ABSTRACT

Title of Document: OPTIMIZATION OF $Pb(Zr_{52}Ti_{48})O_3$ THROUGH IMPROVED PLATINUM METALLIZATION, USE OF A $PbTiO_3$ SEED LAYER, AND FINE TUNING OF ANNEALING CONDITIONS FOR APPLICATIONS IN MULTILAYER ACTUATOR MEMS TECHNOLOGY

Luz Miriam Sanchez, Doctor of Philosophy, 2014

Directed By: Professor Ichiro Takeuchi
Department of Materials Science And Engineering

Dr. Ronald G. Polcawich
U.S. Army Research Laboratory, Adelphi, MD

Using a systematic approach, the processing of PZT (52/48) was optimized to achieve both a high degree of {001} texture and high piezoelectric properties. Initial experiments examined the influence of Ti/Pt and TiO_2/Pt thins films used as the base-electrode for chemical solution deposition PZT thin film growth. The second objective was to achieve highly {001}-textured PZT using a seed layer of $PbTiO_3$ (PTO). A comparative study was performed between Ti/Pt and TiO_2/Pt bottom electrodes. The results indicate that the use of a highly oriented TiO_2 led to highly {111}-textured Pt, which in turn improved both the PTO and PZT orientations. A third objective was to determine the effects of lead excess in the starting PTO and PZT solution on the films orientations and piezoelectric properties. During the

annealing of PZT (52/48), lead (Pb) is volatilized from the films leading to a non stoichiometric state which ultimately reduces the electrical properties. To remedy this issue, a percentage of Pb-excess is added to the PZT solution prior to deposition to compensate for the Pb that is lost during the thermal treatment. This study thoroughly examines the effects of the Pb-excess in the PTO seed layer with percentages between 0% and 30% and PZT (52/48) with Pb-excesses between 0% and 10%. The final objective, leveraged the texture optimization on single 500nm thick PZT thin films, to deposit high quality PZT films in multiple Pt/PZT/Pt layers for use in multilayer actuators (MLA). Efforts have been focused on developing actuators using a four 250 nm layer stack of PZT using 10% lead excess in solution. By performing x-ray diffraction (XRD) measurements between each layer, the texture within the films could be monitored during the growth process. To electrically measure the quality of the PZT multilayer stack, a series of six-sided capacitors were fabricated. In addition to capacitors, cantilever actuators were fabricated so as to measure the piezoelectric induced deformation. These measurements on MLA PZT films demonstrate high piezoelectric coefficients that are suitable for tactile radio and mm-scale robotic devices.

OPTIMIZATION OF $Pb(Zr_{52}Ti_{48})O_3$ THROUGH IMPROVED PLATINUM METALLIZATION, USE OF A $PbTiO_3$ SEED LAYER, AND FINE TUNING OF ANNEALING CONDITIONS FOR APPLICATIONS IN MULTILAYER ACTUATOR MEMS TECHNOLOGY

By

Luz Miriam Sanchez

Dissertation submitted to the Faculty of the Graduate School of the
University of Maryland, College Park, in partial fulfillment
of the requirements for the degree of
Doctor of Philosophy
2014

Advisory Committee:

Professor Ichiro Takeuchi, Chair
Dr. Ronald G. Polcawich
Professor John Cumings
Professor Don DeVoe
Professor Robert M. Briber

Dedication

To my father and mother
Martin and Maria Sanchez

&

In loving memory

Ana Ballesteros
Jacqueline Nicole Sanchez
Father Jose Aldegunde

Acknowledgements

I am very thankful to my advisor, Professor Ichiro Takeuchi, for the amazing opportunity to be a part of his research group at the University of Maryland while working off-campus at the U.S. Army Research Laboratory. I would also like to thank my committee members Professor John Cumings and Professor Don DeVoe for your interest in my research and for providing guidance and support through this process. A special thanks to Professor Robert Briber for his interest in my research and in particular for accepting to be a part of my committee at the last minute.

I would like to acknowledge my colleagues and the technical staff at the U.S. Army Research Laboratory (ARL). In particular Brian Power, Joel Martin, Steven Isaacson and Dr. Daniel Potrepka who have repeatedly answered all of my questions, provided much needed assistance, and who tolerated me when I followed them around the cleanroom. I am also thankful to everyone on the Cleanroom staff who have maintained the equipment and provided the necessary training in particular Jim Mulcahy, Joyce Bell-Sampson, and Nicholas Strnad. I would also like to thank Dr. Robert Proie, Ryan Rudy, Gabriel Smith, and Jeffrey Pulskamp who have answered countless questions and provided valuable assistance ranging from connecting my ground probe correctly to homemade cookies. I would like to thank Dr. Brett Piekarski for his continued support since 2008 and for allowing me to pursue my studies while working at ARL.

I am also very thankful to my co-advisor, Dr. Ronald G. Polcawich at the U.S. Army Laboratory. Outside of his extreme patience, guidance, and support throughout

my graduate studies, his drive has been inspiring to me. He has also forced me to "think outside the box" when I didn't want to and for that I am grateful.

I could not have completed my graduate studies and work without the support of my family and friends. My old friends, in particular Cassandra Oliver-Croswell and Ali Dalipi who entertained me all throughout undergrad and made my move from New York to Maryland a lot less lonesome. My new friends in Maryland, far too many to list, who have supported me throughout this process, in particular Paris Alexander and Richard Suchoski who have spent many late nights with me at the University of Maryland, the times I managed to leave ARL in order to get more ARL work done. Retired Sergeant Major Steven Hornbach who even though he's retired from the military, it doesn't stop him from keeping me on task while taking the occasional dinner break. Simon Ghionea, who has spent the last two years reminding me that the light at the end of the tunnel was nearing, I am thankful for all of your truly unconditional support.

I would like to thank my brother, retired Chief Juan Carlos Sanchez, and his family, Dina and Selena Sanchez, who have provided extremely pleasant and needed breaks every time we visited each other. I am thankful to Walter and Glady's Galvan who have basically known me since I was the size of a pinto bean and have shown me that you do not need to be a blood relative to call someone your family. As odd as it may seem, I am also thankful to my Chihuahua Whiskey who has been with me since the start of my graduate studies, keeping my lap warm, my cheeks wet with kisses, and provided much comic relief in his silly costumes which he loves to prance around in. Lastly, I am extremely thankful to my parents Martin and Maria Sanchez for their

endless patience, support, encouragement, and advice. I could have never pursued my ambitions without you.

Estoy agradecido a Walter y Gladys Galván que básicamente me han conocido desde que era del tamaño de un frijol pinto y me han demostrado que no es necesario ser un pariente de sangre para llamar a alguien de tu familia. Por lo extraño que pueda parecer, también estoy agradecida a mi Chihuahua whiskey que ha estado conmigo desde el comienzo de mis estudios en Maryland, manteniendo mis piernas calientes, mis cachetes llenos de besos, y proporcionó un gran alivio cómico en sus trajes tontos que les encanta. Finalmente, estoy muy agradecido a mis padres Martín y María Sánchez por su infinita paciencia, su apoyo, aliento y sus buenos consejos. Yo nunca podría haber seguido mis ambiciones sin ustedes. Los quiero mucho.

Table of Contents

List of Tables

List of Figures

Chapter 1: Introduction into the World of Piezoelectric Micromechanical Systems (MEMS)

1.1 Everyday MEMS

It is virtually impossible to imagine carrying around a large bulky computer, gaming console, or even cell phone since the advent of microelectromechanical systems (MEMS). The miniaturization of the electrical components in those devices and many others has led to a generation of young adults who have rarely seen cell phones larger than the average hand of a person, or have ever used a cassette player or even a portable compact disk player. Thanks to the new products made possible due to MEMS it is possible to have access to almost anything in the world right in the palm of your hand.

The technology available through MEMS isn't limited to entertainment systems, but is also widely used in automotive and aerospace as accelerometers[1] and magnetic-field sensors [2], in medical as non-integrated pressure sensors and micro catheters [3] , communications for switching and tuning [4], just to name a few.

Up until 2011 the MEMS market was expected to reach approximately $10 million dollars according to the Yole Developpment market analysis [5]. The top 4 MEMS companies are Texas Instruments, STMicroelectronics, Hewlett Packard, and Robert Bosch leading the competition with an estimate of over $700 Million in

revenue through March 2012 [5]. It has become more than apparent that all future technologies will have MEMS components incorporated into it in one way or another.

1.2 Actuated Systems

A very brief overview of how MEMS devices are already present in our everyday lives has been discussed. One specific type of MEMS devices that will be the focus of this thesis are actuated systems. Actuators provide some sort of motion in a system. MEMS actuators typically do more than just move components, they must also operate within a targeted voltage range, provide high forces, provide variable speed, and ideally be able to provide sensory feedback for control..

1.2.1 Driving Materials in Actuators

In selecting a MEMS actuator, the material driving the motion is very important. Depending on the final device and application MEMS actuators can be electrostatic, thermal, magnetic, or piezoelectrically driven. In electrostatic actuators, there is an attraction between oppositely charged conductors through the application of a voltage. Thermally driven actuators create displacements through thermal expansion. Magnetic actuators require a magnetic or electromagnetic field to create a displacement. Piezoelectric actuators are displaced due to strains induced by an electric field. The piezoelectric actuators typically exhibit large displacements in low fields leading the focus of this thesis to be placed on piezoelectric actuation.

1.3 Discovery to Development: 1860-1960's

The existence of piezoelectric properties has been known for over 300 years and it its earliest days were known simply as mysterious properties. In India and Ceylon, Tourmaline, a semi-precious gemstone, exhibited a strange effect when put into hot ash; it would attract the ash on one end of the crystal and repeal it on the other end, over time the attraction and rejection sides of the crystal would be inverted [6]. In the early 1700's Tourmaline physical properties were described in a book by Johann Georg-Schmidt where shortly afterwards Louis Lemery would write the first scientific description of pyroelectricity and in 1747 Carl Linnaeus would coin the term "Lapis Electricus" which stands for electric stone in Latin [7]. By the early 1800's, René Just Haüy and Antoine César Becquerel found a relationship between pressure and electricity but the discovery of piezoelectrity wouldn't really occur until the Curie brothers, Pierre and Jacques, in 1880 [8].

The Curie brothers demonstrated that an electrical polarization was created in tourmaline, quarts, topaz, cane sugar, and Rochelle salt when a mechanical stress was applied [9]. There are two parts to piezoelectricity, the direct piezoelectric effect and the converse piezoelectric effect; the Curie brothers discovered the direct piezoelectric effect. A year later in 1881, Gabriel Lippman predicted the converse piezoelectric effect based off the Carnot principle [10], essentially stating that by applying electricity to the crystal there will be a change in its volume. The Curie brothers experimentally proved the converse piezoelectric effect shortly afterwards.

Prior to World War I in 1914, work performed on piezoelectricity was mostly on the development of thermodynamic models and the asymmetric nature of

piezoelectric crystals. With the eruption of World War I, Paul Langevin and Constatin Chilowski worked on the first serious application of a piezoelectric crystal, quartz, for ultrasonic submarine detection which was patented in 1917 using active detection techniques, emitting signals to detect the presence of submarines. Their successful work leveraged work performed by Ernest Rutherford and Robert William Boyle in 1916. Unfortunately for Rutherford and Boyle, their research consisted of using passive detection, detecting the sound emitted by submarines, which didn't work nearly as effectively as Langevin's method. Their work on generating high-frequency waves using piezoelectric crystals [11] was essentially what led to Langevin's active detection method using quartz. Langevin's ultrasonic submarine detection system wouldn't be fully operational until the end of the war.

Between World War I and II, there would be burst of novel technologies using piezoelectric materials such as frequency stabilizers for vacuum tube oscillators, ultrasonic transducers for the measurement of material properties, and commercial products such as microphones and accelerometers [12]. With the start of World War II in 1938, significant research was performed by the United States, Japan, and the Soviet Union on the development of materials with high dielectric constants. This paved the way to tailor existing materials to specific applications and also resulted in a number of inventions; sonar, piezoelectric ignition systems [13], and sensitive hydrophones [14][15] and a large number of patents for different types of piezoelectric devices were filed between 1938 and 1960, [16]–[20].

1.4 Chapter Descriptions and Thesis Objectives

A more detailed description of the piezoelectric effects and measurement techniques are described in Chapter 2. The synthesis and chemical solution deposition techniques are detailed in Chapter 3. This chapter also describes the fabrication of the MEMS capacitors and cantilever arrays used in this study as well as the measurement techniques used. The results of optimizations performed on the piezoelectric material, lead zirconate titanate such as variations in thermal conditions, stoichiometry of starting solutions, and changes to the bottom platinum electrode as described in Chapter 4. The main focus of this chapter is the effects a thin layer of $PbTiO_3$ has on the orientation and electrical properties of the PZT (52/48) films. Chapter 5 highlights the use of the optimizations, described previously in Chapter 4, in particular a more thorough investigation of the effects of lead excess in starting solutions on the resultant film. Several samples were fabricated and electrical measurements were performed to determine the effects. Using the optimization techniques developed, a 4-layer multilayer device is fabricated and described in Chapter 6. This multilayer device using the optimized PZT (52/48) process will reduce the driving voltage of the MEMS device while maintaining the same actuator displacement characteristics as a single stack PZT device. The fabrication and results from electrical testing are described in Chapter 6. Chapter 7 summarizes the results of all the previous experimental chapters and describes future work that is needed to further understand the material properties.

Chapter 2: The Piezoelectric Effect and Theories

2.1 What is the Piezoelectric Effect

The Curie brothers' first discovery of piezoelectricity was the direct piezoelectric effect; a buildup of charges is produced along the surface of the material due to a mechanical strain, Figure 1. The direct piezoelectric effect is the basis upon which sensors operate. As a mechanical pressure, i.e. sound wave, is applied to a piezoelectric film, deformations in the lattice create dipoles within the film. The resulting electric field produced in the film creates a potential on electrodes of the piezoelectric sensor.

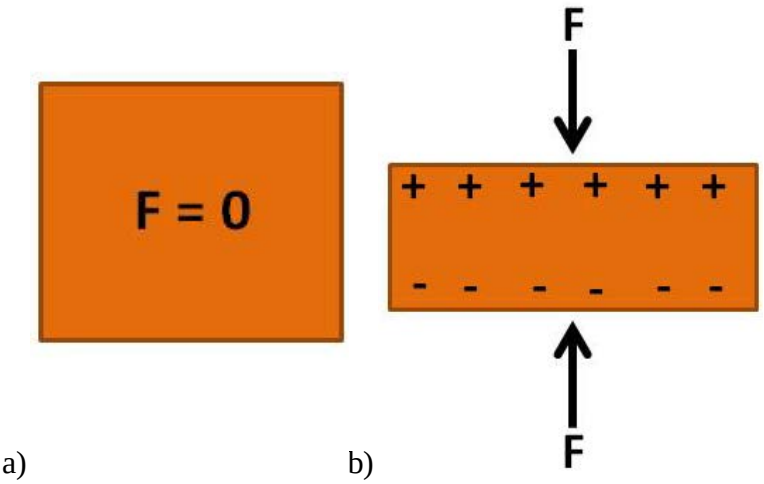

Figure 1. The direct piezoelectric effect under the application of different forces. The application of a) zero force results in no surface charges once the film experiences a b) force charges build up on opposite surfaces.

The converse piezoelectric effect is used in actuators as the application of a voltage on a piezoelectric film will result in a change in volume of the material, Figure 2. When an alternating voltage is applied to the device, it will contract and expand at the frequency of the applied voltage [10]. When used in this mode and paired with a stiffer and thick substrate, such as silicon, actuator beams can be created for applications in switches. The actuator beam tip displacement can be modified by designing the position of the piezoelectric layer relative to the neutral axis position of the beam, further described in the *section* 2.3.3.

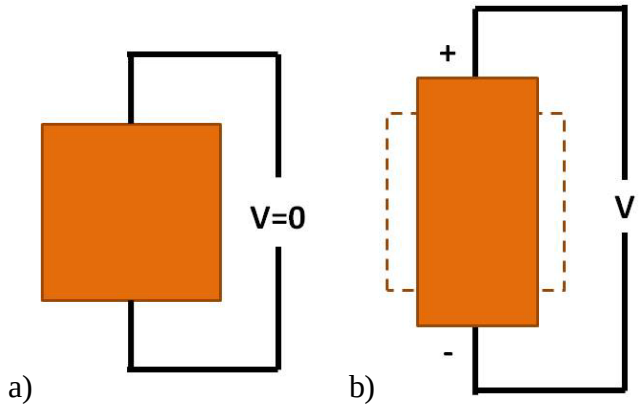

Figure 2. The converse piezoelectric effect where with a) no applied voltage there is no change of shape but with b) the application of a voltage there is a change of shape in the material.

2.2 Crystal Structures: The Perovskite Structure

The absence of a center of symmetry in the crystal structure is a requirement in the piezoelectric effect. A piezoelectric ceramic involves a large group of perovskite unit cells (ABO_3), where each individual crystal is composed of a lattice of oxygen at the face center of the cell, large divalent metal ions at the corners, and a small tetravalent metal ion located inside of this lattice (Figure 3a). Due to the shift of the center tetravalent metal ion and stringent requirements of the cubic unit cell structure, tilting is observed in the oxygen octahedral [21] [22] leading to the development of an electrical dipole (Figure 3b).

2.2.1 Curie Temperature

Temperature plays a crucial role in the perovskite structure as it leads to substantial changes in not only the structure itself but also in the unique properties observed in piezoelectric crystals. At a material dependent critical temperature there is a sudden change in the direction of the electrical dipole. This critical temperature is known as the Curie temperature, T_c. At T_c and higher temperatures, the perovskite crystal resembles a simple cubic structure (Figure 3a) with no dipole moment. Once the temperature is lowered below T_c, each perovskite cell deviates from the simple cubic structure as the ions shift to a lower energy configuration ultimately resulting in the creation of an electric dipole within the unit cell. In Figure 3b a shift in the center metal ion, which is positively charged, in the Z-direction towards the divalent metal ions at the four top corners of the cell, lead to an elongation of the cell as the divalent metal ions are also positively charged and a net positive charge in the top half the

cell is created. The five oxygen atoms at the bottom half of the cell create a net negative charge in the bottom half of the unit cell.

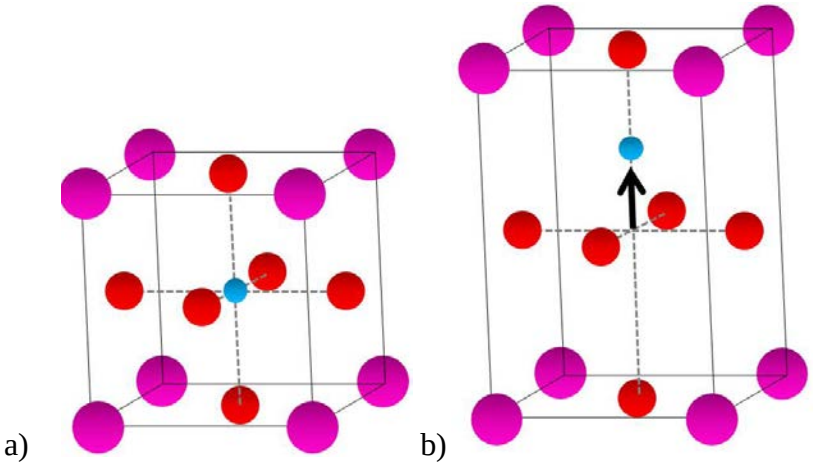

Figure 3. The perovskite crystal structure a) cubic structure observed at temperatures higher than the Curie temperature and b) center ion off center causing a dipole at temperatures below the Curie temperature.

2.3 Ferroelectricity

The dipole moment of a perovskite unit cell is observed throughout the entire film leading to a net polarization of the film. Polarization is a vector component as it has both magnitude and direction associated to it. In the case where there are oppositely alternating polarization vectors, the film is said to be antiferroelectric as the adjacent polarization vectors cancel each other resulting in a film with a net polarization of zero(Figure 4a). When the polarization vectors are generally aligned in the same direction, the material is ferroelectric (Figure 4b).

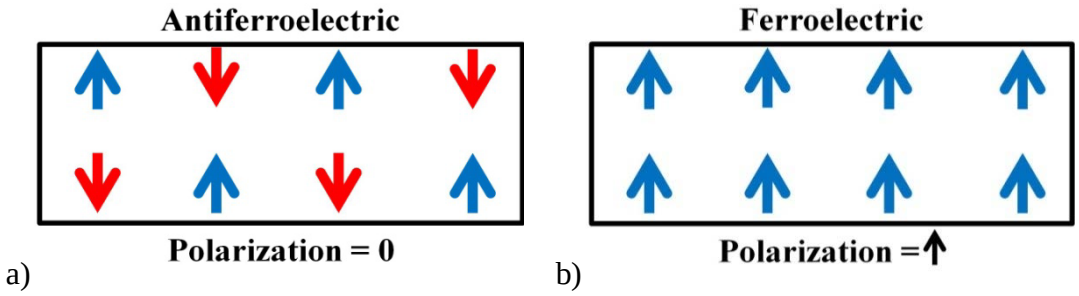

Figure 4. Two examples of domain configurations a) antiferroelectric and b) ferroelectric

2.2.1 Polarization in Ferroelectric Materials

A ferroelectric material exhibits a polarization at zero volts. As a voltage is applied, internal dipoles are rotated into the direction of the electric field. In ferroelectric materials the polarization axis is determined by the crystalline structure of the material. This electric field, stress, and concentration gradients cause abrupt changes between the two oppositely polarized domains. This is a non-linear process and depends on the electric field experienced by the material and its history, giving rise to a hysteresis Figure 5a.

Upon the application of a voltage, changes in the films dipole moments can be observed. With increasing voltage, an internal electrical field is produced as the dipoles align with the field, ultimately reaching a maximum polarization value, P_{max}. In an ideal material, all the dipoles would align with the field. However, in real ferroelectric materials dipole pinning occurs due to material defects and intergranular stresses. These defects create deformities in the crystal lattice and local electric fields which can permanently pin the ferroelectric materials dipoles or affect its switching behavior [23]. As the voltage is decreased from P_{max}, the dipoles begin to switch direction. Due to the non-ideal nature of the domain interactions, the reverse

polarization path is different from the forward polarization path. Once it returns to zero volts, the material maintains some of its dipole configuration, depending on the direction of the field, leading to a remanent polarization, P_r. The coercive voltage, E_c, is also an important value as it determines the field required to achieve zero polarization and also the start of domain switching in the ferroelectric material Figure 5b.

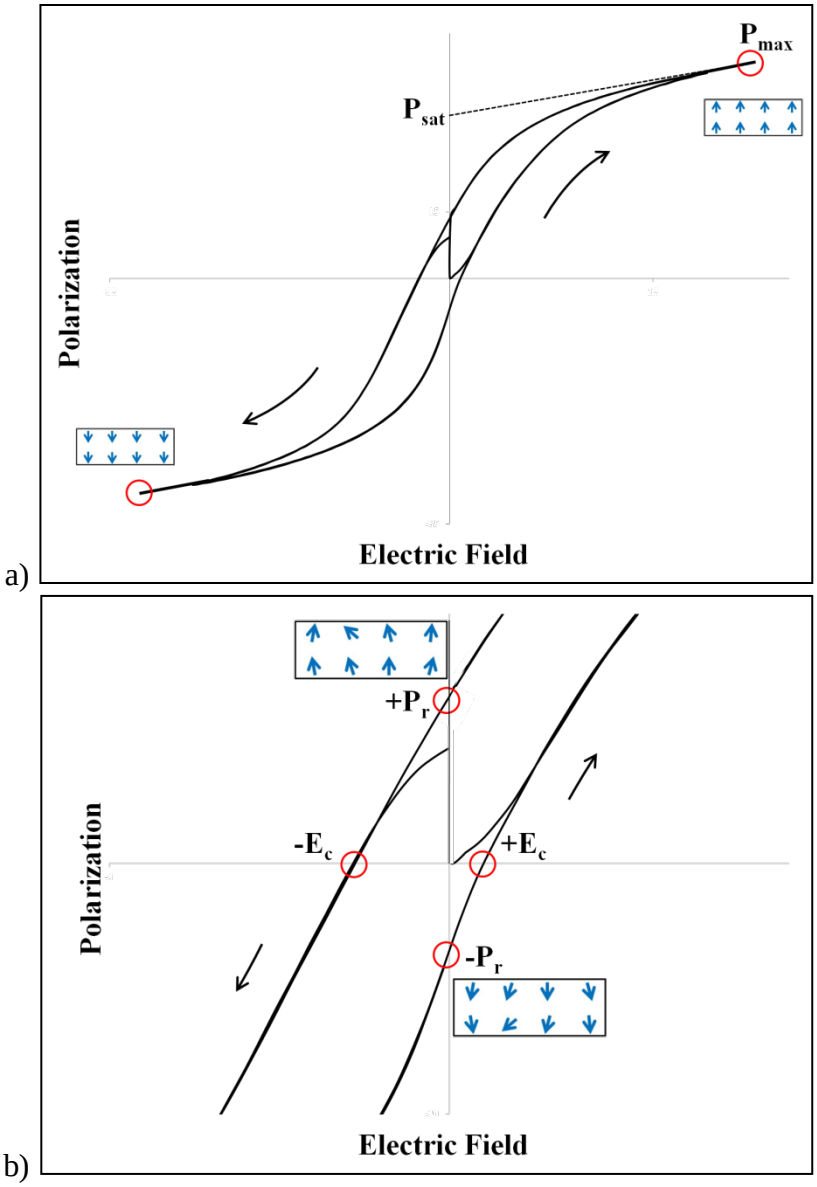

Figure 5.Polarization –electric field (PE) hysteresis loop observed from a ferroelectric film. a) the full loop and b) a magnified section of the loop showing the remanent polarization and coercive voltages.

2.2.2 Hysteresis Shape and Material Properties

Gathering information of the maximum polarization and remanent polarization are important, however the hysteresis loop shape and shift characteristics are also important. Square shaped hysteresis show greater switching capabilities in films but also represent a film with few defects that pin domains or preferential defect orientation. A hysteresis with a tilted loop demonstrates the presence of a dielectric film with a low permittivity located between the PZT film and the electrode [24][25][26]. This dielectric film is most likely a Pb deficient layer formed during the 700°C annealing process of the film as PbO volatilizes at temperatures above 500°C. The tilt in the hysteresis loop is increased if the dielectric film thickness is increased. This is proven by calculating slope of the hysteresis at the coercive field and the effect of the depolarizing field effects on the slope [24]. The depolarizing field, $E_{d,}$ is a function of the total macroscopic electric field, E_{tot}, and the applied electric field, E_o.

$$\boldsymbol{E_{tot} = E_o + E_d}$$

The depolarizing field develops to counter the effect of the applied electric field. Although the depolarizing field in the film is minimized during cooling from the Curie temperature, it may develop when there is an uneven distribution of the spontaneous polarization, particularly near the surface of the film [26]. In this scenario the depolarization field is a function of polarization, P, and thickness of the PZT film, t, and the thickness of the dielectric layer, d, and its dielectric constant, ε_d.

$$E_d = -\left(\frac{P}{t}\right)\left(\frac{d}{\varepsilon_d}\right)$$

The hysteresis tilt can be best described as the slope of the hysteresis at the coercive field. To determine the slope the derivative of the total macroscopic electric field is taken. As the ratio between d/t increases, the tilt of the hysteresis loop increases [24][26]. After a certain dielectric layer thickness the hysteresis will resemble a football shaped loop which is observed when measuring films with high leakage current.

$$\left(\frac{\partial E_{tot}}{\partial P}\right)_{E_c} - \left(\frac{\partial E_o}{\partial P}\right)_{E_c} = -\frac{1}{\varepsilon_d}\left(\frac{d}{t}\right)$$

Tilted hysteresis loop are not the only type of shape that may be present in the hysteresis measurements, shifted or imprinted and pinched loops are also observed. Both phenomena may occur due to electronic defect dipoles, Pb or O vacancies or through substitution of ions (doping) with different valences, in the PZT [27]. A hysteresis loop that is either positively or negatively shifted along the field axis develops if there is an internal field in the PZT film that may be present due to the preferential orientation of electric defect dipoles [28][29]. While pinched loops can also result from both positive and negative internal fields due to preferential orientation, another mechanism is the diffusion of the defects into domain walls thus pinning the domain walls until a large enough external field is applied. The pinched effect in hysteresis loops can be temporarily [30] reduced or eliminated by annealing the sample past the Curie temperature or switching the device several times to relax the film.

2.4 Piezoelectric Material Calculations

2.3.1 Determination of the Piezoelectric Constants

Piezoelectric materials exhibit a coupling between the electric behavior involving the dielectric displacement (D) and the electric field applied (E) and Hooks law involving the strain (ε) and the stress (σ), determined by

$$\boldsymbol{D = \xi E} \quad \boldsymbol{\varepsilon = S\sigma}$$

D = vector of dielectric displacement (C/m^2)
ξ = permittivity of the material (F/m)
E = applied electric field (V/m)
ε = strain vector (m/m)
S = compliance coefficient (m^2/C)
σ = stress vector (N/m^2)

The stress and strain tensors can also be described in terms of the sum of their piezoelectric coefficients and the applied electric field:

$$\boldsymbol{\varepsilon_i = \sum_j d_{ji} E_j} \qquad \boldsymbol{\sigma_i = \sum_j e_{ji} E_j}$$

ε = strain vector (m/m)
d = piezoelectric strain coefficient
e = piezoelectric stress coefficient
E = applied electric field (V/m)

The electromechanical equations expressing the relationship between the electrical behavior and hooks law for linear piezoelectric materials can be expressed as:

$$\boldsymbol{\varepsilon_i = S_{ij}^{E}\sigma_j + d_{mi}E_m}$$

$$\boldsymbol{D_m = d_{mi}\sigma_j + \epsilon_{mk}{}^{\sigma}E_k}$$

D = vector of dielectric displacement (C/m^2)
ϵ = permittivity of the material (F/m)
E = applied electric field (V/m)
ε = strain vector (m/m)
S = compliance coefficient (m^2/C)
σ = stress vector (N/m^2)
d = piezoelectric strain constant (3^{rd} rank tensor)

The subscripts in the electromechanical equations define the direction within the materials coordinate system. The indexes *i*, *j* = 1, 2, 3,…,6 and *m*,*k* = 1, 2, 3 (Figure 6). The superscripts E and σ are held at either a constant electric field or at a constant stress in the material. The piezoelectric strain constant, d_{ij}, corresponds to the strain or force that is developed in the *j* direction in response to an applied field in the *i* direction.

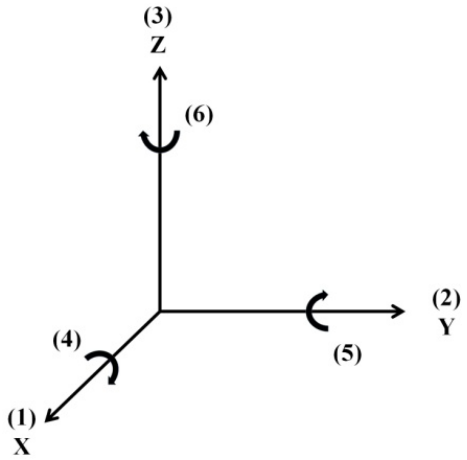

Figure 6. Axis nomenclature.

The electromechanical equations that express the relationship between the electrical behavior and hooks law for linear piezoelectric materials can be expanded as the following matrices:

$$\begin{bmatrix}\varepsilon_1\\ \varepsilon_2\\ \varepsilon_3\\ \varepsilon_4\\ \varepsilon_5\\ \varepsilon_6\end{bmatrix} = \begin{bmatrix}S_{11} & S_{12} & S_{13} & S_{14} & S_{15} & S_{16}\\ S_{21} & S_{22} & S_{23} & S_{24} & S_{25} & S_{26}\\ S_{31} & S_{32} & S_{33} & S_{34} & S_{35} & S_{36}\\ S_{41} & S_{42} & S_{43} & S_{44} & S_{45} & S_{46}\\ S_{51} & S_{52} & S_{53} & S_{54} & S_{55} & S_{56}\\ S_{61} & S_{62} & S_{63} & S_{64} & S_{65} & S_{66}\end{bmatrix}\begin{bmatrix}\sigma_1\\ \sigma_2\\ \sigma_3\\ \sigma_4\\ \sigma_5\\ \sigma_6\end{bmatrix} + \begin{bmatrix}d_{11} & d_{21} & d_{31}\\ d_{12} & d_{22} & d_{32}\\ d_{13} & d_{23} & d_{33}\\ d_{14} & d_{24} & d_{34}\\ d_{15} & d_{25} & d_{35}\\ d_{16} & d_{26} & d_{36}\end{bmatrix}\begin{bmatrix}E_1\\ E_2\\ E_3\end{bmatrix}$$

$$\begin{bmatrix}D_1\\ D_2\\ D_3\end{bmatrix} = \begin{bmatrix}d_{11} & d_{12} & d_{13} & d_{14} & d_{15} & d_{16}\\ d_{21} & d_{22} & d_{23} & d_{24} & d_{25} & d_{26}\\ d_{31} & d_{32} & d_{33} & d_{34} & d_{35} & d_{36}\end{bmatrix}\begin{bmatrix}\sigma_1\\ \sigma_2\\ \sigma_3\\ \sigma_4\\ \sigma_5\\ \sigma_6\end{bmatrix} + \begin{bmatrix}\epsilon_{11} & \epsilon_{21} & \epsilon_{31}\\ \epsilon_{12} & \epsilon_{22} & \epsilon_{32}\\ \epsilon_{13} & \epsilon_{23} & \epsilon_{33}\end{bmatrix}\begin{bmatrix}E_1\\ E_2\\ E_3\end{bmatrix}$$

In anisotropic materials the stress and strain relationship may require 21 independent constants while limiting to isotropic materials [31], which piezoelectric materials can be assumed to be transversely isotropic, the number of independent constants are reduced using the relationships.

$$S_{11} = S_{22}$$
$$S_{13} = S_{31} = S_{23} = S_{32}$$
$$S_{12} = S_{21}$$
$$S_{44} = S_{55}$$
$$S_{66} = 2\,(S_{11} - S_{12})$$

$$d_{31} = d_{32}$$
$$d_{15} = d_{24}$$

$$\epsilon_{11} = \epsilon_{22}$$
$$\epsilon_{33}$$

The non-zero coefficients and the new coupled electromechanical matrices are shown below.

$$\begin{bmatrix}\boldsymbol{\varepsilon_1}\\ \boldsymbol{\varepsilon_2}\\ \boldsymbol{\varepsilon_3}\\ \boldsymbol{\varepsilon_4}\\ \boldsymbol{\varepsilon_5}\\ \boldsymbol{\varepsilon_6}\end{bmatrix} = \begin{bmatrix}\boldsymbol{S_{11}} & \boldsymbol{S_{12}} & \boldsymbol{S_{13}} & \boldsymbol{0} & \boldsymbol{0} & \boldsymbol{0}\\ \boldsymbol{S_{21}} & \boldsymbol{S_{22}} & \boldsymbol{S_{23}} & \boldsymbol{0} & \boldsymbol{0} & \boldsymbol{0}\\ \boldsymbol{S_{31}} & \boldsymbol{S_{32}} & \boldsymbol{S_{33}} & \boldsymbol{0} & \boldsymbol{0} & \boldsymbol{0}\\ \boldsymbol{0} & \boldsymbol{0} & \boldsymbol{0} & \boldsymbol{S_{44}} & \boldsymbol{0} & \boldsymbol{0}\\ \boldsymbol{0} & \boldsymbol{0} & \boldsymbol{0} & \boldsymbol{0} & \boldsymbol{S_{55}} & \boldsymbol{0}\\ \boldsymbol{0} & \boldsymbol{0} & \boldsymbol{0} & \boldsymbol{0} & \boldsymbol{0} & \boldsymbol{S_{66}}\end{bmatrix}\begin{bmatrix}\boldsymbol{\sigma_1}\\ \boldsymbol{\sigma_2}\\ \boldsymbol{\sigma_3}\\ \boldsymbol{\sigma_4}\\ \boldsymbol{\sigma_5}\\ \boldsymbol{\sigma_6}\end{bmatrix} + \begin{bmatrix}\boldsymbol{0} & \boldsymbol{0} & \boldsymbol{d_{31}}\\ \boldsymbol{0} & \boldsymbol{0} & \boldsymbol{d_{32}}\\ \boldsymbol{0} & \boldsymbol{0} & \boldsymbol{d_{33}}\\ \boldsymbol{0} & \boldsymbol{d_{24}} & \boldsymbol{0}\\ \boldsymbol{d_{15}} & \boldsymbol{0} & \boldsymbol{0}\\ \boldsymbol{0} & \boldsymbol{0} & \boldsymbol{0}\end{bmatrix}\begin{bmatrix}\boldsymbol{E_1}\\ \boldsymbol{E_2}\\ \boldsymbol{E_3}\end{bmatrix}$$

$$\begin{bmatrix}\boldsymbol{D_1}\\ \boldsymbol{D_2}\\ \boldsymbol{D_3}\end{bmatrix} = \begin{bmatrix}\boldsymbol{0} & \boldsymbol{0} & \boldsymbol{0} & \boldsymbol{0} & \boldsymbol{d_{15}} & \boldsymbol{0}\\ \boldsymbol{0} & \boldsymbol{0} & \boldsymbol{0} & \boldsymbol{d_{24}} & \boldsymbol{0} & \boldsymbol{0}\\ \boldsymbol{d_{31}} & \boldsymbol{d_{32}} & \boldsymbol{d_{33}} & \boldsymbol{0} & \boldsymbol{0} & \boldsymbol{0}\end{bmatrix}\begin{bmatrix}\boldsymbol{\sigma_1}\\ \boldsymbol{\sigma_2}\\ \boldsymbol{\sigma_3}\\ \boldsymbol{\sigma_4}\\ \boldsymbol{\sigma_5}\\ \boldsymbol{\sigma_6}\end{bmatrix} + \begin{bmatrix}\boldsymbol{\epsilon_{11}} & \boldsymbol{0} & \boldsymbol{0}\\ \boldsymbol{0} & \boldsymbol{\epsilon_{22}} & \boldsymbol{0}\\ \boldsymbol{0} & \boldsymbol{0} & \boldsymbol{\epsilon_{33}}\end{bmatrix}\begin{bmatrix}\boldsymbol{E_1}\\ \boldsymbol{E_2}\\ \boldsymbol{E_3}\end{bmatrix}$$

While the piezoelectric strain coefficient, d_{ij}, was used in the coupled electromechanical equations for piezoelectric materials above, there are several other piezoelectric coefficients of interest in this field; namely the piezoelectric stress coefficient e_{ij} which is the piezoelectric charge as a function of the stresses. Both the piezoelectric strain and stress coefficients are useful in thin film actuators and sensors and can be related to one another through the stiffness tensor, c_{pk}. There are several other piezoelectric coefficients such as g_{ij} and h_{ij} which relates the electric field to stress and the strain to electric field, respectively.

2.3.2 Determination of $e_{31,f}$ in an Actuator

In thin film piezoelectric actuators the film is only a small section of a composite structure, typically using a thick elastic layer clamping the film along the substrate-piezoelectric interface but allowing it to move freely out of plane (Figure 7).

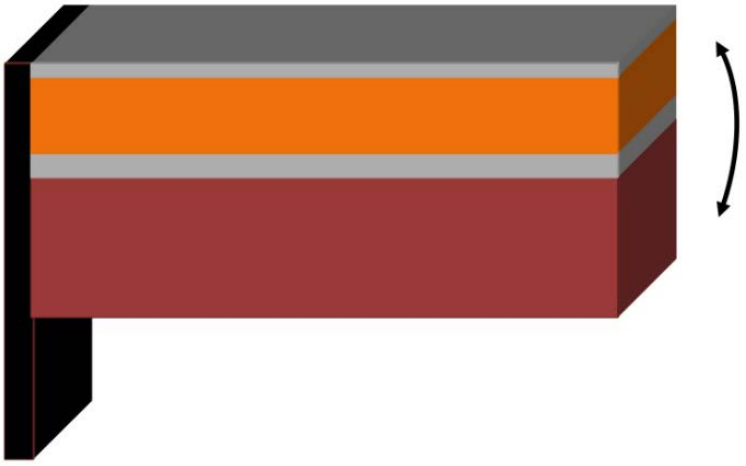

Figure 7. Thin film unimorph cantilever beam

The piezoelectric stress and strain coefficients are typically calculated where the z-axis is aligned with the poling direction of the material. The values for e_{31} and d_{33} are usually reported where e_{31} will described the piezoelectric charge of a beam and d_{33} described the longitudinal response [32]. In actuators the converse piezoelectric effect is used leading to in-plane strains that are equal to zero,$\varepsilon_1 = \varepsilon_2 = 0$, while out of plane strain and in-plane stresses are created:

$$\boldsymbol{\varepsilon_1 = (S_{11} + S_{12})\sigma_1 + d_{31}E_3 = 0}$$

$$\boldsymbol{\varepsilon_3 = 2(S_{13}\sigma_1) + d_{33}E_3}$$

Directly measurable e_{31} and d_{33} values can be obtained and are described as the effective $e_{31,f}$ and $d_{33,f}$. The measured $d_{33,f}$ is less than the calculated d_{33} and $e_{31,f}$ is always larger than the e_{31}. The impact of high $e_{31,f}$ in piezoelectric films means that higher displacements can be achieved in actuators.

$$\boldsymbol{\varepsilon_1 = (S_{11} + S_{12})(-e_{31,f}E_3) + d_{31}E_3 = 0}$$

$$\boldsymbol{\varepsilon_1 = E_3[-e_{31,f}(S_{11} + S_{12}) + d_{31}] = 0}$$

$$\boldsymbol{-e_{31,f}(S_{11} + S_{12}) = d_{31}}$$

$$\boldsymbol{-e_{31,f} = \frac{d_{31}}{(S_{11} + S_{12})}}$$

$$\boldsymbol{\varepsilon_3 = 2[S_{13}(-e_{31}E_3)] + d_{33}E_3}$$

$$\boldsymbol{d_{33,f}E_3 = E_3[2(-e_{31}S_{13}) + d_{33}]}$$

$$\boldsymbol{d_{33,f} = d_{33} - \frac{2S_{13}}{S_{11} + S_{12}}d_{31}}$$

A method used to determine the $e_{31,f}$ of piezoelectric actuators is by measuring the tip displacement in a beam by the application of voltage. The substrate upon which the piezoelectric material is on will greatly affect this measurement since the thickness of the substrate is considered to be much greater than the thickness of the piezoelectric material. Since the film is free to move in 3 (Z-direction) and the stresses σ_1 and σ_2 are equal due to the isotropic nature of piezoelectric materials, d_{31} can be derived by:

$$\boldsymbol{\varepsilon_1 = S_{11}\sigma_1 + S_{12}\sigma_1 + d_{31}E_3}$$

The determination of $e_{31,f}$ is fairly straightforward once the cantilever beam is modeled as pure bending of a plate instead of a beam [33]. The electric field, $\boldsymbol{E_3 = {V}/{h_p}}$, where V is the voltage applied and h_p is the piezoelectric material thickness. To calculate the displacement of a plate at the cantilever tip the bending moment must be taken into account; assuming $M_x = M_y$ then:

$$\boldsymbol{M = -h_p \sigma_1 \frac{h_s}{2}}$$

$$\boldsymbol{w(x,y) = -\frac{6M(1-v)}{Yh^3}x^2 - \frac{6M(1-v)}{Yh^3}y^2}$$

$$\boldsymbol{w(L,0) = \delta = -\frac{6M(1-v_s)}{Y_s h_s^3}L^2}$$

$$\boldsymbol{\delta = \frac{3h_p \sigma_1 (1-v_s)}{Y_s h_s^2}L^2}$$

The curvature radius of the beam is $\sin\theta = {\delta}/{L}$ and through small angle approximation $\theta = {\delta}/{L}$. During deflection of the beam the piezoelectric material contracts as a function of the strain, ε_1, while the substrate remains virtually unchanged in length leading to the final equation necessary for the experimental determination of $e_{31,f}$, described in ref [33]:

$$\frac{\boldsymbol{\delta}}{\boldsymbol{L}} = \frac{\boldsymbol{L\varepsilon_1}}{\boldsymbol{h_s}}$$

$$\boldsymbol{\varepsilon_1} = \boldsymbol{h_s}\frac{\boldsymbol{\delta}}{\boldsymbol{L^2}}$$

$$\boldsymbol{d_{31}} = -\frac{\boldsymbol{h_s^2 Y_s(S_{11}+S_{12})}}{\boldsymbol{3(1-v_s)L^2V}}\boldsymbol{\delta} - \frac{\boldsymbol{h_p Y_p(S_{11}+S_{12})}}{\boldsymbol{3(1-v_p)L^2V}}\boldsymbol{\delta}$$

where $h_s >> h_p$,

$$\boldsymbol{d_{31}} = -\frac{\boldsymbol{h_s^2 Y_s(S_{11}+S_{12})}}{\boldsymbol{3(1-v_s)L^2V}}\boldsymbol{\delta}$$

$$-\boldsymbol{e_{31,f}} = \frac{\boldsymbol{d_{31}}}{\boldsymbol{(S_{11}+S_{12})}}$$

$$-\boldsymbol{e_{31,f}} = \frac{\boldsymbol{h_s^2 Y_s(S_{11}+S_{12})}}{\boldsymbol{3(1-v_s)L^2V(S_{11}+S_{12})}}\boldsymbol{\delta}$$

$$-\boldsymbol{e_{31,f}} = \frac{\boldsymbol{h_s^2 Y_s}}{\boldsymbol{3(1-v_s)L^2V}}\boldsymbol{\delta}$$

2.3.3 Determination of the Neutral Axis in a Beam

Another useful value to calculate in piezoelectric beams is the neutral axis. The neutral axis is the axis along a beam in which there are no longitudinal stresses or strains; $\varepsilon_{12} = \varepsilon_{31} = \sigma_{12} = \sigma_{13} = 0$. This is an important value to determine since shows which regions of the beam contribute to resting beam deflection and whether it will be in-plane or out-of-plane. Knowing the neutral axis of a stacked system beforehand assists in the determination of layer thicknesses to achieve the desired MEMS device specifications. Focusing in on the individual components of the beam shown in Figure 7, Figure 8 illustrates a specific composite stack with a SiO_2 elastic layer at the bottom, followed by a bottom electrode such as platinum, a piezoelectric material such as PZT, and a top electrode which may be the same as the bottom electrode for simplicity.

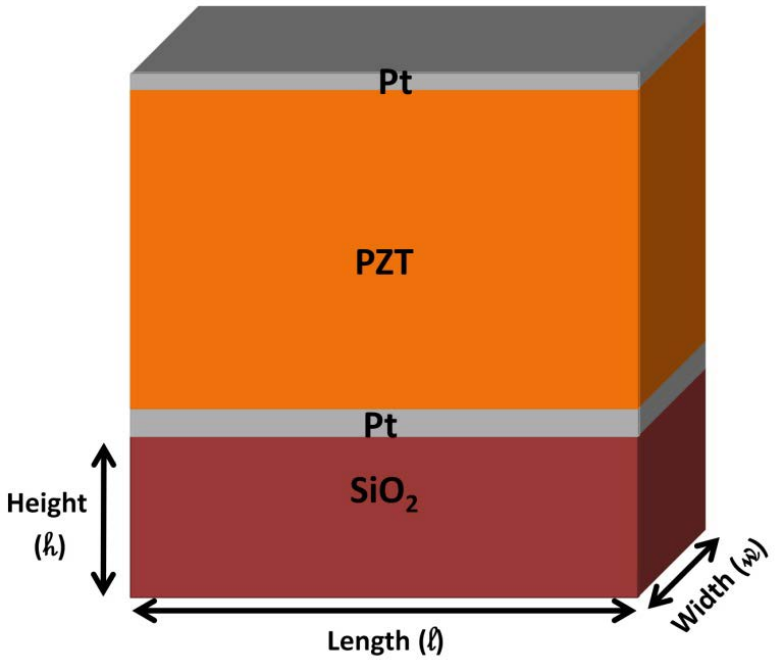

Figure 8. A basic piezoelectric stack using SiO_2 as the thick elastic layer, platinum as both the bottom and top electrode, and PZT as the piezoelectric material.

There are a few parameters that are required for the calculation of the neutral axis such as the thickness or height (h) of the individual films, the length of the beam (l), width of the beam (w), and the Young's Modulus of the material (written as E to prevent confusion). When calculating the neutral axis of different materials such as the stack in Figure 8 it is necessary to transform the stack from uniform length (l) into a length that equals the Young's modulus of the material. A visual representation is shown in Figure 9. Assuming the beam is a simple rectangle, the position of the central axis line for each layer is used and its height relative (y_i) to the bottom of the entire stack (y=0) is used in calculating the neutral axis, Y_{cent} (Figure 10).

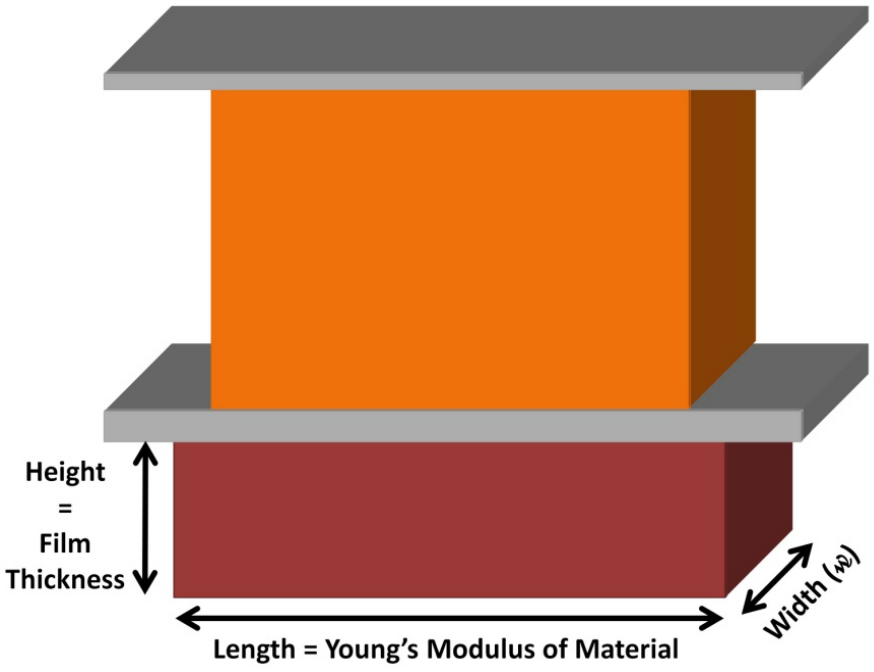

Figure 9. Composite piezoelectric stack from Figure 8 modified based on the normalization of the stack with then Young's Modulus values.

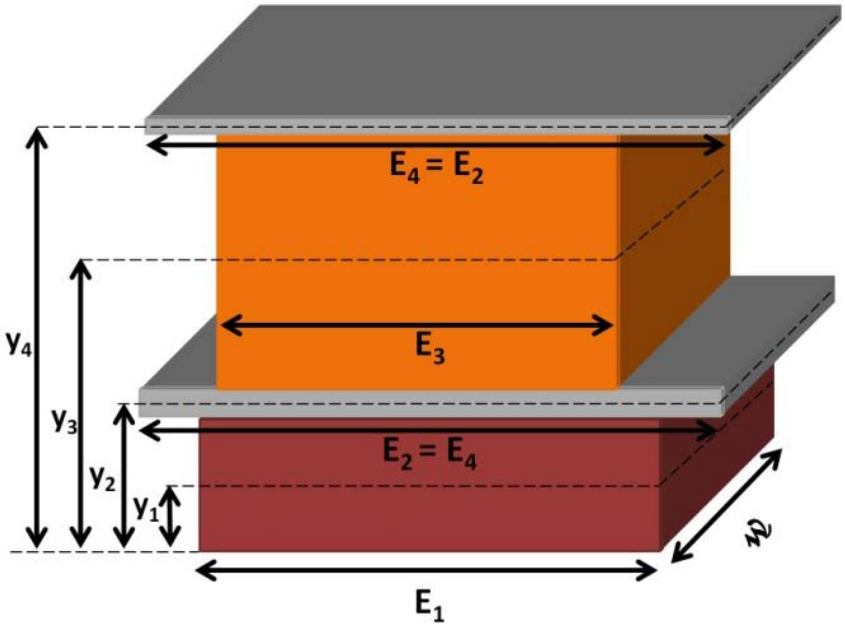

Figure 10. Composite piezoelectric stack highlighting the mid-point positions within each layer with the bottom of the stack representing y=0.

The neutral axis (Y_{cent}) in the stack shown in Figure 10 is calculated by:

$$Y_{cent} = \frac{\sum_i M_i y_i}{\sum_i M_i}$$

$$M_1 = E_1 \omega h_1$$
$$M_2 = E_2 \omega h_2$$
$$M_3 = E_3 \omega h_3$$
$$M_4 = E_4 \omega h_4$$

$$Y_{cent} = \frac{(M_1 y_1) + (M_2 y_2) + (M_3 y_3) + (M_4 y_4)}{M_1 + M_2 + M_3 + M_4}$$

2.5 $PbTiO_3$ and $PbZrO_3$ Individually

Prior to the discovery of the useful properties of PZT ceramics as piezoelectric materials, $PbTiO_3$ and $PbZrO_3$ were individually used as lead pigments in the 1940's [34]. $PbZrO_3$, a perovskite crystal, was heavily studied in the early 1950's with work by Shempard Roberts [35] showing some of the earliest results stating that it was a ferroelectric material due to its dielectric variations as a function of temperature when compared to $BaTiO_3$. In 1951, $PbZrO_3$ was proven to be an antiferroelectric material by Shirane *et al* 1951 due to anomalous hysteresis loops unlike those seen by ferroelectric materials [36]. Antiferroelectric materials exhibit a polarization due to a shift in internal electrical dipoles, like ferroelectric materials. However, the individual polarization vectors for each crystal alternate direction throughout the entire film, leading to a net polarization at zero applied electric field.

$PbTiO_3$, also a perovskite crystal exhibiting ferroelectric properties, was heavily studied in the 1930's, in particular its physical and chemical properties were investigated by Cole and Espenschield in 1937 [37]. When $BaTiO_3$ was discovered in 1935 by Busch and Scherrer [38] it soon led a push to find novel ferroelectric materials when Wainer and Salomon discovered and then patented unusual dielectric properties of $BaTiO_3$ at high temperatures in 1945 [39]. In 1951 the some work was performed in both $PbTiO_3$ and $PbZrO_3$ together as solid solutions (PZT) by Shirane *et al* [40], [41]**.** They determined that the phase diagram for the PZT material at the different Zirconium and Titanium ratios could be divided into three distinct sections; the antiferroelectric region at the $PbZrO_3$ area, the paraelectric region above the Curie temperature where the perovskite structure of PZT is cubic, and the ferroelectric

region at increasing concentrations of Titanium. A thorough investigation on the composition spread of PZT was performed by Jaffe *et al* in 1954 [42] it was through this research as well as the initial work by Shirane and Takeda [40] that the morphotropic phase boundary was discovered, region where the rhombohedral and tetragonal perovskite unit cells can coexist. There was some research on a combination of $BaTiO_3$, $PbTiO_3$, and $PbZrO_3$ to further improve the dielectric constant of the material however research by Ikeda in 1959 showed that the addition of Ba to the PZT system actually lead to a lowering of the Curie temperature and a reduction in the ferroelectric effect of the material [43].

2.6 The Morphotropic Phase Boundary – Monoclinic Phase

The phase diagram for PZT has remained relatively unchanged since it was determined by Jaffe *et al* [44] with the exception of the discovery of a few low symmetry phases at the antiferroelectric to ferroelectric transition [45] and a monoclinic phase within the morphotropic phase boundary region, discovered by Noheda *et al* [46]. The morphotropic phase boundary (MPB) which allows for the coexistence of both rhombohedral and tetragonal unit cells, has also been known to exhibit heightened material properties. The MPB is not a distinct composition line since it has a width associated to it around the Zr/Ti ratio 52/48 as shown in Figure 11. The MPB may also be shifted from the PZT (52/48) composition and the width affected by adding dopants to the system [47].

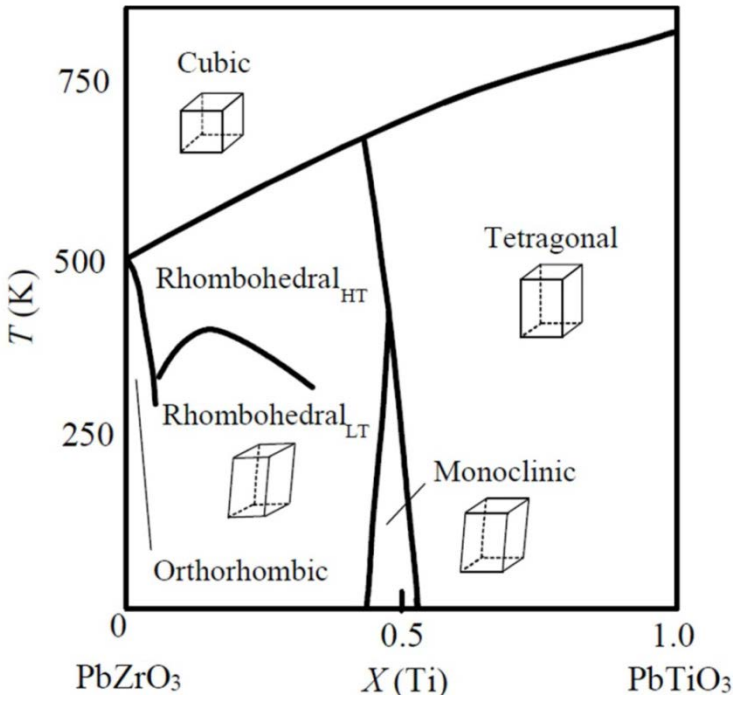

Figure 11. Phase diagram for PZT with the monoclinic phase region **[48]**.

2.7 Deposition Techniques

In the time between the discovery of the PZT ferroelectric properties and the mid 1980's the vast majority of research and device designs were using bulk PZT, several hundred microns thick, prepared by using vacuum systems. While this worked for some systems, problems with the material cracking, thickness uniformity, and composition control posed severe problems in manufacturing. In 1985 Budd *et al* developed a method to create thin PZT films using chemical solution deposition, sol-gel [49], as an alternative to the vacuum system deposition methods. Two years later in 1987 they proved the ability to deposit PZT sol-gel films with compositions at the morphotropic phase boundary PZT (53/47) [50]. Various deposition methods have been utilized in both research and industry in attempts to alter the material properties or to control composition, uniformity, and film density.

2.6.1 Metallorganic Chemical Vapor Deposition (MOCVD)

Metallorganic chemical vapor deposition, MOCVD, uses ultra pure gases which are then injected into a reactor and a thin layer of atoms are deposited onto a sample after which surface reactions cause the crystal growth. In PZT deposition, MOCVD allows for high step coverage, fast deposition rates, and good uniformity [51]. Some studies have shown MOCVD deposited films experienced high leakage currents [52] and difficulties controlling film composition[53].

2.6.2 Sputter Deposition

Sputter deposition, a form of physical vapor deposition, allows for a PZT target of a specific stoichiometry to be volatilized and condensed onto the surface of a substrate. Some key benefits of sputter deposition are low surface roughness, high crystallinity [54], and the ability to perform low temperature depositions (< 500°C) for integrated ferroelectric memory devices and avoid interdiffusion problems [55] [56].

Although sputtering allows for low temperature deposition, it still suffers from lead loss during deposition at high temperature depositions [57] and each constituent element in the target and any dopants have different sputter yields during deposition. A few other disadvantages are low deposition rates and a composition change between target and deposited film [58]. There is also an inability to change film chemistry without changing targets which is time consuming and costly.

2.6.3 Chemical Solution Deposition (CSD)

Of all the deposition processes commonly used, and described above, chemical solution deposition, namely sol-gel, allows for easier composition control and fabrication of large area thin films. It is also low cost and in industrial settings involves a short fabrication cycle as there is no need for vacuum deposition [59]. There are different techniques used to process the PZT sol-gel solutions but the three most widely used [60] involve chelate processes using acetic acid [61][62], metallorganic decomposition using water insensitive metal carboxylate compounds [63] [64], and the 2-methoxyethanol route as the solvent [65][66].

Chelate and metallorganic decomposition processes prove to be water soluble and somewhat safer for use during synthesis, while 2-methoxyethanol, toxic to bone marrow [67] and a teratogen [68], is the most widely used due to its ability to solubilize a variety of starting reagents. Chelate processes, while water insensitive, over time, the solution experiences degradation. Metallorganic decomposition requires proper concentration control to prevent film cracking due to large weight loss and shrinkage [60]. Each method has its benefits over the other, however for the purpose of this study, only PZT using 2-methoxyethanol as the solvent is discussed.

2.8 The Need for Material Improvements in PZT

The ability to use PZT in MEMS devices had opened new pathways towards novel device architecture. Optimizations of the materials are theorized to improve the electrical and piezoelectric properties of PZT [69][70]. There is a need to create large force, large displacement actuators for mm-scale robotics, RF MEMS switches, and phase shifters. The actuator performance for each of the applications can be significantly improved by increasing the piezoelectric coefficient *(section **2.3.2**).*

2.7.1 Orientation Control in PZT Thin Films

In work performed by Du *et al* [71] the dependence on the dielectric properties and film orientation was calculated. It was determined that at the extremes, around the tetragonal PZT (40/60) and rhombohedral PZT (60/40), both exhibited maxima d_{33} values in the spontaneous [001] and [111] directions, respectively. In the case of PZT (60/40) the [111] polarization direction is close to the [001] perovskite direction.

The work by Du *et al* [71] closely matches the experimental work by Berlincourt [72]. The theoretical work was further confirmed in work by Ledermann *et al* [73] who showed the $e_{31,f}$ in {111} and {100} textured PZT films. The results showed the piezoelectric response around the morphotropic phase boundary (MPB) in films that were {100} oriented was significantly higher than the {111} textured films; ~12 C/m^2 for {100} texture films compared to ~7 C/m^2 for {111} textured films. There are a number of reports by research groups who have found improved properties from {100} oriented PZT films at the MPB[74][63][71][32][75] .

The (001), c-axis, orientation is not straightforward to achieve. Although there is a substantial amount of literature that states that the preferential orientation of PZT thin films is dependent on the electrode material chosen [59][76][69], the thermal treatment and solution stoichiometry are just as vital in obtaining films of a specific orientation. Repeatability of a process is also important as film texture can vary between samples made from the same substrate [77].

Chapter 3: Processing Techniques Used for the Optimization of PZT (52/48)

3.1 Solution Fabrication

3.1.1 PZT Solution Preparation

In this research, the PZT solutions were prepared in a procedure modified from that of Budd *et al.*[49] The Pb-excess was varied to determine the best parameters for (001)-textured film growth. Lead (III) Acetate Trihydrate (99.995%) from Puratronic was weighed and mixed with 150 mL 2-Methoxyethanol (2-MOE) from Sigma Aldrich. The amount of lead (III) acetate trihydrate in a 0.4 molar PZT solution used was calculated as shown in *section 3.1.3*. In the Pb-excess study, described in *Chapter 4*, the amount of lead (III) acetate trihydrate was varied according to the percentages of Pb-excess desired in the solution (Table 1). The lead (III) acetate trihydrate and 2-MOE mixture were combined in a 1 L flask within a Labconco 50701 double glove box. A stopper was added to the flask prior to removal from the glovebox.

A separate solution using 20.5 mL of Zirconium (IV) n-propoxide (70 wt% in n-propanol) and 12.75 mL of Titanium (IV) Isopropoxide (97%), both from Alfa Aesar, was prepared using a 250 mL Erlenmeyer flask with each precursor volume added using a separate and clean pump operated graduated pipette. The volumes for these two precursors were determined as shown in *section 3.1.4* . An additional 45

mL of 2-MOE was combined with the two precursors. The solution was then stirred at room temperature on a magnetic stir plate within the Labconco glovebox.

Calculations for 220mL of 0.4 Molar PZT(52/48)			
Pb-Excess (%)	*Pb (g)*	*Zr (mL)*	*Ti (mL)*
0 %	33.38	20.5	12.75
3 %	34.38		
5 %	35.05		
8 %	36.05		
10 %	36.72		
15 %	38.39		

Table 1. Calculations for 220 mL of 0.4 Molar PZT(52/48)

While the Zr/Ti precursor solution was mixing, the 1L lead precursor plus 2-MOE mixture was removed from the glovebox and attached to a Heidolph Laborata 4000 rotary evaporator within a laminar flow hood. The rotary evaporator system was pressured with a positive pressure of nitrogen (N_2) gas (allowed to flow out of a relief valve). The flask, now attached to the unit, was lowered to a 120 °C preheated silicone oil bath and allowed to rotate at 120 rpm for 20 minutes. The N_2 gas was turned off and a vacuum was applied to the system allowing it to rotate for 20 – 25 min in a 200-300 mbar vacuum. As the solution was rotating in the oil bath, water vapor and methoxyethoxide [78] evaporate rise into the cooling coils where they condense and drop into a collection flask located under the cooling coils. After approximately 20 min, the lead acetate precipitated from the solution and changed into a white foam. At this point, the mixing flask was raised out of the silicon oil bath, and the vacuum was removed by applying N_2 gas into the system. Once the system reached atmospheric pressure, the flask was removed from the rotary evaporator and allowed to cool.

The lead foam was taken back into the glove-box where the zirconium (IV) n-propoxide, titanium (IV) isopropoxide, and 2-MOE mixture was added to it. An additional 60 mL of 2-MOE was poured into the zirconium (IV) n-propoxide, titanium (IV) Isopropoxide, and 2-MOE flask to gather any remaining solution and then poured into the lead foam flask. This step was repeated one more time; for a total of 120 mL of 2-MOE. The flask, with the combined solution, was sealed and removed from the glove box for mixing in the rotary evaporator.

Once the 1 L flask was attached to the distillation unit, the unit was lowered into the silicon oil bath and rotated at 120 rpm. The unit was allowed to rotate for 3.5 h at 120 °C. After the 3.5 h, a 925mbar vacuum was applied followed by the introduction of N_2 gas for 5 min. The flask was removed from the hot oil bath and the amount of newly made PZT solution in the flask was measured. The cooled solution was transferred into a storage container with the stirring magnet and 4% Formamide, from Sigma Aldrich, was added to the resulting PZT solution volume to act as a drying control agent. Note, the formamide is added to a cooled solution as adding formamide to a hot solution risks the decomposition of the formamide into carbon ammonia and carbon monoxide [79].The PZT container was sealed and placed on the stirring plate overnight.

3.1.2 $PbTiO_3$ Solution Preparation

The $PbTiO_3$ solution was prepared following the same process used to make PZT described above. Lead (III) acetate trihydrate was measured according to the percentage of Pb-excess desired and mixed with 150 mL of 2-MOE in a 1 L flask. In

a separate flask, 10 mL of titanium (IV) isopropoxide was combined with 45 mL of 2-MOE and allowed to stir on a magnetic stirrer while mixing and vacuum distillation was performed on the lead (III) acetate trihydrate and 2-MOE mixture, similar to the process used to PZT. Once the lead (III) acetate trihydrate and 2-MOE mixture turned into a lead containing white foam, the titanium (IV) isopropoxide and 2-MOE mixture was added to the lead containing white foam inside of the glove box. All the same steps mentioned in the PZT Preparation section were followed.

Calculations for 220mL of 0.15 Molar $PbTiO_3$		
Pb-Excess (%)	*Pb (g)*	*Ti (mL)*
0 %	12.52	10.0
10%	13.77	
15 %	14.40	
20 %	15.02	
30 %	16.27	

Table 2. Calculations for 220 mL of 0.15 Molar $PbTiO_3$

Based on discussions with the research group at Pennsylvania State University (PSU), the procedure to test the $PbTiO_3$ seed layer (PTO) required two different solutions, one with acetic acid and one without. Improved results with acetic acid were reported by PSU researchers [80]. For samples without the addition of acetic acid, the PTO seed layer was used once it finished stirring overnight. For the samples that did require acetic acid, 7% acetic acid was added to the desired volume of PTO solution and allowed to mix for 30 min on a magnetic stirrer.

3.1.3 Calculations of Pb-Excess Used in the PZT (52/48) Solutions

The mass of Lead (III) Acetate Trihydrate required to achieve a specific PZT solution molarity was determined using the equation below. In this study 0.4M PZT (52.48) was used as well as 0.15M $PbTiO_3$.

$$\text{Pb (grams)} = (X\ mol) * (379.33 \frac{g}{mol})$$

3.1.4 Calculations of Zirconium and Titanium Precursor Volumes

Volume (mL) of 97% Titanium (IV) Isopropoxide and 70% Zirconium (IV) n-propoxide used required to achieve the correct PZT (52/48) composition and molarity. The calculations were performed as follows:

$$48\%\ \text{Ti (mL)} = \frac{(0.48) * (\text{X}\ mol) * (284.26 \frac{g}{mol})}{(0.974 \frac{g}{mL}) * (0.97)}$$

$$52\%\ \text{Zr (mL)} = \frac{(0.52) * (\text{X}\ mol) * (326.56 \frac{g}{mol})}{(1.044 \frac{g}{mL}) * (0.7)}$$

3.2 Substrate and Electrodes Used

Substrates throughout this research consisted of (100) silicon (Si) wafers with a diameter of either 100mm or 150mm. First, the wafers were coated with 500 nm of thermally grown silicon dioxide (SiO_2) thin film. Next, a bottom electrode was sputter deposited onto the silicon dioxide using a Unaxis Clusterline 200 (CLC) deposition system. Initial test data involved a bottom electrode that consisted of a bi-layer of (20nm) Ti/ (85nm) Pt (referred hereon as Ti/Pt), where both metal layers were sputter deposited at 500ºC. The resulting Pt exhibited a mixed texture of (111) and (002). Subsequent data involved improvements to this bottom electrode and are reported in Potrepka et. al. [81]. The improved bottom electrode involved approximately30 nm thin layer of titanium (Ti) sputter-deposited at room temperature using the CLC deposition tool. After the Ti deposition, an oxygen anneal was performed at 750^{o}C in a Bruce Technologies tube furnace, to convert the Ti to TiO_2 with a thickness of 33 – 36 nm. A 100nm Pt film was deposited at 500^{o}C using the CLC resulting in a {111} textured Pt with a full width half maximum (FWHM) ranging from 1.8 to 3.0 degrees. Previously reported, highly {111} textured Pt (referred hereon as TiO_2/Pt) provides a template for {111} PZT textured growth when the PZT is applied directly onto the Pt [82][83][76].

3.3 Chemical Solution Deposition: Sol-Gel

3.3.1 Deposition, Spin Rates, and Thicknesses

Using a 10 mL syringe filled with the 0.4 M PZT (52/48) solution with a 0.1 μm PTFE membrane filter attached to the tip, the solution was statically dispensed onto the surface of a Pt coated silicon substrate described in the previous section. The sample was spun for 45 s at 2000 rpm on a Bibtec SP100 spin coater and then pyrolyzed on a Wentworth Laboratories vacuum hot plate for 2 min at 350 °C. Following the pyrolysis step, the film was crystallized using an AG Associates Heatpulse 610 Rapid Thermal Anneal (RTA), with internal quartz ware used only for PZT processing, for 60 s at 700 °C in a 4 °C/s ramp in flowing oxygen, ~5 sccm (Figure 12). The deposition steps were repeated until the PZT reached the desired thickness for the devices being fabricated, 500 nm was the primary focus of much of this research. The film thickness was measured using a J.A. Woollam M-2000 spectroscopic ellipsometer.

The deposition process for the samples using a 0.15 M PTO seed layer utilized a single layer of the PTO seed layer solution with a targeted thickness of 17 - 20 nm deposited directly onto the Pt surface. The seed layer was statically dispensed and then spun for 30 – 45 s at a spin rate between 2500-4000 rpm and then pyrolyzed for 2 min at 350 °C. The samples were put into the RTA for 60 s to fully crystallize the film. Initial PTO seed layer work consisted of an RTA temperature of either 700 °C or 600 °C depending on the experiment that was being performed. Following the seed layer crystallization, multiple PZT layers were deposited using the same process described above, until the desired film thickness was achieved.

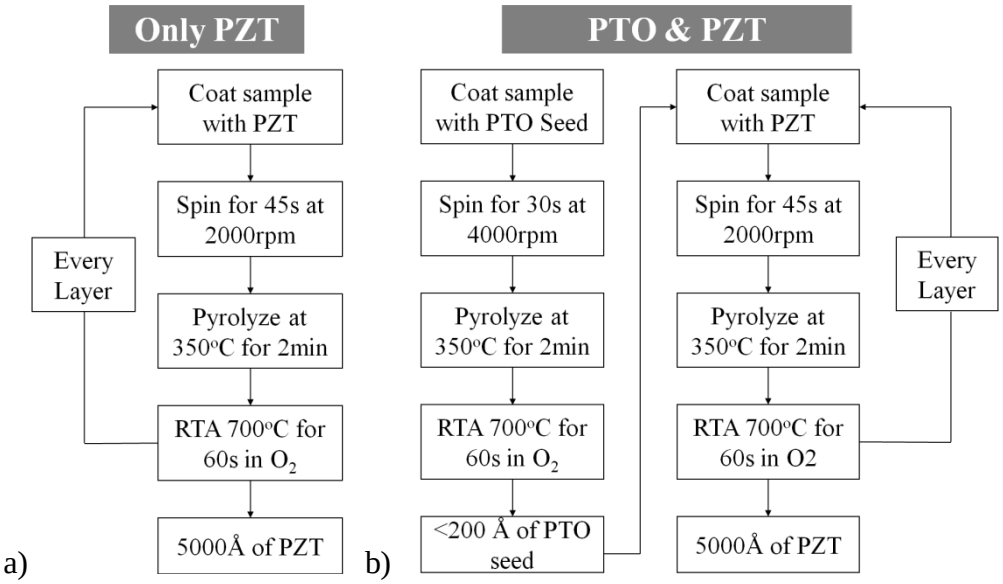

Figure 12. Standard parameters used for sol-gel deposition of a) only PZT and b) a single layer of PTO and multiple layers of PZT.

The thickness control of the PTO and PZT films depends on the Molarity (M), which influences the viscosity of the solution, and the operation of a Bibtec SP100 spin coater, namely the spin rate and spin time (Table 3). Assuming the PTO and PZT solutions initially follow Newtonian fluid dynamics, the resulting individual film thickness should be proportional to the spin speed.

Spin Rate	0.15 M PTO Thickness (nm)	0.4 M PZT (52/48) Thickness (nm)
2000 rpm	30	63
2500 rpm	21	60
3000 rpm	19	58
4000 rpm	17	55

Table 3. Comparison of spin rate on sol-gel thickness for PTO and PZT solutions per layer deposited.

3.3.2 Pyrolysis, Annealing Temperature, and Ramp Rates

The RTA conditions have a major impact on Pb-loss, which significantly affects PZT orientation [84]. Initial work on PTO and PZT orientation involved the use of a slow RTA ramp rate, Slow Ramp (hereon SR), of 4°C/sec from ~100°C to 700°C (Figure 13a). The starting anneal temperature was slightly above 100°C resulting from a pre-conditioning run in the RTA prior to annealing the PTO or PZT coated wafers. The studies on the effect of crystallization temperature on film orientation were performed at 680°C, 700°C, 720°C, and 740°C. At dwell temperatures below 680°C, the pyrochlore phase was observed previously in the PZT thin films. The Pb-deficient pyrochlore phase is undesirable as it reduces the piezoelectric properties of PZT thin films by pinning ferroelectric domains.

The pyrolysis step in sol-gel depositions is known to have an influence on the final orientation of PZT thin films, where organic materials are burned out of the films at temperatures under the films crystallization temperature, above 500°C. The current process involves using a Wentworth Laboratories vacuum hot plate temperature of 350°C for 2 minutes. Using a rapid ramp anneal process (RR), sample is heated at ~199°C/sec up to 700°C and held for 60 sec (Figure 13b), 4 pyrolysis temperatures were studied to see the effect, if any, on film orientation. The temperatures used in this study were 350°C, 400°C, 430°C, and 450°C. An attempt at a 500°C pyrolysis was made however hotplate temperature control above 450°C proved to be difficult with 15°C temperature fluctuations. Films were deposited at the specified pyrolysis temperatures and annealed using RR conditions at 700°C. XRD measurements were performed to observe film orientation.

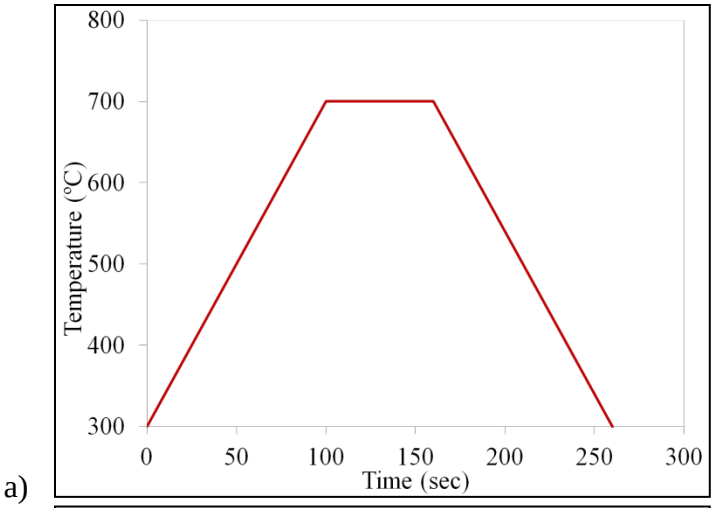

a)

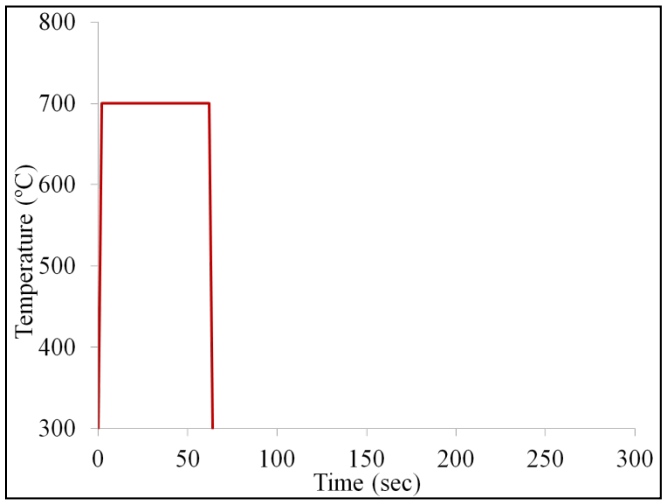

b)

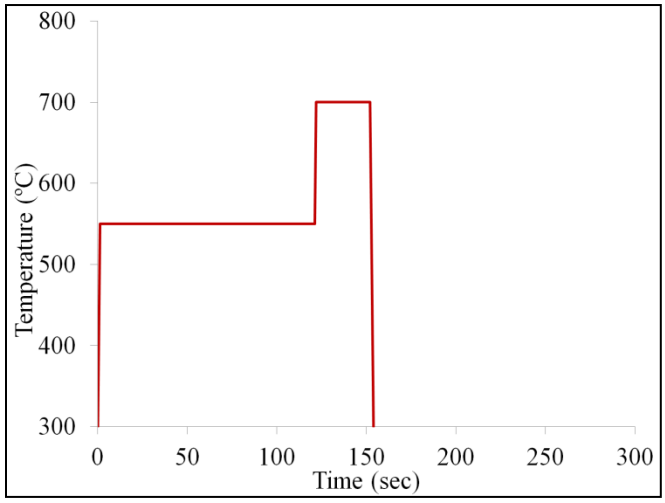

c)

d)

Figure 13. The RTA temperature-time profiles used in this study included a) slow ramp (SR) with a 4°C/sec ramp to 700°C, b) rapid ramp (RR) with a 199°C/sec ramp, and c) double ramp with 199°C/sec ramp up to 550°C followed by a 2 minute hold before a second 199°C/sec ramp to the final crystallization temperature of 700°C.

3.4 Device Fabrication

3.4.1 500 µm x 500 µm Square Capacitors on 25 cm Square Substrates

In order to quickly fabricate capacitors within a day, a 100 mm wafer with the bottom electrode already deposited was cleaved into several pieces using a diamond scribe. Small test substrates of approximately 25 cm x 25 cm were used. After the PTO and PZT deposition, following the procedures described in Figure 12, 500x500 µm square capacitors were fabricated for electrical testing. The samples were coated with Clariant AZ5214E photoresist in a stationary spinner chuck and spun at 2000 rpm for 40 s. Spinning the sample allows for the application of a uniform layer of photoresist as the centrifugal forces expels excess resist from the edge of the sample. After the coating, the samples are placed on a hot plate for 60 s at 110 °C. The resist was exposed for 2.1 s under low vacuum contact using a Karl Suss MA/BA6 contact aligner using a test mask comprised of an array of 500 x 500 µm squares. After this first exposure, a post exposure bake was performed at 120 °C for 30 s. Following the bake, a flood exposure of 3.5 s was done to achieve an image reversal to create a re-entrant sidewall profile (Figure 14). After exposure, the resist was developed using an AZ 300MIF developer for 75 s followed by inspection under a microscope.

With the resist patterning complete, a top Pt layer was sputter deposited on the samples to serve as a top electrode during electrical testing of the PZT capacitors. The Pt was deposited using a Varian 3190 DC magnetron sputter system to deposit approximately 1000 Å of Pt. After deposition, the samples were placed in an acetone bath to remove excess metal and resist using a liftoff technique. Using a resist with a re-entrant sidewall allows the Pt deposited in the 500 x 500 µm squares to be

removed while the excess Pt and resist is removed. The liftoff process took approximately 30 min and then the samples were rinsed with methanol, isopropyl alcohol, and finally de-ionized water.

To open access to the bottom Pt, the samples were again coated with photoresist and the resist in one corner of the sample was removed with acetone. The open corner was then exposed to a wet etch solution to remove the PZT, thereby revealing the bottom Pt layer. The etch solution consisted of 240 mL of distilled water, 120 mL of hydrogen chloride (HCl), and 1 mL of hydrogen fluoride (HF). The area to be etched was dipped into the solution and agitated for several seconds until the bottom Pt electrode was visible and appeared clean. The sample was rinsed with liberal amounts of de-ionized water. After the wet etch process, the remaining resist was removed using oxygen plasma for 25 min. The resulting capacitors were annealed in the RTA at 350°C for 2 minutes in flowing O_2.

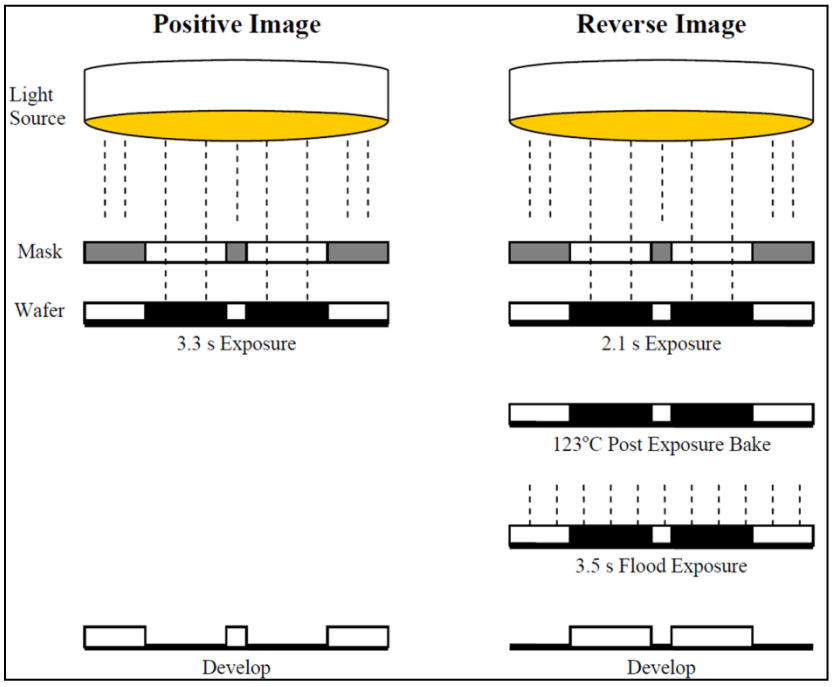

Figure 14. Schematic of positive and reverse photolithography process using AZ5214 photoresist.

3.4.2 Full Wafer Fabrication of Cantilever Arrays and Capacitors

Using the procedures described previously on either 100mm or 150mm wafers, the stack shown in Figure 8 in *section **2.3.3*** was fabricated. Cantilever actuator arrays and capacitors began processing with a coating of AZ5214E resist using a Karl Suss ACS200 Wafer Coater/Developer (ACS200). Using a Karl Suss MA/BA6 Contact Aligner, a positive exposure of the resist was performed for mask level 1 to define the top Pt electrode. The wafer was developed in the ACS200 using AZ300MIF developer. Resist was manually removed along the edge of the wafer in preparation for the ultraviolet (UV) cure of the resist. During the spinning process, surface tensions along the edge of the wafer cause a thicker layer of resist (aka edge bead) to be formed. This thickened layer tends to fracture and create particulates during the UV curing process in which evolved gases attempt to escape from the curing resist. A clean cloth moistened with acetone was placed in the hood and the wafer was rolled over the acetone to remove edge bead resist. A 5-min descum using the Metroline/IPC Plasma Photoresist Stripper removed any un-patterned resist that remained on the wafer. The UV cure was accomplished using an Axcelis UV photostabilizer in which a combination of 220°C heat and UV light are used to cure the resist. The heat softens the resist, allowing impurities to escape in gaseous form while the temperature is ramped to cure and hardened the resist. This prepares the wafer for the first ion mill step using a 4wave 4W-PSIBE Ion Beam Etch system (Figure 15a).

During the Argon ion mill process, the top Pt layer that is not covered with resist is removed, exposing the PZT beneath (Figure 15b). The 4wave Ion mill etch system used a secondary ion mass spectrometer (SIMS) endpoint system which allowed for the detection of the Pt ions as the Pt was etched away. After this process, the wafers underwent a 25 min ash in the Metroline that removed all the resist from the wafer (Figure 15c). Next, the second mask level is patterned using the same procedure outline previously with the addition of an alignment of Mask 2 to Mask 1. Mask level 2 defines the PZT actuator by removing excess PZT and bottom metal (Ti/Pt or TiO_2/Pt) using the Ar ion mill and the SIMS endpoint system (Figure 15e). Following the etch, another 25 min O_2 plasma ash was performed to remove all resist (Figure 15f). At the conclusion of the patterning with Mask level 2, the elastic layer deposited earlier is now exposed on a vast majority of the wafer.

To expose the bottom Pt layer, a PZT wet etch is performed after patterning the next part of the circuit with a reverse exposure of the AZ5214 photoresist. The wafer is again placed into the Ar ion mill to etch away the exposed PZT and using the SIMS endpoint system, etching was stopped once the bottom Pt electrode ions were detected. A new PZT wet etch solution, described in an earlier section, was made to ensure a quick and clean wet etch. The mixture was placed into a Teflon container into which the wafer could fit and a similar glass container was filled with de-ionized water and used to end the PZT etch reaction. The wafer was placed into the PZT wet etch mixture and agitated for 5–15 s. Color changes were observed on a large bottom metal pad from the traces of PZT still on the pad; the wafer was immediately removed from the PZT wet etch mixture when the pad appeared clean of any residual

PZT and was placed into the de-ionized water container. Water was allowed to run over the wafer to completely end the reaction and then it was dried using N_2 gas. The wafer was inspected to ensure that the PZT was completely etched through and that the circuit features were not damaged or over-etched since this could cause a short-circuit (Figure 15g). A 25-min O_2 plasma ash was performed to remove all resist from the wafer (Figure 15i).

Next, an oxide reactive ion etching (RIE) was performed on the exposed elastic layer which enabled access to the Si substrate for the final release step. For this process, a reverse image exposure (Figure 14) was performed followed by a 5-min O_2 descum to remove un-patterned resist (Figure 15j). A Lam 590 Oxide/Nitride Etch (Lam 590) was used to etch the elastic layer using a combination of 30 sccm CHF_3, 90 sccm CF_4, and 170 sccm He gases, at a pressure of 2800 mT and 800 W power. This etching process causes damage to the bonds removing the elastic layer. Using an SiO_2 elastic layer, the gases used in the Lam 590 chemically reacts with the Si to convert it into SiF_4, the O into O_2 or H_2O. The elastic layer can also be composed of alternating layers of silicon oxide and silicon nitride to create stiffer beams and devices as per device needs. The Lam 590 etching gasses will react with the SiO_2 as described as well as convert the N into N_2 on the wafer. The sample was inspected with a microscope to ensure the etch completely removed the elastic layer and exposed the underlying Si substrate (Figure 15k). After etching, a 25-min ash was performed (Figure 15l).

The final mask pattern defines a Ti and gold (Au) bi-layer metallization using a reverse exposure (Figure 15m). An Evatec BAK 641 Electron Beam Evaporator deposited 200 Å of Ti followed by 3000 Å of Au (Figure 15n). This will protect the contact pads during electrical testing from getting scratched by the electrical probes. The entire wafer was covered with Ti and Au and an acetone liftoff was required to remove all Ti and Au that was attached to the resist. This results in Ti and Au remaining in the areas that were not covered with resist (Figure 15o). A 5-min O_2 plasma ash was performed to remove any resist residues from the wafer.

Throughout the processes mentioned, the cantilever array was slowly being formed. Finally, 20 s etch in the Lam 590 was performed to remove any native SiO_2 from the exposed Si substrate, followed by a XeF_2 isotropic etch using a Xactix Xetch (Figure 15p). This process etches the Si substrate, undercutting and releasing the cantilevers from the substrate, and does not damage the other layers on the wafer. The cantilever beams are now fully released and ready for testing.

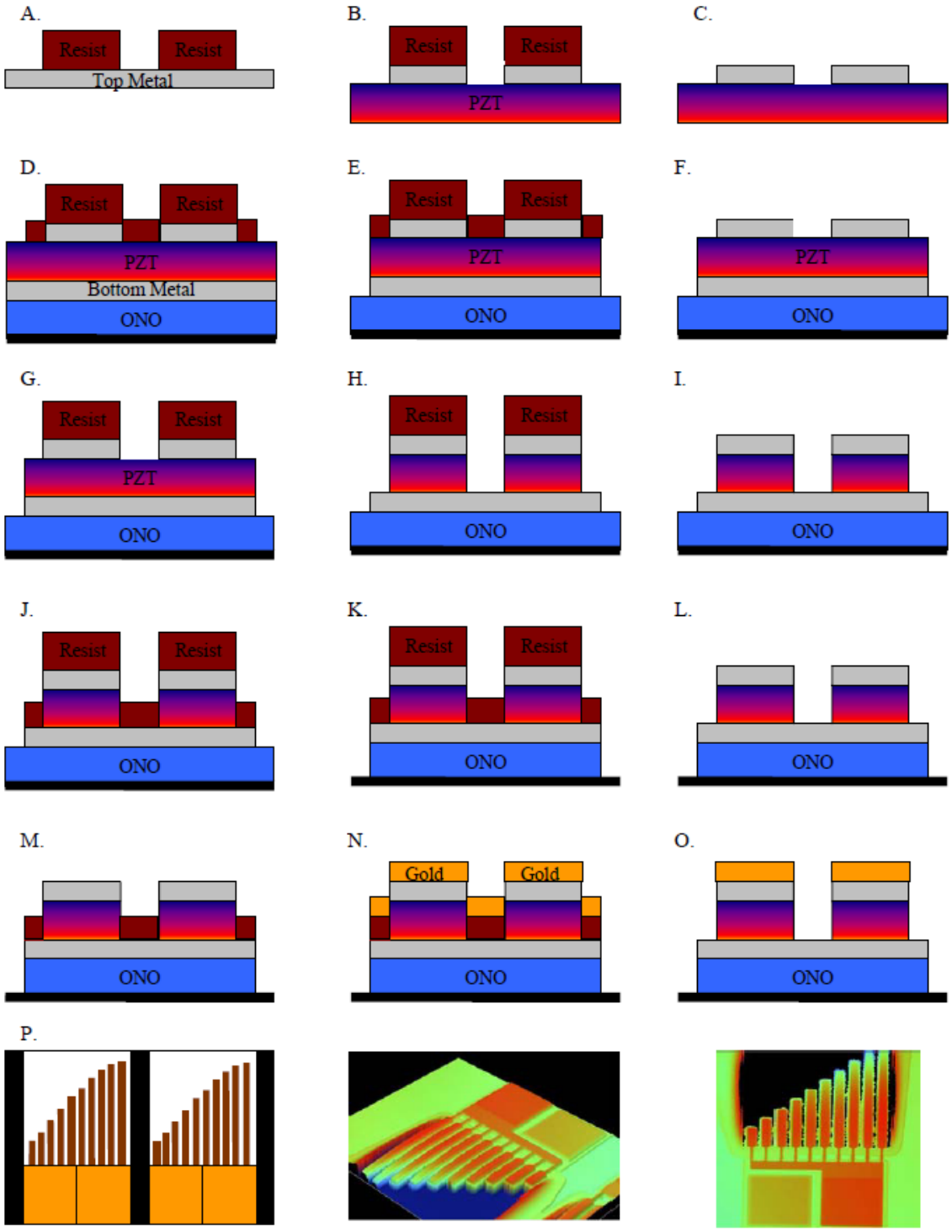

Figure 15. (a) Top metal pattern, (b) 1st ion mill, (c) After 25 min ash, (d) PZT/bottom metal pattern, (e) 2nd ion mill, (f) After 25 min ash, (g) PZT wet etch pattern, (h) After PZT wet etch, (i) After 25 min ash, (j) Oxide RIE pattern, (k) After oxide RIE, (l) After 25 min ash, (m) Ti/Au deposition pattern, (n) After Ti/Au deposition, (o) After acetone liftoff, and (p) XeF_2 etch releases cantilever.

Chapter 4: Improving PZT (52/48) Thin Film Texture through Improved Platinum Metallization and Seed Layers

4.1 Initial Work Using a $PbTiO_3$ Seed Layer for Orientation Control

To evaluate $PbTiO_3$ as a seed layer for inducing (001) PZT orientation, single-sided polished 100 mm silicon (Si) wafers were utilized. First, a 200 nm thick silicon dioxide (SiO_2) to be used as an elastic layer was deposited using a Plasma Them 790 plasma enhanced chemical vapor deposition (PECVD) system. The SiO_2 thickness was measured with a J.A. Woollam spectroscopic ellipsometer to within ± 20 nm thickness deviation. The wafers were then annealed using an A.G. Associates Heat Pulse 610 Rapid Thermal Anneal (RTA) furnace at 700 °C for 60 s in approximately 6 sccm flowing N_2 gas. The bottom electrode was sputter deposited using a Unaxis Clusterline 200 system (CLC). The bi-layer bottom electrode consisted of 20 nm titanium (Ti) and 85 nm platinum (Pt) deposited at 500°C. The wafers followed the chemical solution deposition processing procedure for both the PTO and PZT outlined in *section **3.3***.

4.1.1 X-ray Diffraction and Hysteresis Results of Using a $PbTiO_3$ Seed Layer

Initial testing was performed on 25 cm x 25 cm square samples cleaved from the 100 mm Si wafers previously prepared. The first tests consisted of analyzing the effects of RTA temperature and use of acetic acid on the single layer PTO film. A control sample using 500 nm PZT (52/48) without the PTO seed layer annealed under

slow ramp (SR) annealing conditions (Figure 13a). The sample labeled as Seed Test 1 in Table 4 used 20 nm PTO with 7 % acetic acid added to the PTO solution approximate 30 minutes before PTO deposition. The film was annealed in the RTA at 700°C for 60s followed by deposition of 500 nm of PZT (52/48). Seed Test 2 and 3 in Table 4 followed a similar procedure as Seed Test 1 with the exception that the PTO seed layer was annealed at 600°C instead of 700°C and in Seed Test 3 no acetic acid was used in the PTO seed layer.

Control Sample	• No PTO used • 500 nm of PZT (52/48) • 700°C RTA
Seed Test 1 – with Acetic Acid	• 20 nm PTO used • 700°C RTA • 500 nm of PZT (52/48) • 700°C RTA
Seed Test 2 – with Acetic Acid	• 20 nm PTO used • 600°C RTA • 500 nm of PZT (52/48) • 700°C RTA
Seed Test 3 – without Acetic Acid	• 20 nm PTO used • 600°C RTA • 500 nm of PZT (52/48) • 700°C RTA

Table 4. Initial $PbTiO_3$ Seed Layer tests examining the effects of annealing temperature and use of acetic acid on orientation and electrical properties.

X-ray diffraction measurements, XRD, using a Rigaku Ultima III diffractometer with Bragg-Brentano geometry, were performed on a Ti/Pt sample with a 250 nm PTO thin film to determine the crystalline structure of the film (Figure 16). The film showed a mixed texture of (001) and (110) orientations. The preferred seed layer should consist of solely (001) PTO as it will allow for templating of (001) PZT. Even with a mixed orientation, it was anticipated that the PTO seed layer would result in a greater degree of texturing within the PZT thin film.

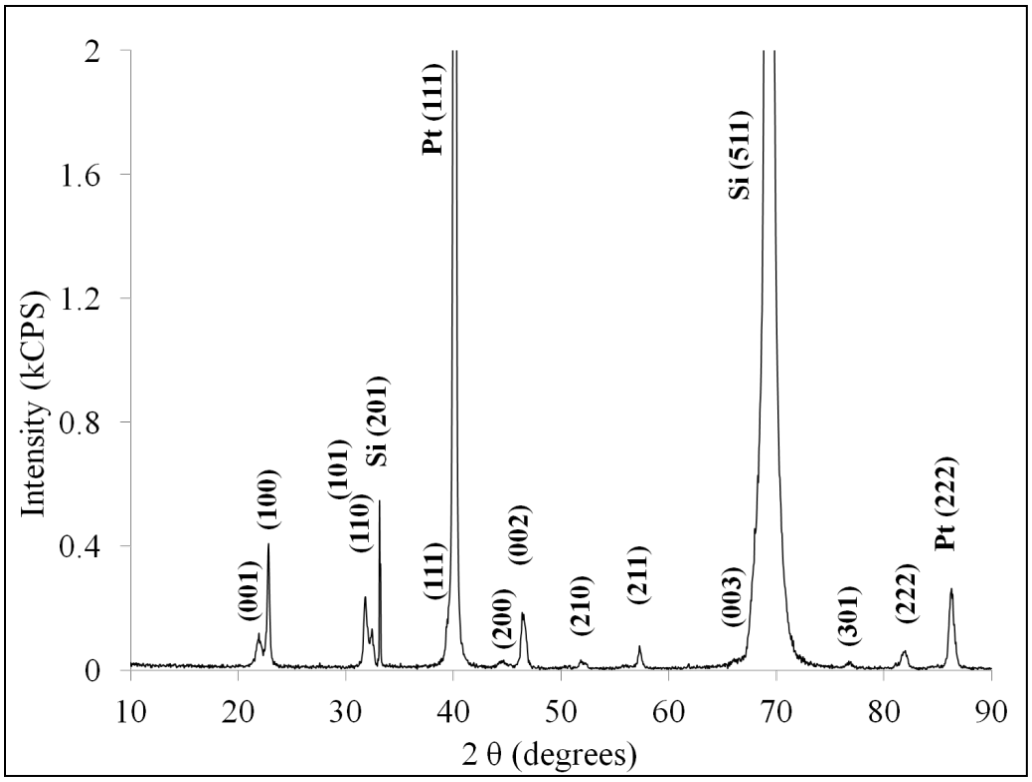

Figure 16. XRD of 250 nm PTO on a Ti/Pt electrode

Simple parallel plate capacitors were fabricated on the samples outlined in Table 4. Hysteresis measurements were performed on the capacitors using an HP Multi-Frequency LCR Meter 4275A at 10 kHz with an excitation signal of 50 mV and a Radiant Technologies RT-66a measurement unit. The capacitors were poled

with a poling voltage of 10 V for 2-3 minutes prior to being measured. For the different growth conditions, very little change was observed in the polarization-electric field hysteresis loops (Figure 17). Small subtle changes in the saturation polarization, remnant polarization, and coercive fields are attributed to sample variances and are within the assumed standard deviation for these measurements. In contrast, the dielectric properties for the different films show more significant changes between the processing conditions. The two PTO solutions that were selected for additional testing were the 700°C and 600°C annealed samples with acetic acid mixed into the solution, Seed Test 1 and 2, due to their higher dielectric constants of 1299 and 1354, respectively.

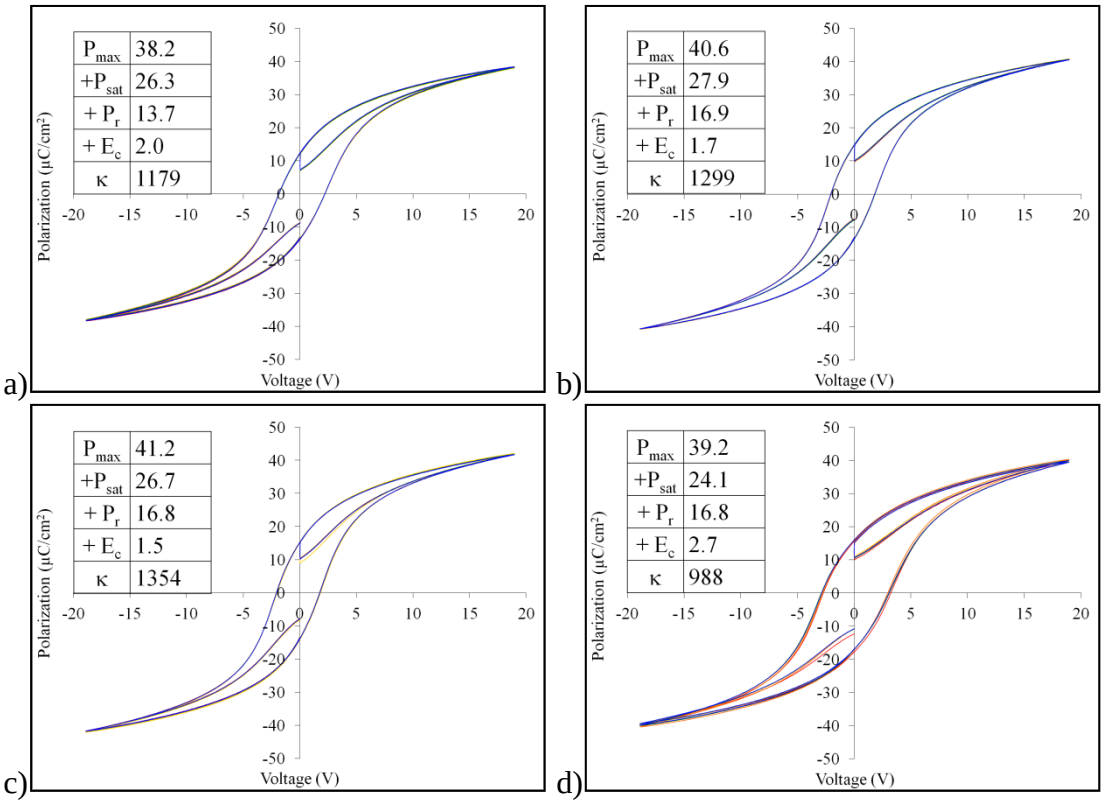

Figure 17. PE hysteresis measurements performed on a) PZT (52/48) b) Seed Test 1 c) Seed Test 2 and d) Seed Test 3.

The higher performing conditions were then selected for additional testing using cantilever devices to measure the piezoelectric induced deformation as described in *section 3.4.2*. Prior to the fabrication of the cantilever devices, XRD measurements were performed to determine the crystallinity of the PZT thin films with the PTO. XRD of the PZT (52/48) control sample showed a mixed texture with strong random order phases and significant (111) orientations (Figure 18a). Using the PTO seed layer in samples Seed Test 1 and 2, reductions in the (110) and (111) peaks are observed (Figure 18 b & c). In addition, peak broadening and the beginnings of peak splitting of the (001) and (100) peak are observed in samples with the PTO seed layer.

a)

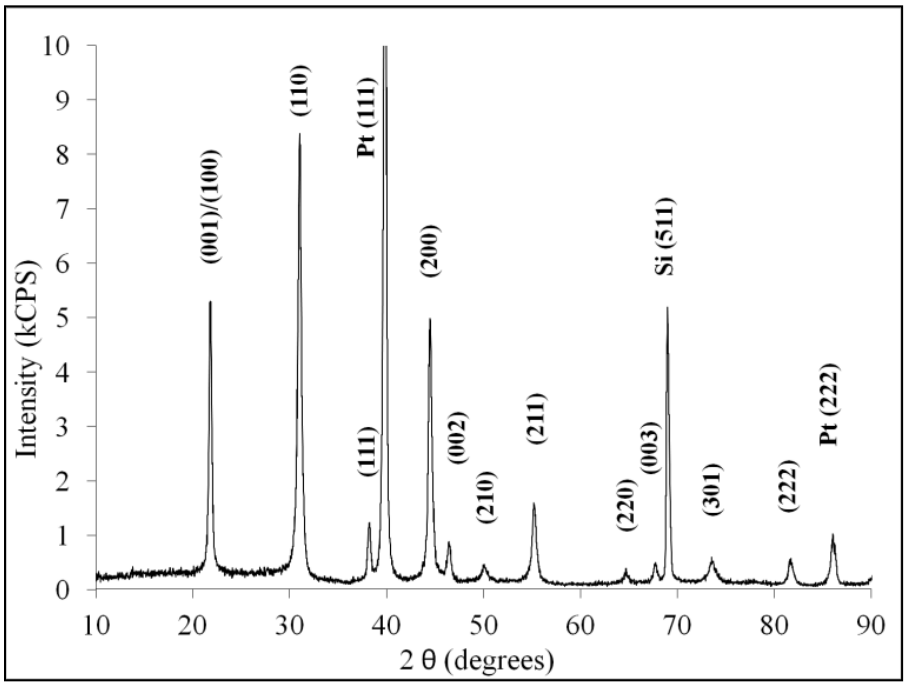

b)

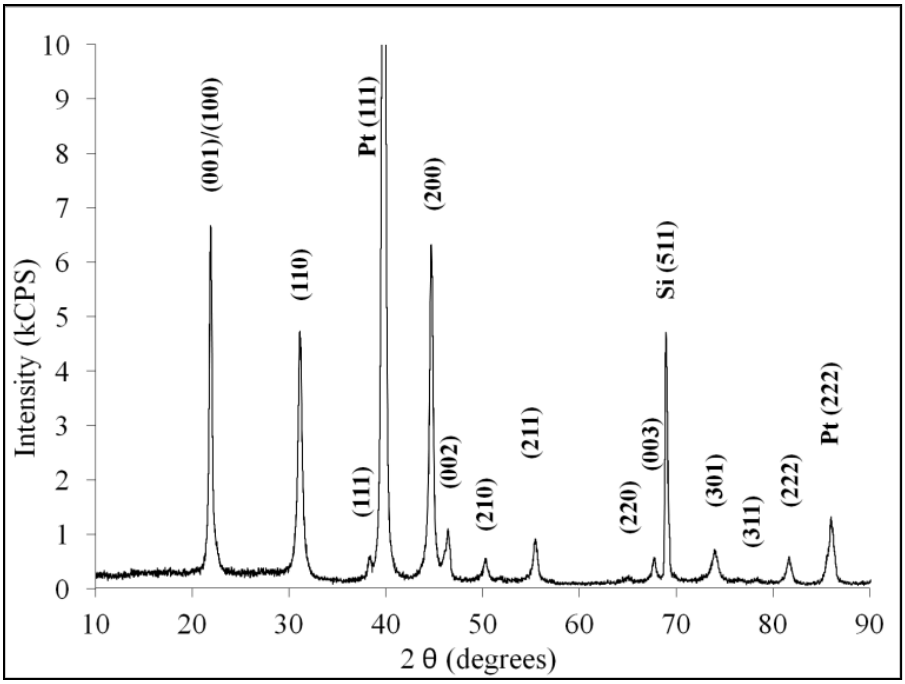

c)

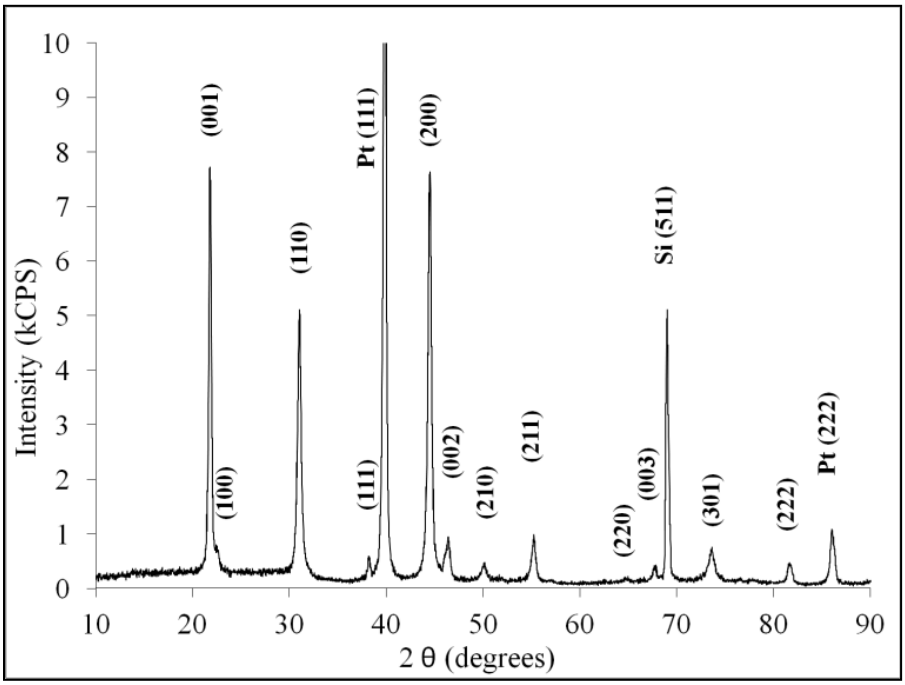

Figure 18. XRD with peak labeling of a) Ti/Pt/PZT control sample b) Ti/Pt/PTO (700°C anneal)/PZT and c) Ti/Pt/PTO (600°C anneal)/PZT

4.1.2 Cantilever Displacement Results of Using a $PbTiO_3$ Seed Layer

Cantilever arrays were fabricated following the device procedure outlined in the *section 3.4.2*. The cantilever structures were used to analyze the effects of PZT stoichiometry and texture on the displacement properties of the PZT thin films. In previous studies PZT (45/55) has shown higher piezoelectric coefficients compared to PZT (52/48) due to the random crystalline texture of the existing material [85]. A test sample using PZT (45/55) without a PTO seed layer was prepared for comparative purposes, however, the two samples with the PTO seed layer and PZT (52/48) show noticeable improvements when compared to the PZT (45/55) sample without the PTO seed layer. The 4 test samples underwent piezoelectric actuation comparison tests collected using a Wyko optical profilometer between 0 and 20 V. Data was collected from cantilevers 1, 2, and 3 (83 μm, 107 μm, and 132 μm lengths, respectively) by actuating the beam and measuring the out of plane deflection of the beam as a function of the applied voltage (Figure 19). There is a dramatic improvement in the displacement metrics, approximately double, in both PTO seed layer samples over control sample with PZT (52/48) and there is approximately a 20% improvement compared to control sample with PZT (45/55) (Figure 20). Ultimately, the sample with the Ti/Pt/PTO (700°C anneal) / PZT (52/48) exhibited the highest displacement measurements of all the samples.

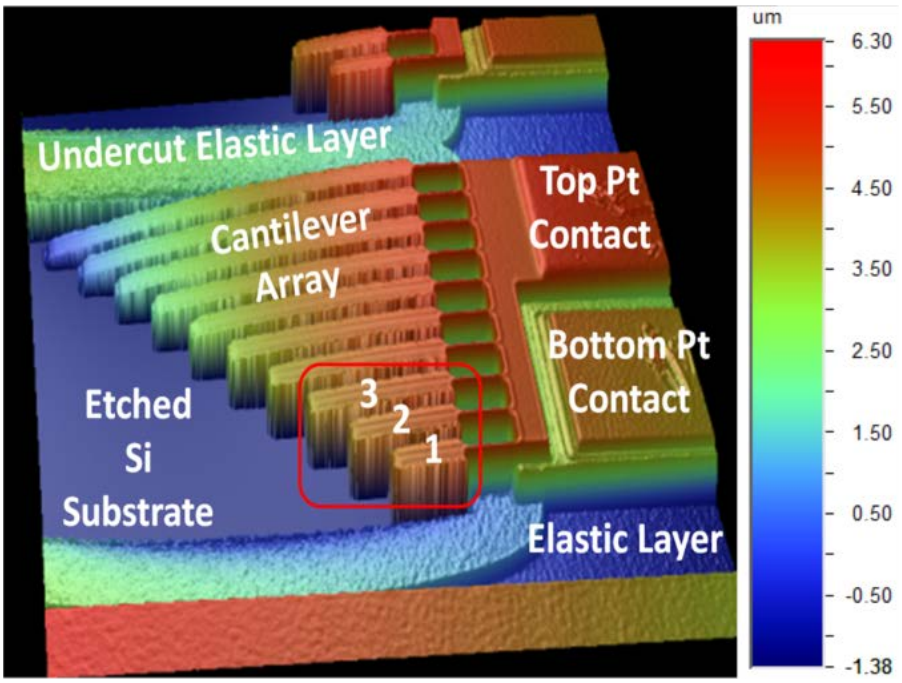

Figure 19. 3D image of the cantilever array taken by the Wyko optical profilometer.

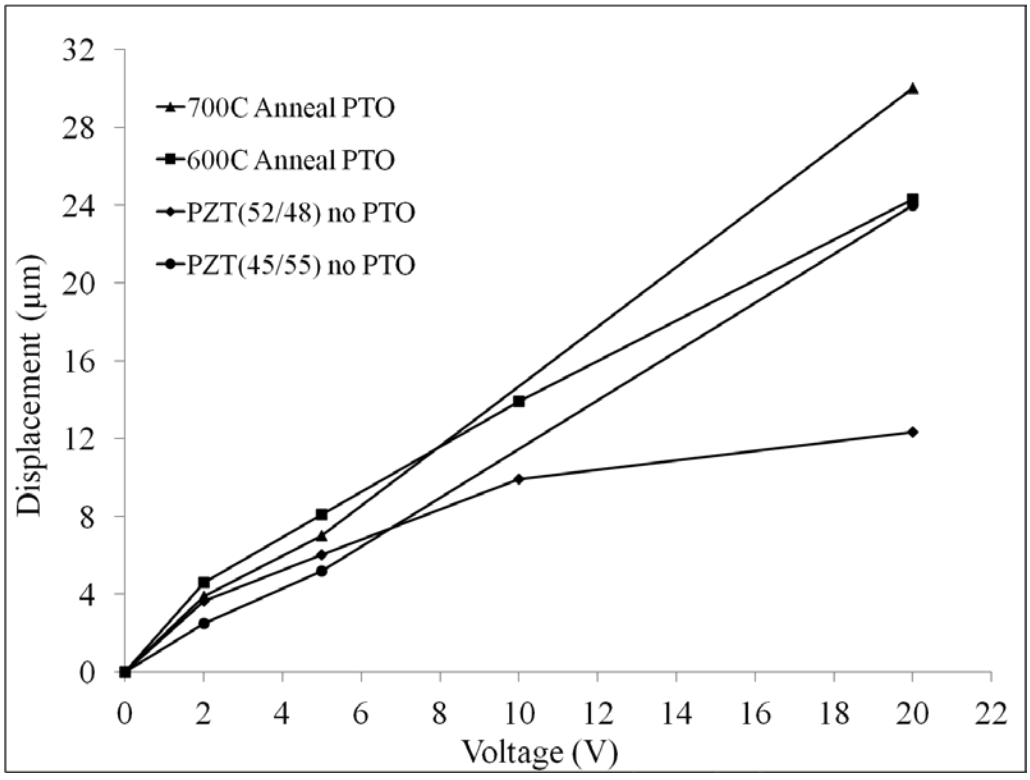

Figure 20. Summary of the cantilever displacements as a function of voltage.

One additional note is that although the cantilevers were prepared in similar techniques and the cross-sections were very similar, the static deformations of the samples with the seed layers were dramatically different from the control sample. The added texture component in the samples with the PTO seed alters the overall residual stress gradient resulting in a shift from a negative (in-wafer) curvature to a positive (out-of-wafer) curvature. This change is noted as it can have a dramatic influence on the functionality of certain MEMS devices (e.g. switch/relay functionality can be adversely affected by a significant change in static deformation state).

4.2 Effects of Platinum Electrode Optimization on PZT (52/48) Orientation

To further improve the PZT texture, the bottom electrode metallization was changed from Ti/Pt to TiO_2/Pt (Figure 21). Some research has shown that the TiO_2 adhesion layer promotes more strongly (111) textured Pt as well as influences the PZT texture [86]. The higher quality Pt results in significant improvements in the orientation of the PZT deposited on the highly {111}-textured Pt.

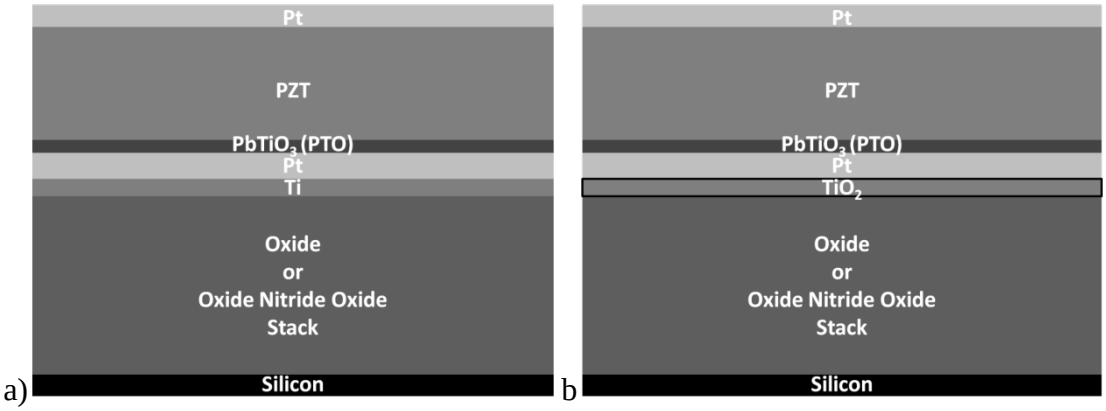

Figure 21. Pt/PZT/Pt stack using different bottom electrodes a)Ti/Pt and b)TiO_2/Pt.

4.2.1 X-Ray Diffraction of Ti/Pt and TiO_2/Pt

In order to quantify the percentage of orientation in the film, the Lotgering factor was used [87]:

$$f = \frac{P - P_0}{1 - P_0}$$

$$P = \frac{[I_{(001)} + I_{(002)} + I_{(100)} + I_{(200)}]}{\sum I_{(hkl)}}$$

P_0 = XRD intensity values based on a standard
P = XRD intensity values based on actual sample
$I_{(001/100)}$ = Intensity of (001) and/or (100) peaks
$\sum I_{(hkl)}$ = Sum of all PZT peaks

The Lotgering factor (f) used the peak intensities from x-ray diffraction data using a Rigaku Ultima III Diffractometer Bragg-Brentano geometry**.** The peaks of interest are the (001), (100), (002), and (200). Using a powder diffraction file (PDF) standard for PZT near the MPB (PDF#00-050-0346) the experimental values and the standard values allow for the percentage of orientation, Lotgering factor, in the {100} direction to be determined.

Rigaku Ultima Diffractometer Parameters	
Divergence Slit	2/3
Divergence H.L. Slit	10 mm
Scattering Slit	2/3
Receiving Slit	0.3
Voltage	40 kV
Current	44 mA
Start	10 °
Stop	90°
Sampling Width	0.05°
Scan Speed	2.5 deg/min

Table 5. Rigaku Ultima diffractometer parameters

The development of a TiO_2 process would ideally lead to improvements in the densification of the bottom Pt electrode and prevent inter-diffusion of the Ti and PbO, thus affecting PZT nucleation and growth [88]. The Ti/Pt process involved sputtering 20 nm of Ti and 85 nm of Pt deposited at 500°C using the CLC. Initial work used a thin TiO_2 buffer layer sputtered between the Ti and Pt layers and the effects of annealing the Ti/TiO_2/Pt stack at 500°C for 60 seconds in O_2 were studied. A Ti/Pt control sample was made and two Ti/TiO_2/Pt samples. One of the Ti/TiO_2/Pt samples was annealed in an RTA at 500°C in O_2 for 60 s and the other was not. XRD was performed on all three samples. The Ti/TiO_2/Pt sample that was annealed showed stronger (111) and (222) Pt peaks compared to the un-annealed sample and the Ti/Pt sample.

4.2.2 Influence of Ti/Pt and TiO_2/Pt on the Electrical Properties of PZT (52/48)

The three electrodes used in Figure 22 and an additional Ti/Pt sample that was annealed at 500°C in O_2 for 60 s were coated with a layer of 20 nm PTO and 500 nm of PZT (52/48). To examine the electrical properties with the new bottom electrodes, simple 500 x 500 µm square capacitors were fabricated and hysteresis measurements were performed on the capacitors using an HP Multi-Frequency LCR Meter 4275A at 10 kHz with an excitation signal of 50 mV and a Radiant Technologies RT-66a measurement unit.

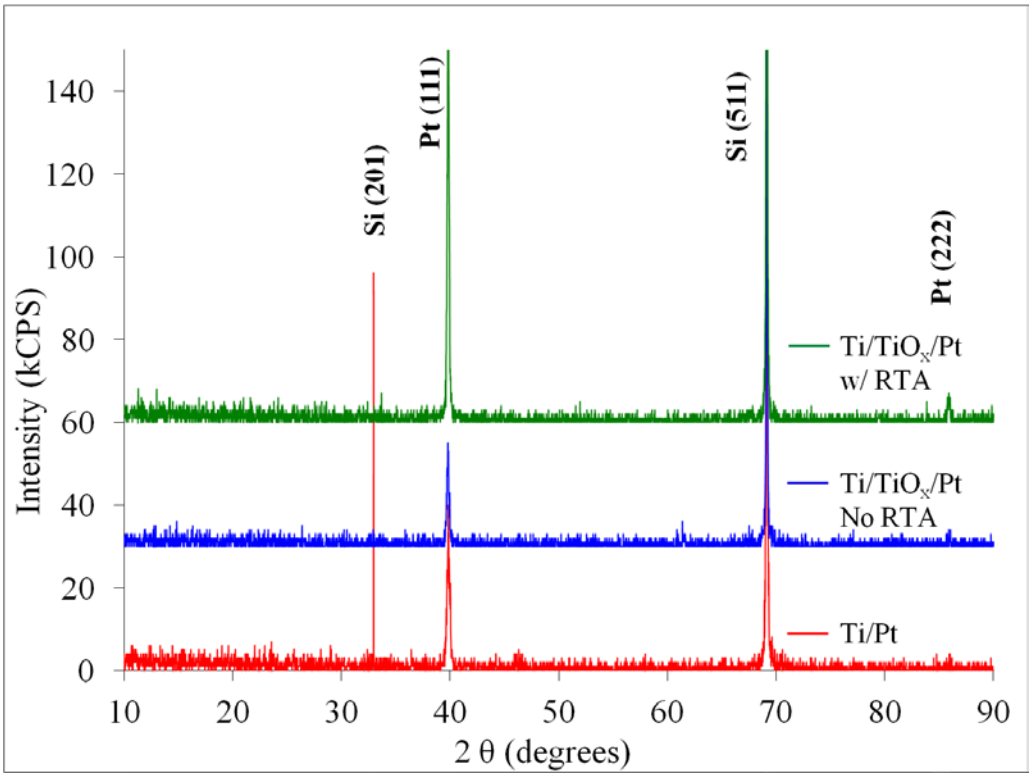

Figure 22. Influence of a TiO_2 barrier layer on Ti/Pt electrodes and the effects of an RTA

The Ti/Pt/PTO/PZT showed no difference in the electrical hysteresis loop of the PZT whether or not the Ti/Pt electrode was annealed at 500°C in O_2 for 60 s or not. The Ti/TiO_2/Pt/PTO/PZT samples showed the same improved dielectric constant

observed in Figure 17 however wider P-V loops were observed. Annealing the $Ti/TiO_2/Pt$ does lead to higher P_{max} and P_{sat} values, however, the overall influence on the electrical properties of the PTO/PZT did not lead to the improvements expected.

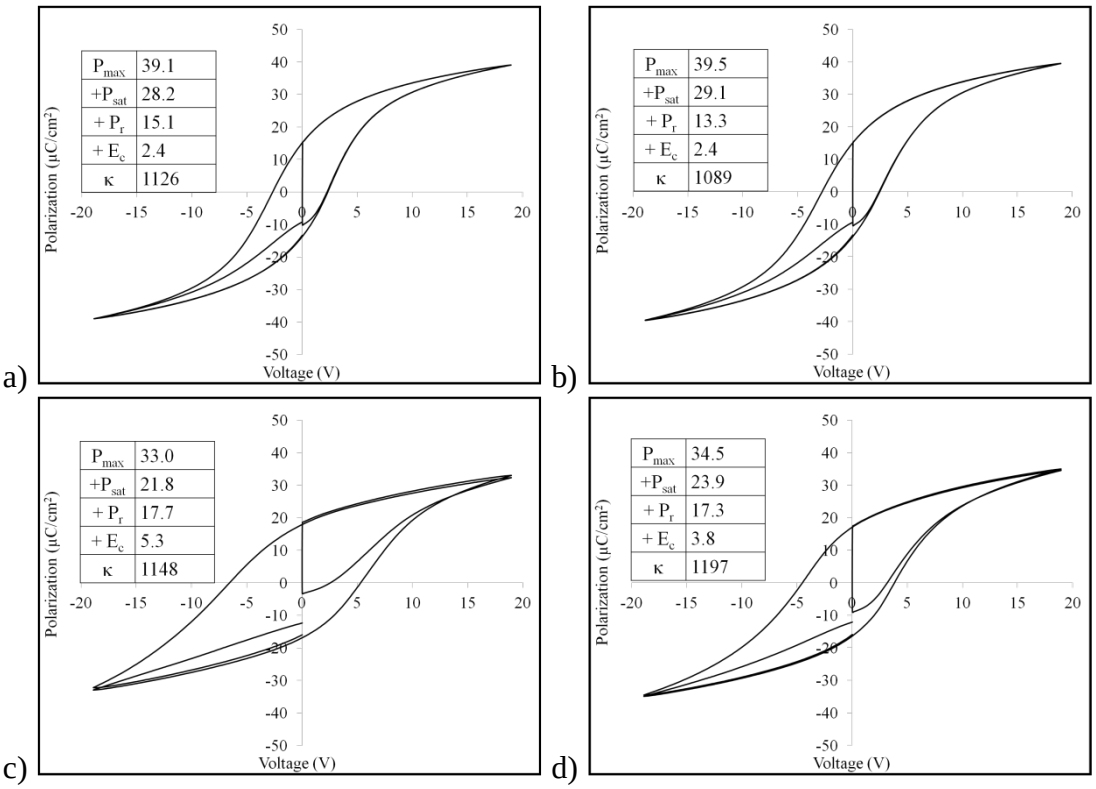

Figure 23. Hysteresis loops for a) Ti/Pt (no RTA)/PTO/PZT b) Ti/Pt (RTA)/PTO/PZT c) $Ti/TiO_2/Pt$ (no RTA)/PTO/PZT and d) $Ti/TiO_2/Pt$ (RTA)/PTO/PZT

A study performed examining improvements on the Ti/Pt bottom electrode by Dr. Daniel Potrepka at the Army Research Laboratory [81] involved sputter deposited 30 nm thin layer of titanium (Ti) at room temperature using the CLC deposition tool at 500 W with 30 sccm Argon flow. The initial sputtered Ti is oriented in the (0001) hexagonal orientation. After the Ti deposition, an oxygen anneal was performed at 750°C in a Bruce Technologies tube furnace in O_2 for 30 minutes, to convert the Ti to TiO_2. Upon annealing via tube furnace, oxygen is pumped into the interstitial sites of the Ti, forming a rutile TiO_2 structure (Figure 24). This rutile structure is

energetically favorable for the growth of highly (111) oriented 100nm Pt deposited at 500°C achieving a full width half maximum (FWHM) between 1.7°-2.3°.

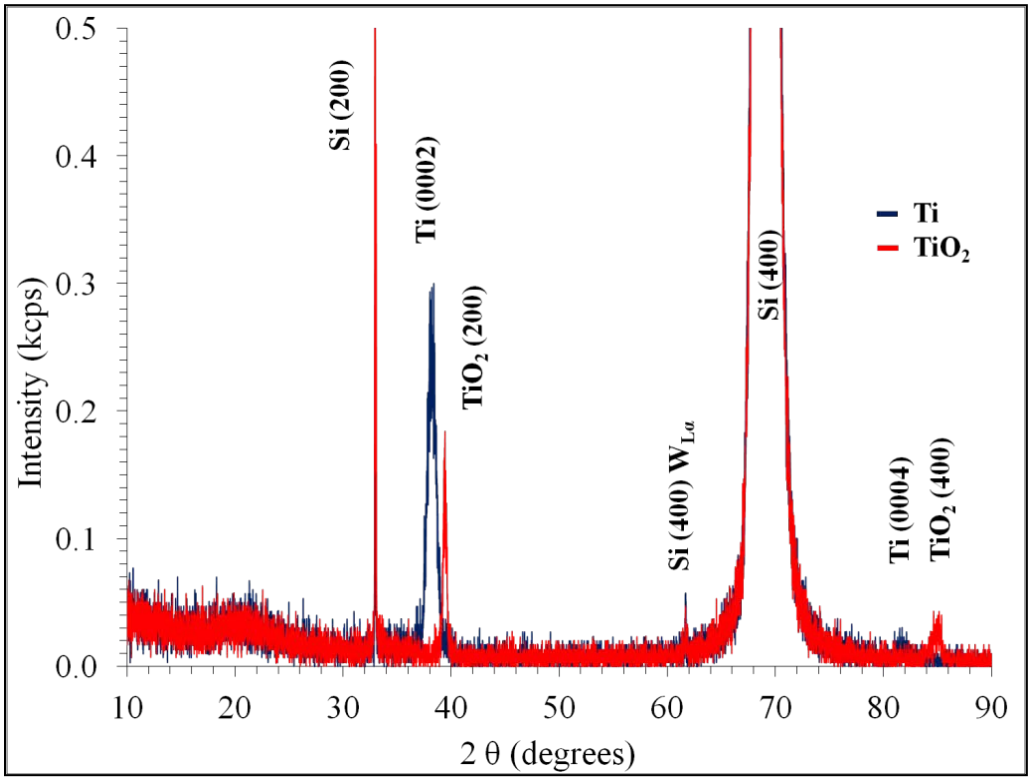

Figure 24. XRD comparison of Ti and furnace annealed TiO_2.

4.2.3 Influence of Ti/Pt and TiO_2/Pt on the Orientation of/PZT (52/48)

The effects of the TiO_2/Pt thin films on PZT orientation with and without a PTO seed layer were investigated. Two Ti/Pt samples were also coated with PZT and PTO/PZT as control samples. Using the Lotgering factor to better compare the crystalline nature of the different samples, improvements on the (001)/(100) PZT orientation were observed when using the TiO_2/Pt bottom electrode with a 20 nm PTO seed. The XRD measurements performed on the 4 samples showed random orientation on the Ti/Pt/PZT sample with a weak (001)/(100) Lotgering factor, $f_{(001)/(100)}$=0.59. The TiO_2/Pt/PZT XRD showed the influence of a highly oriented

bottom electrode on the PZT orientation. With an $f_{(001)/(100)}$=0.10, the main impact was noted in the (111) PZT orientation; with the highly (111) Pt resulting in (111) PZT templates. The use of PTO improved the (001)/(100) PZT orientation in both Ti/Pt and TiO_2/Pt bottom electrodes. The Ti/Pt electrodes showed improvements from $f_{(001)/(100)}$=0.59 to $f_{(001)/(100)}$=0.87 when using the PTO seed layer. The TiO_2/Pt electrode improved from $f_{(001)/(100)}$=0.10 to $f_{(001)/(100)}$=0.96, which was very reproducible (Figure 25).

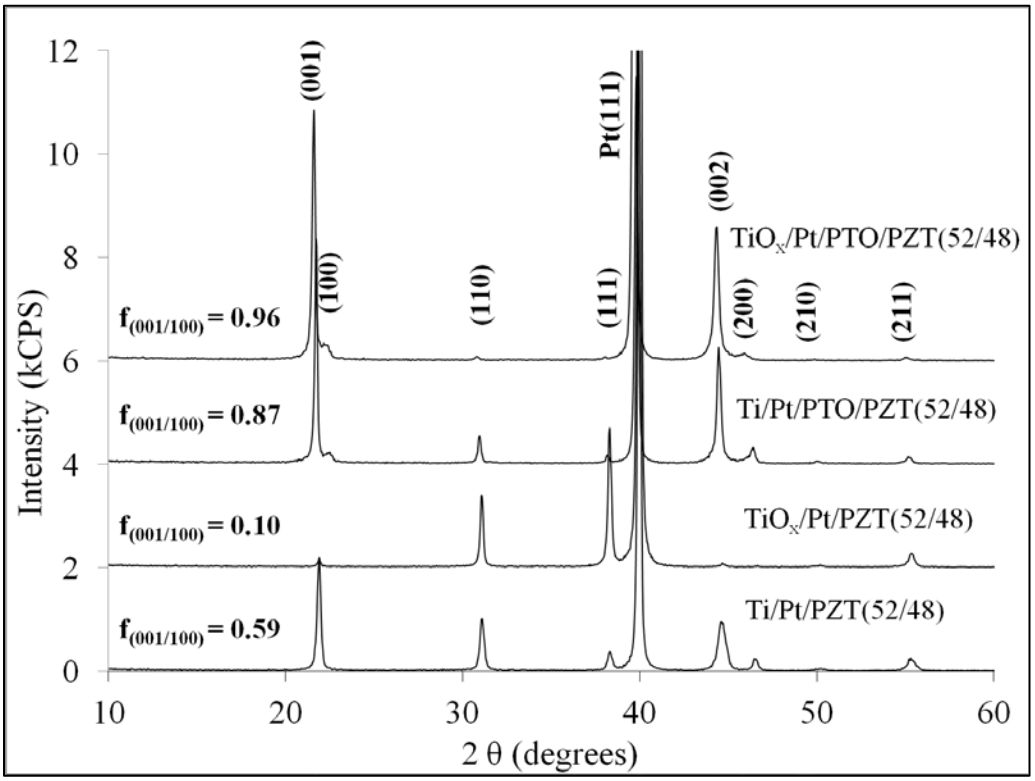

Figure 25. XRD illustrating the effects of the bottom electrode (Ti/Pt vs TiO_2/Pt) and the use of a PTO seed on the texture of PZT thin films.

Chapter 5: The Effects of Thermal Treatment and Lead Excess in $PbTiO_3$ and PZT (52/48) Solutions on Orientation

5.1 Effects of the Thermal Treatment of PZT (52/48) on Orientation

5.1.1 The Influence of the Crystallization Temperature on Orientation

As mentioned previously, the final annealing temperature, or crystallization temperature, of the PZT thin films will influence the orientation of the resulting material. A thorough study of crystallization temperatures between 560°C and 740°C, with a 20°C temperature difference between the samples, was performed. The data showed that annealing temperatures below 680°C exhibited a significant pyrochlore phase. The Pb-deficient pyrochlore phase reduces the piezoelectric properties of PZT thin films, when present, by pinning ferroelectric domains [89].

The best orientations in the films were observed at 700°C and 720°C even with a small unlabeled secondary phase around 30° that may be due to $Pb_2(Ti,Zr)O_3$, $PbZrO_3$, pyrochlore, or ZrO_2 precipitation (**Figure 26**). For these two temperatures of interest, 700°C shows a diminished (110) and a larger (111) PZT peak, whereas at 720°C the reverse is observed.

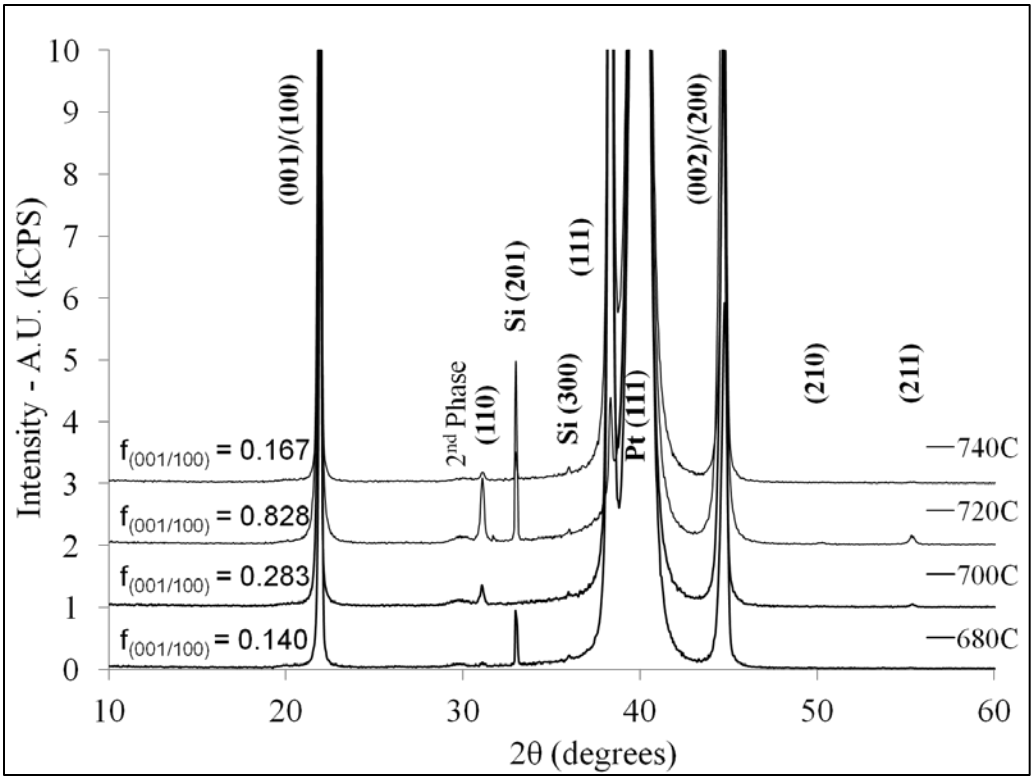

Figure 26. XRD of PZT films each crystallized at varying temperatures; 680 °C, 700 °C, 720°C, and 740 °C

5.1.2 Influence of Anneal Ramp Rate and Pb-Excess on Crystallization

With improved PZT(52/48) piezoelectric performance observed for the PTO in combination with the TiO_2/Pt electrode, it was expected that additional improvements could be obtained through optimization of the PZT thermal treatment, hence, a variety of RTA annealing parameters were studied. There are many reports available that perform slow RTA ramp rates such as 4°C/sec, slow ramp (SR) (Figure 13) and also fast ramp rates of over 100°C/sec or even furnace annealing of the PZT to acquire high orientation control [90][91][92]. Because such a wide range of anneal conditions have been reported to result in PZT with various crystallographic textures, three different anneal approaches were chosen for this study to determine whether a specific anneal method resulted in superior control of texture and properties. Since

the Pb content within the crystallized PZT film is dependent on the anneal profile the study of the effect of fast ramp rates included variations in Pb-excess contained within the PZT solutions used for film deposition.

It is important to note that the cleanliness of the RTA system is vital to maintain repeatable results in PZT orientation. A RTA system that hasn't been cleaned will lead to fluctuations in the Pb-excess due to a buildup of volatilized PbO within the quartz chamber. After cleaning the RTA it is necessary to condition the chamber by processing PZT coated wafers to prevent excessive PbO loss in the film. The RTA system in this study has been cleaned in a 30% acetic acid bath on average once a month to maintain repeatable operational conditions.

PZT films deposited from solutions with 8, 10, and 15% Pb-excess were analyzed under the following two RTA ramp processes referred to as "Rapid Ramp" (RR) (Figure 13b) and "Double Ramp" (DR) (Figure 13c). In the RR process, the sample temperatures were ramped up and down as fast as possible using an A.G. Associates Heatpulse 610 RTA. For these experiments, the temperature ramp (up and down) was ~199^{o}C/sec with a dwell at 700^{o}C for 60 seconds. Similarly, in the DR process, the temperature ramp (up and down) was ~199^{o}C/sec with a dwell 1 at 550^{o}C for 2 minutes followed by a ramp and dwell 2 at 700^{o}C for 30 seconds. It has been reported that the anneal at 550^{o}C allows the PZT to crystallize at low temperature under conditions that result in reduced PbO evaporation from the sample surface but still provides the textured crystallization [93]. The 700^{o}C segment of the two step anneal process is reported to encourage grain growth and the removal of other growth defects [82], [93]. In both RR and DR cases, the software control of the RTA was

terminated once the samples cooled to 350°C. XRD data was gathered to determine the best orientation in PZT films under the conditions described (Figure 27).

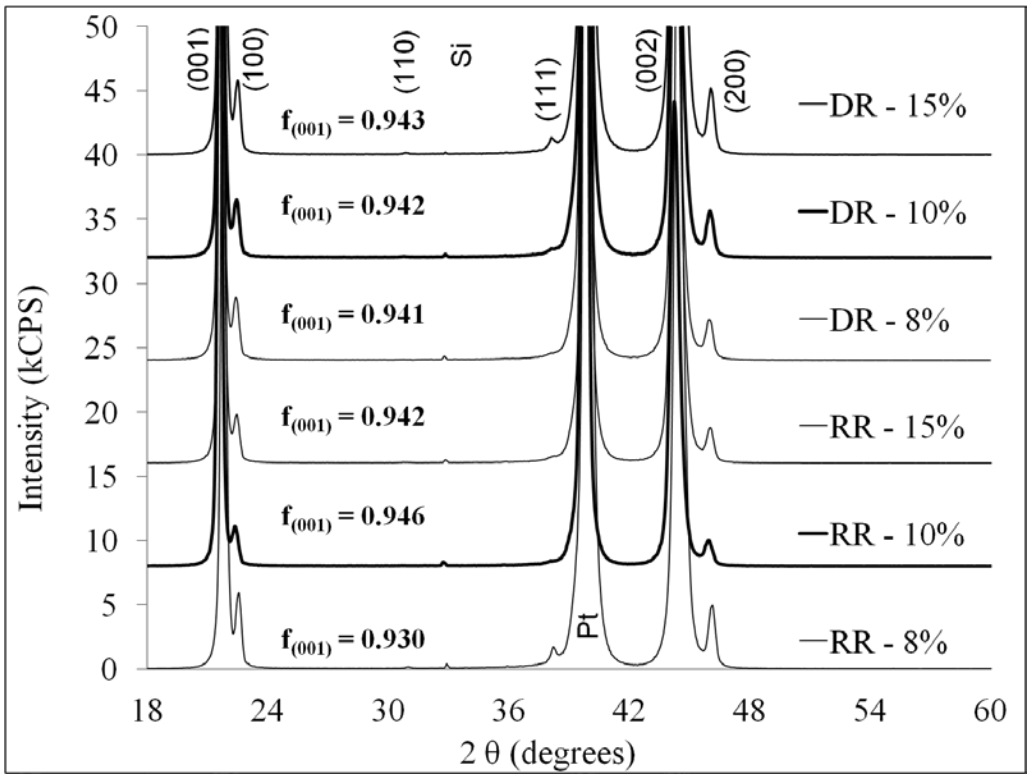

Figure 27. XRD Summary of the varying ramp rate and Pb-excess conditions.

By performing the RR and DR anneals on samples with the optimized bottom electrode and PTO seed layer, it was determined that the 10% Pb-excess using a RR DR showed the highest (001) orientation and the greatest reductions in both the (110) and (111) PZT peaks. Lotgering factors of the RR and DR were $f_{(001)}$=94.6% and $f_{(001)}$=94.2%, respectively (Figure 28). The $f_{(100)}$ for RR and DR for 10% Pb-excess PZT (52/48) showed values of 4.9% and 5.2% ,respectively (Figure 28). Comparing the Lotgering factor for unseeded PZT deposited on Ti/Pt prepared at the beginning of this research to the seeded PZT films deposited on TiO_2/Pt, which is the current

state of the art, shows a substantial increase in (001) and (001/100) orientations, from $f_{(001)}$=59% to $f_{(001)}$=96%, in the PZT thin films.

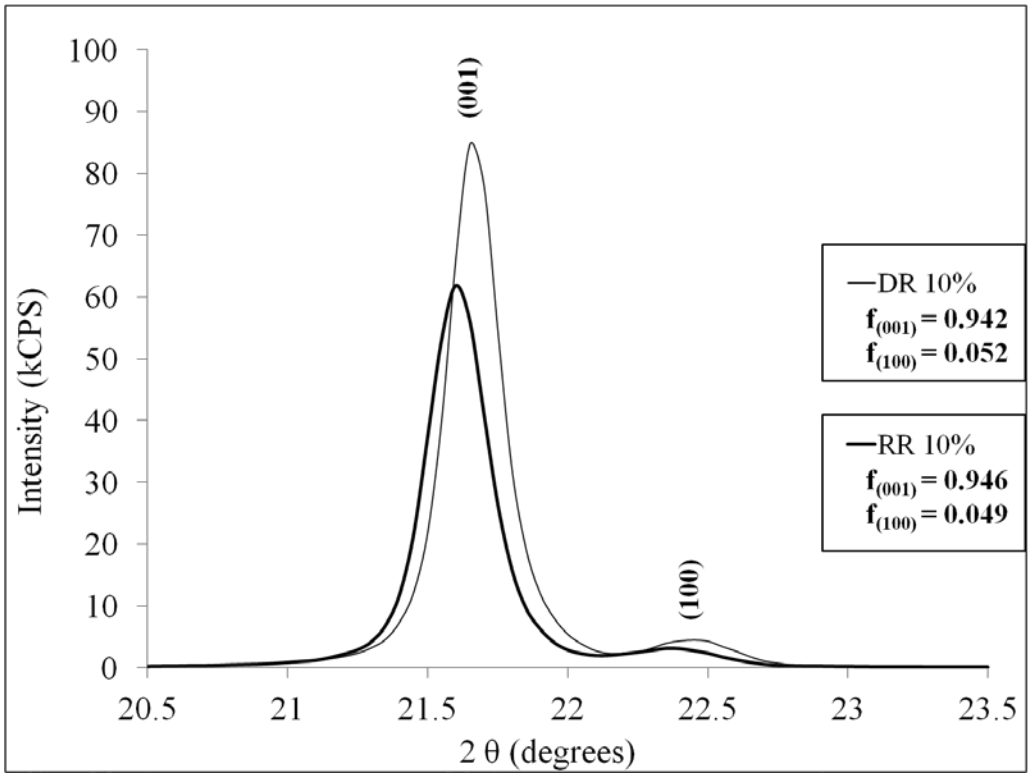

Figure 28. XRD comparison of DR and RR annealed samples with 10% Pb-excess along with their respective Lotgering factors.

A cross-section transmission electron microscopy (TEM) measurement was performed by Ke Wang and Leonid Bendersky at NIST on the PZT (52/48) annealed under the RR conditions using a JEOL JEM-3010 UHR at 300kV. Templating is observed from the bottom Pt electrode between the Pt-PTO and the PTO-PZT (Figure 29). It is evident that the TiO_2/Pt/PTO layers have a great influence on PZT (52/48) orientation, allowing for columnar growth associated with (001) film growth.

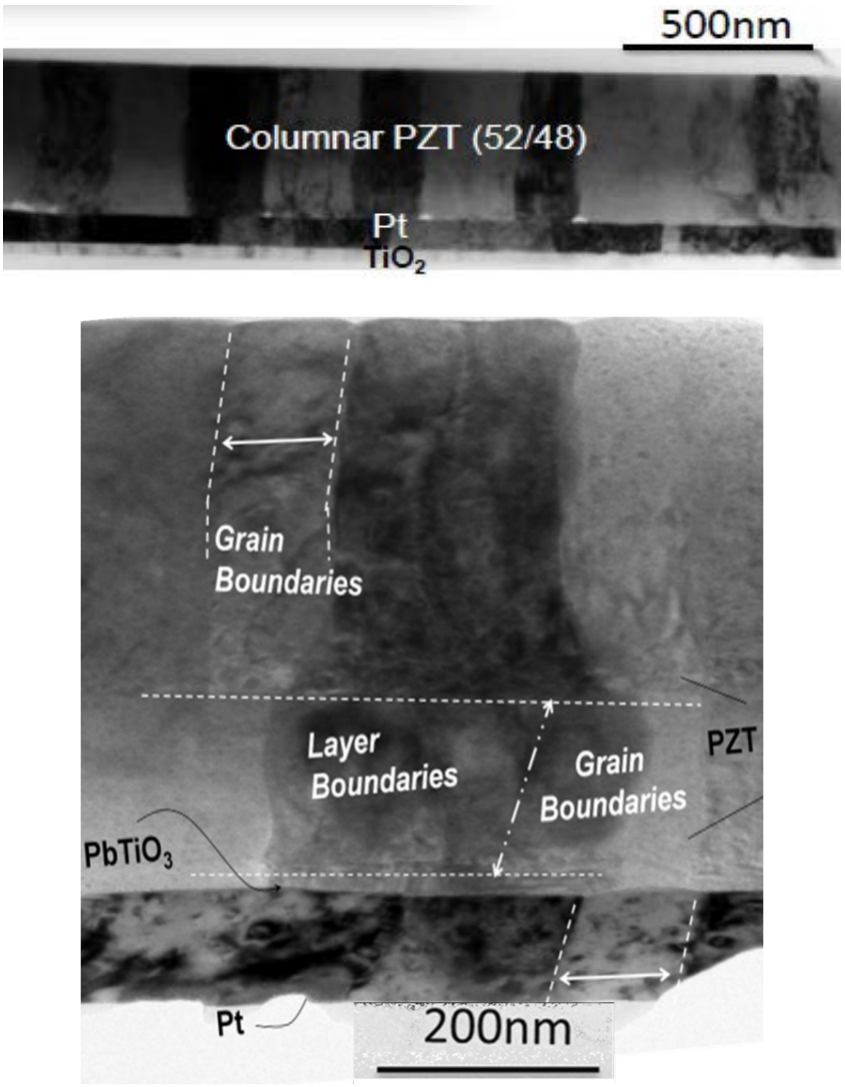

Figure 29. Cross-section TEM demonstrating columnar growth on a TiO_2/Pt/PTO/PZT samples annealed under RR conditions.

To further evaluate the texture of the PZT and the electrode and seed layer effects, electrical data was acquired on simple capacitors, fabricated as described previously, using wafers coated with PZT processed using the 10% Pb-excess DR and RR annealing conditions on the TiO_2/Pt bottom electrodes. From these 500x500µm square capacitors, the dielectric constants were calculated for samples processed under both annealing conditions. As shown in Table 8, the 10% Pb-excess under the

DR conditions showed a ~13% higher dielectric constant compared to the RR conditions. The values are average values taken on 6 different capacitors on 8 samples (4 samples under the DR conditions and 4 under the RR conditions) to demonstrate reproducibility.

Sample	+ Pr	-Pr	Thickness (µm)	Cap. (nF)	Tanδ (%)	ε	Std Dev.
PTO/ **10%** Pb-excess PZT (52/48) DR anneal	17.2	15.7	0.5	5.9	0.070	1343	22.4
PTO/ **10%** Pb-excess PZT (52/48) RR anneal	16.9	15.4	0.5	5.3	0.066	1190	3.5
PTO/ **8%** Pb-excess PZT (52/48) DR anneal	16.1	12.3	0.5	5.1	0.069	1012	9.1
PTO/ **8%** Pb-excess PZT (52/48) RR anneal	19.4	15.4	0.5	5.5	0.070	1088	35.6

Table 6. Dielectric constants in 5 samples of 10% and 8% Pb-excess under DR and RR conditions.

5.1.3 Cantilever Displacement Measurement on10% Pb-Excess PZT (52/48)

Initial cantilever displacement data shows promising results in the efforts to achieve high displacement with lower actuation voltage devices. Comparing 10% Pb-excess PZT (52/48) under DR and RR conditions with and without the PTO seed layer, one can clearly see tremendous improvements in cantilever deflection (Figure 30). Although the DR samples showed improved dielectric constant (Table 8), it was the RR with seed layer samples that showed the greatest deflection with 120% improvement over RR without the PTO seed layer at 2 volts. Changes in mask design do not allow a direct comparison with previously discussed cantilever displacement data in Figure 20. The new cantilever lengths measured in these experiments were 27µm long, and were deflected so far out-of-plane that taking optical profilometry

measurements were difficult as not enough light was reflected back from the cantilever for an accurate measurement.

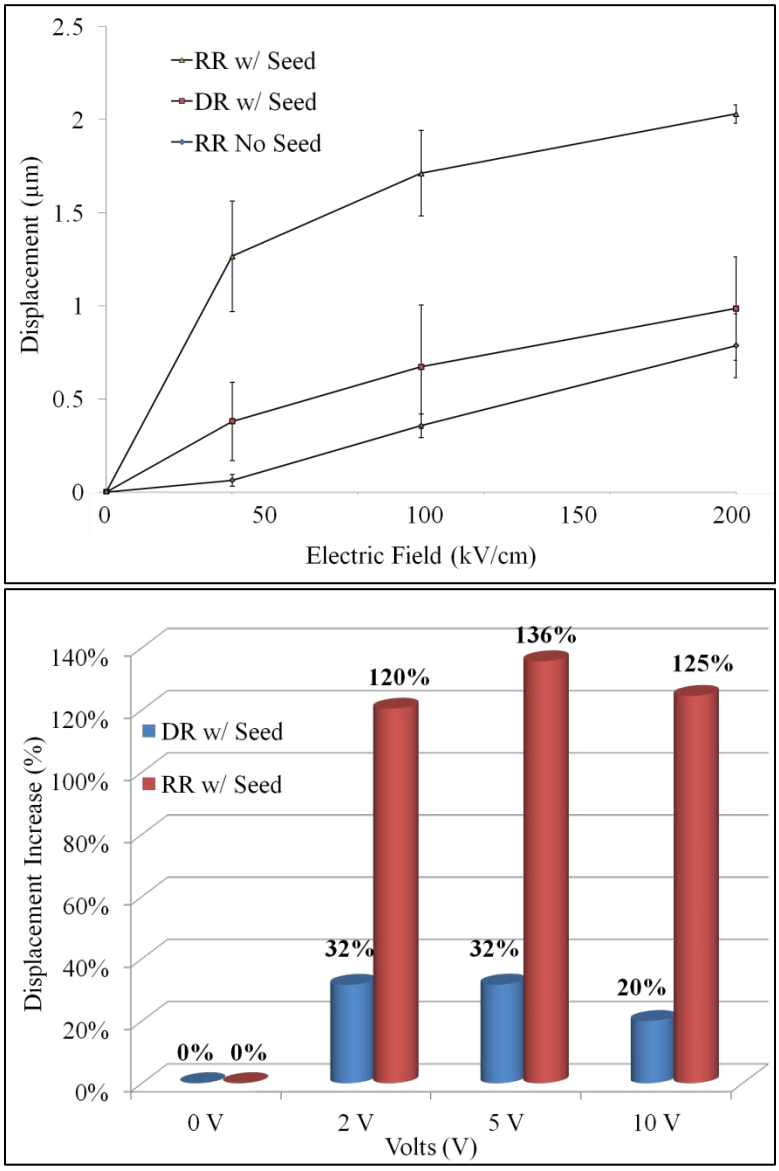

Figure 30. Comparison of the cantilever displacements in 10% Pb-excess PZT under DR or RR annealing conditions.

In a separate experiment, PZT (52/48) samples were fabricated, one with the PTO seed layer leading to highly (001) oriented PZT (52/48) films and the other without the PTO seed layer leading to highly (111) oriented films (Figure 31)

Cantilever arrays were once again fabricated and using a Polytec MSV laser Doppler vibrometer (LDV) system, the cantilever arrays were poled and unipolar actuation data was acquired. The LDV system allows for non-destructive, dynamic displacement measurements to be taken.

a) 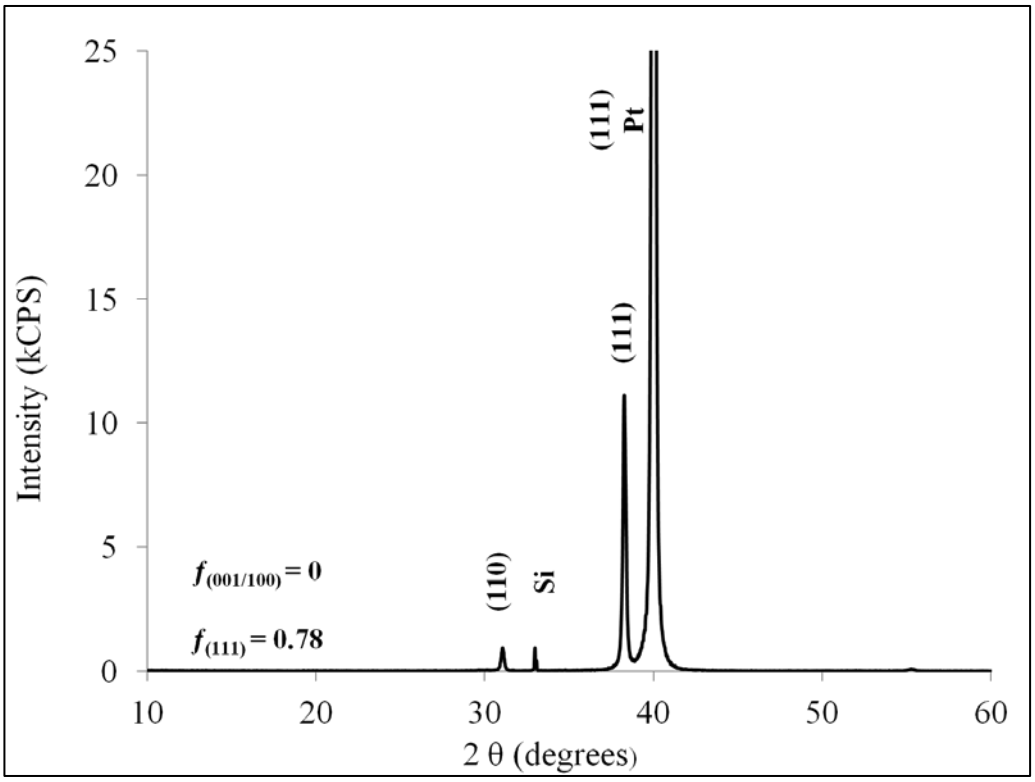

b)

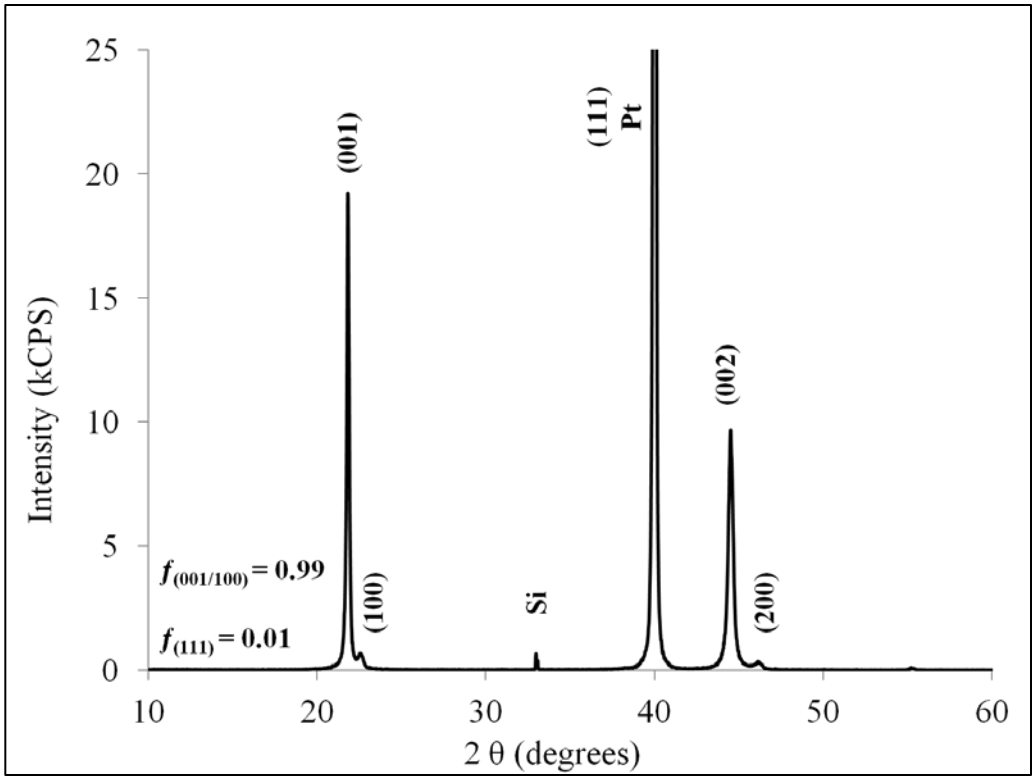

Figure 31. XRD of a) highly (111) oriented PZT and b) highly (001) oriented PZT.

Using the LDV at a frequency of 2 Hz to measure the piezoelectrically induced deformation in 52µm long cantilevers, devices made from the (001) oriented films shows significant improvements over devices from (111) oriented films. Comparing the two samples at 9.8V with the bottom Pt electrode serving as the ground connection, a 50% increase in deflection is observed with a peak displacement of 1.33 µm in the (001) oriented film and a 0.67µm displacement in the (111) oriented films (Figure 32a). Similarly, at 4.9V, the (001) samples exhibit approximately 46% improvement over the (111) films (Figure 32b).

Actuating the films using negative voltages show similar results (Figure 32c). A near doubling of the displacement is observed in films with (001) oriented PZT (52/48) compared to the (111) oriented films at -9.8V. At half the voltage, 4.9V, an

improvement of only 26% was observed for the (001) films. The impact of obtaining (001) oriented PZT (52/48) films is noted here for applications requiring a large displacement and/or requiring a lowered voltage for operation.

a)

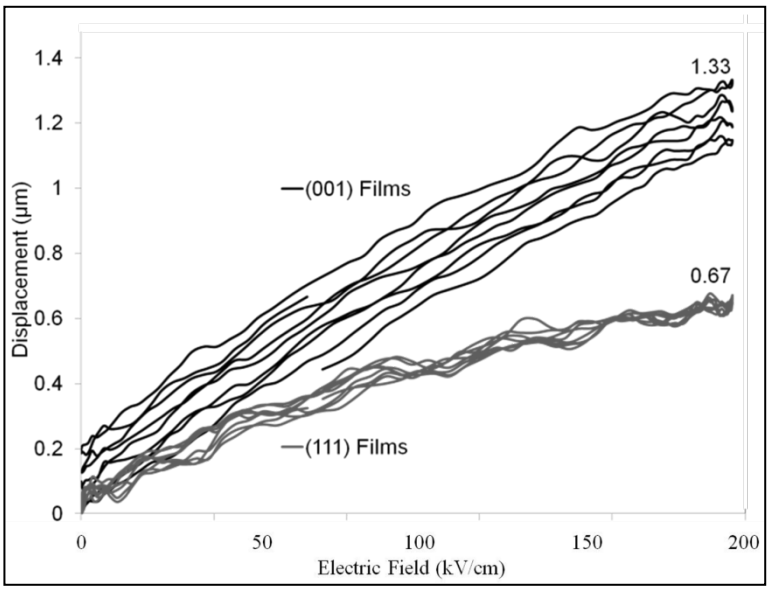

b)

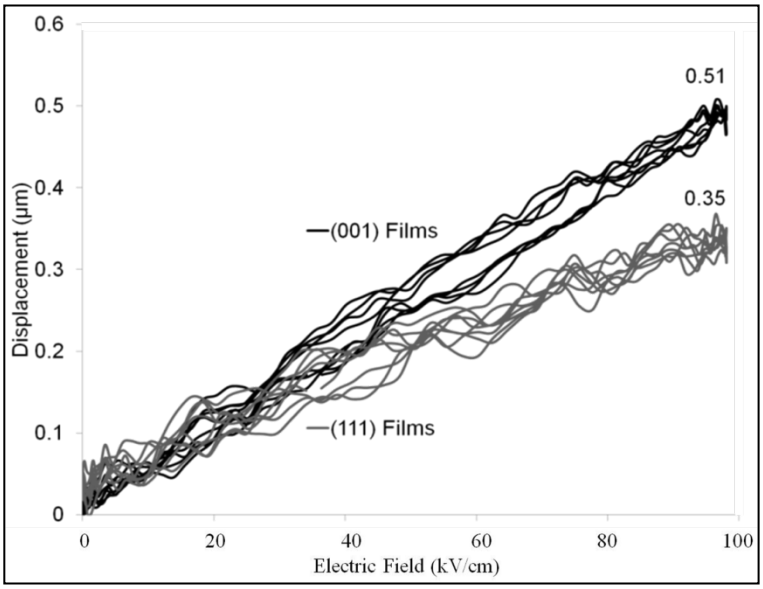

c) 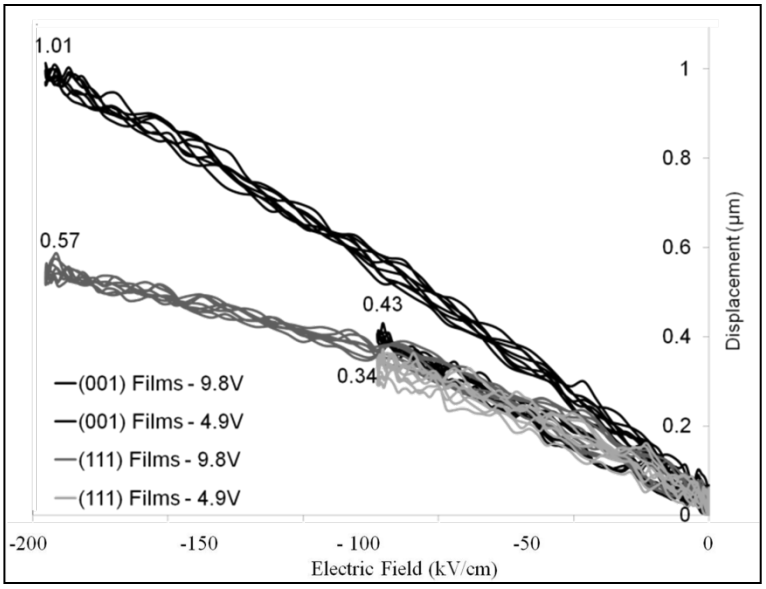

Figure 32. LDV data showing the effects of orientation on 52 µm cantilever displacement in devices actuated up to a) + 200 kV/cm b) + 100 kV/cm and c) – 200 kV/cm. Note – the noise in the individual traces was attributed to a combination of extreme positive curvature in the cantilevers which limited imaging to the smallest cantilevers in the array. This was corrected in subsequent tests (see section 5.2)

5.1.4 Effects of Pyrolysis Temperature on 10% Pb-Excess PZT (52/48)

The sol-gel process for PZT films includes a pyrolysis step where organic materials are removed from the films at temperatures below the films crystallization temperature. The exisiting process involved using a hotplate at 350°C for 1 minute. Using the RR annealing process, 4 pyrolysis temperatures were studied to see the effect, if any, on film orientation. The temperatures used in this study were 350°C, 400°C, 430°C, and 450°C. An attempt at a 500°C pyrolysis was made however hotplate temperature control above 450°C proved to be difficult with 15°C temperature fluctuations. Films were deposited at the specified pyrolysis temperatures and annealed using RR conditions at 700°C. Finally, XRD measurements were performed to observe film orientation.

Pyrolysis temperature definitely affects film orientation, with and without the use of the PTO seed layer. In samples without the PTO seed layer (Figure 33a), (100) peak intensity increases with increasing temperature. However, the random order peaks (110) and (111) also increase showing a slight decrease at the 450°C pyrolysis temperature. The greatest effects are shown in the samples with the PTO seed layer (Figure 33b) at a temperature of 400°C, in which there is no (110) and a small (111) peak relative to the high (001) orientation. At 430°C, (111) peak dominates the film orientation but decreases again at 450°C as observed in the Lotering factors in Table 7.

a)

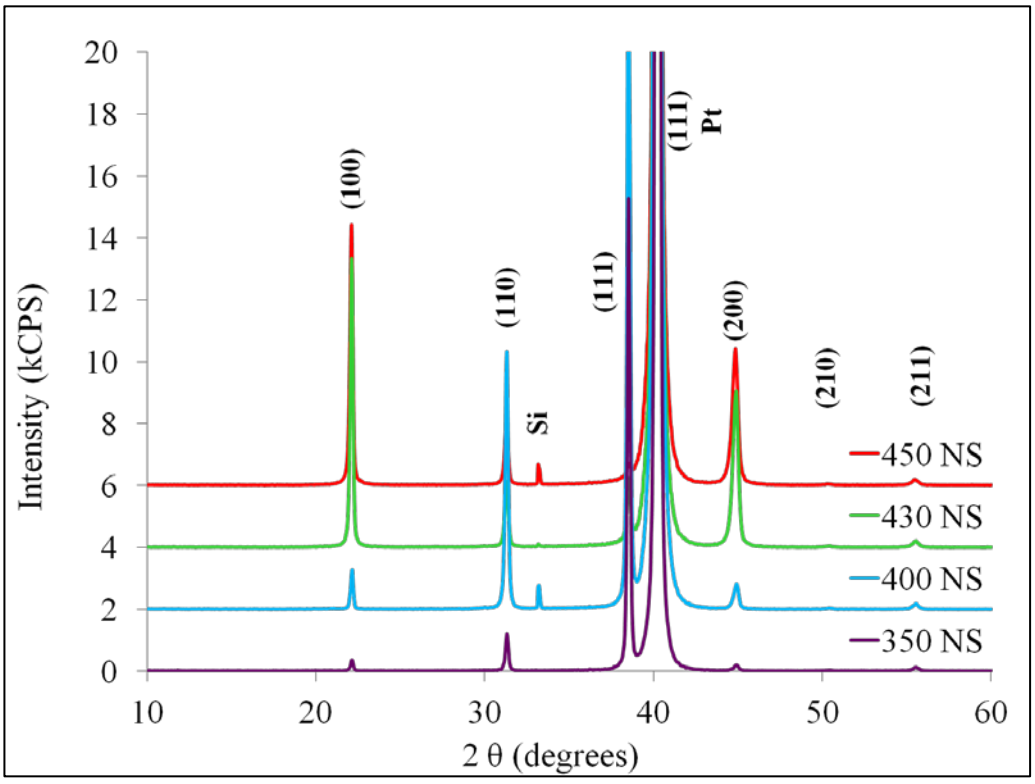

b)

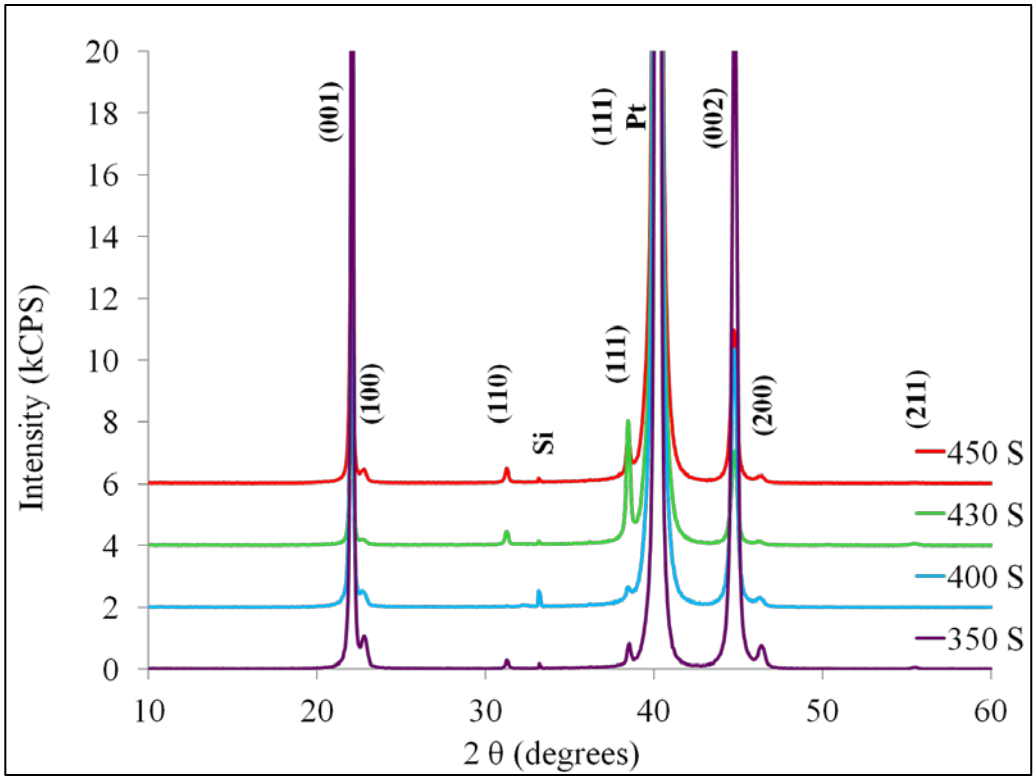

Figure 33. XRD of samples under varying pyrolysis temperatures under RR annealing conditions a) without PTO and b) with PTO

$f_{(001/100)}$		350°C	400°C	430°C	450°C
	PZT	13.5%	9.8%	71.3%	77.1%
	PTO/PZT	97.6%	96.4%	61.0%	57.4%

Table 7. Lotgering factor calculations for samples pyrolyzed with and without the PTO seed layer.

5.2 Influence of Pb-Excess on Device Properties

A described previously, the effects of PbO evaporation during the thermal treatment of PZT greatly influence the nucleation of PZT on the Pt electrodes. The initial investigation looked at comparing 8%, 10%, and 15% Pb-excess in the PZT while the PTO was kept constant with a Pb-excess of 30%. Devices fabricated with 30% Pb-excess PTO and 15% Pb-excess PZT demonstrated catastrophic failure upon

the application of any voltage. With this knowledge, a new study was proposed to examine a matrix consisting of varying the Pb excess in the PTO and the Pb excess in the PZT solution. The investigation required the creation of 19 individual combinations as shown by the X's in Table 8.

PbTiO3 Pb%	PZT Pb-Excess %				
	0%	3%	5%	8%	10%
0%	X	X	X	X	X
10%	-	X	X	X	-
15%	-	X	X	X	-
20%	-	X	X	X	-
30%	X	X	X	X	X

Table 8. Wafers fabricated with varying Pb-excess in both the PTO and PZT solutions are shown in the matrix and designated by an X.

Similar to the previous experiment, the solutions were fabricated using Equation 1 from Chapter 3 to determine the amount of Pb-excess required. The films were deposited on 150mm Si wafers with 500nm thermal oxide elastic layer and TiO_2/Pt bottom electrode. The wafers were coated with ~17nm or 1 layer of the PTO solution of the required Pb-excess using CSD. The wafer was pyrolyzed at 350°C for 2 minutes and then annealed in the RTA using the RR annealing procedure at 700°C for 1 minute. The wafers were then coated with PZT (52/48) of the appropriate Pb-excess to match the matrix in Table 8 until a thickness of approximately 0.5 µm was achieved (Table 9).

Wafer #	PTO Pb-excess	PZT Pb-excess	Notation PTO/PZT	Thickness (Å)
6117	0	0	0/0	4777
6109	0	3	0/3	5038
6101	0	5	0/5	5238
6163	0	8	0/8	4788
6103	0	10	0/10	4836
6006	10	3	10/3	5000
6015	10	5	10/5	5334
6151	10	8	10/8	4790
6102	15	3	15/3	5073
6120	15	5	15/5	6345
6110	15	8	15/8	4783
6017	20	3	20/3	4987
6155	20	5	20/5	5000
6001	20	8	20/8	4798
6107	30	0	30/0	5000
6113	30	3	30/3	5073
6019	30	5	30/5	5039
6020	30	8	30/8	4829
6122	30	10	30/10	5070

Table 9. Fabricated samples and final film thicknesses.

5.2.1 Description of Nomenclature

The data presented in this section has been sorted between the percentage of Pb-excess in the PTO seed layer and the percentage of Pb-excess in the PZT (52/48) as it is easier to observe trends. To facilitate the description of samples, they will be referred to by a ratio of the percentage of Pb-excess in the PTO solution to the percentage of Pb-excess in the PZT solution, i.e. 30/10 refers to 30% Pb-excess in the PTO solution and 10% Pb-excess in the PZT (52/48) solution. Another method used to describe the samples in this thesis will also be 30 PTO 10 PZT to describe 30% Pb-excess in the PTO solution and 10% Pb-excess in the PZT (52/48) solution.

5.2.2 Calculating Grain Size by Interception Method

The surface morphology of the PZT films with varying Pb-excess were observed, as-deposited, using a Zeiss scanning electron microscopy (SEM) with an accelerating voltage of 2.29kV, an aperture size of 30 µm , and frame averaging of n=2 due to the charging nature of the PZT. The grains were visible at a magnification of 20kX, allowing for relatively easy measurements of the grain sizes. Using the Zeiss SEM software, the images were annotated with seven randomly placed lines of 2µm length, scaled to the magnification of the image taken (Figure 34).

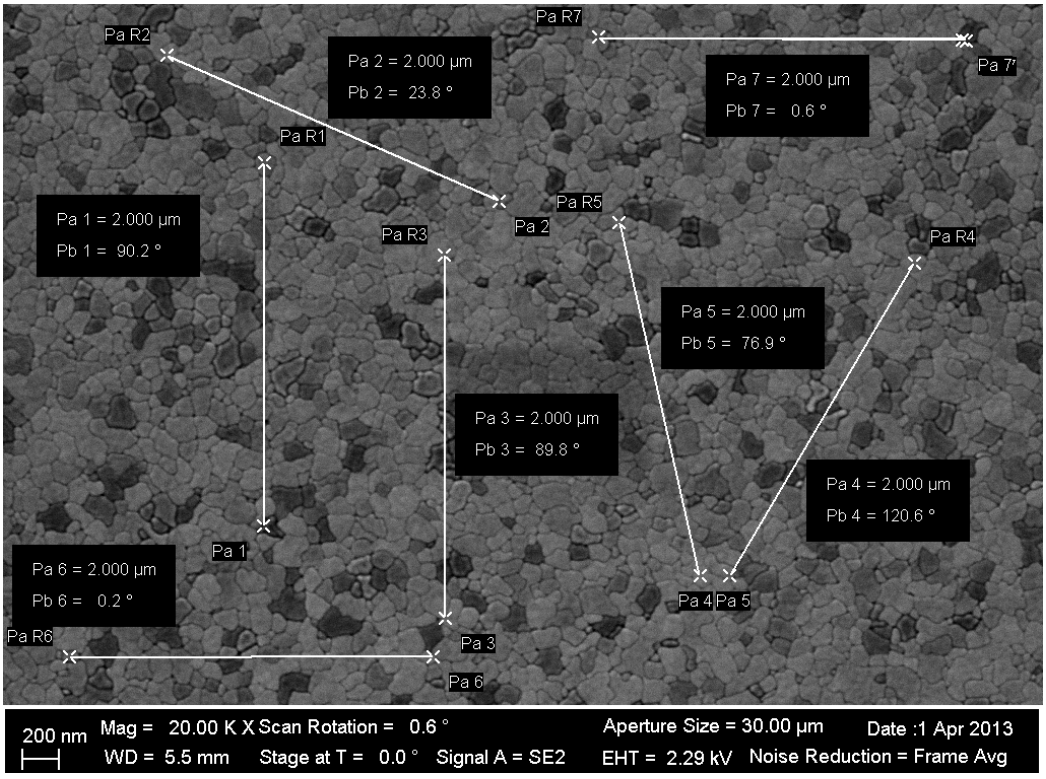

Figure 34. SEM image of 10 PTO 5 PZT annotated with 7 randomly placed lines of 2 µm length of grain size measurements.

In the intercept method, each grain boundary that crosses the 2 µm line is counted. To prevent counting error or bias when one line has a higher value than another line, imaging software, in this case ImageJ, was used (Figure 35). This process was performed for each of the seven lines and the average is taken. The line length of 2 µm (or 2000 nm) was divided by the average number of interceptions per line to give the average grain size value. Since the 2 µm annotated lines were drawn to scale with the image magnification, no correction factor was necessary. The raw count values for each line were saved and the grain size calculations were performed in excel.

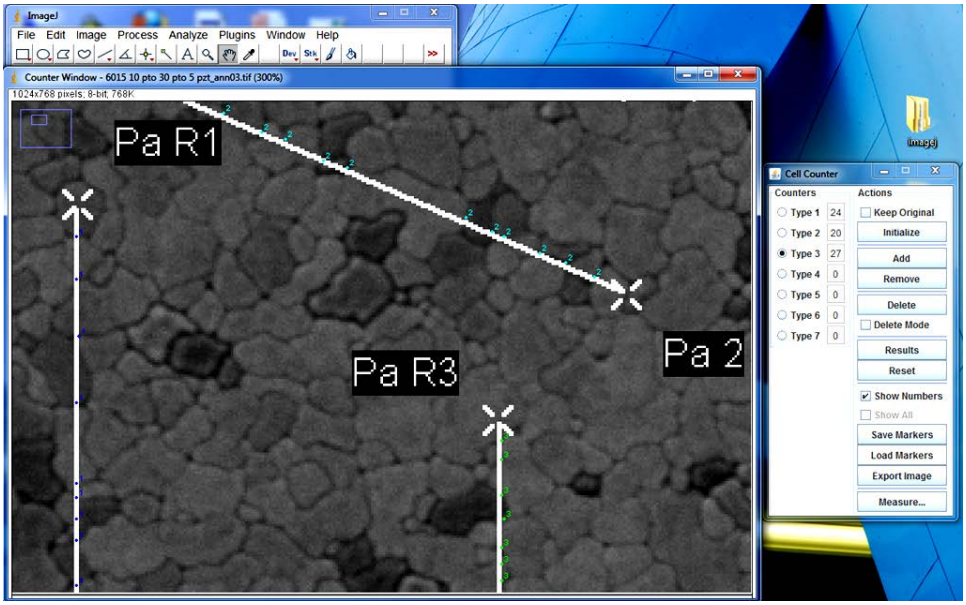

Figure 35. Screen shot of ImageJ software being used to count line interceptions in SEM image 10 PTO 5 PZT

There were five films that were not imaged prior to fabrication; however, some trends were present on the influence of Pb-excess to the grain size of PZT in the samples that were imaged. When the data is sorted as a function of Pb-excess in the PTO (Figure 36) no noticeable trends are observed. Plotting the data as a function of Pb-excess in the PZT showed larger grain sizes, greater than 110nm, in PZT films

with 8% Pb-excess in the PZT solution compared to the rest of the samples that had grain sizes of less than 110 nm (Figure 37). The sample 0 PTO 5 PZT also showed grain sizes larger than 110nm with a small standard deviation.

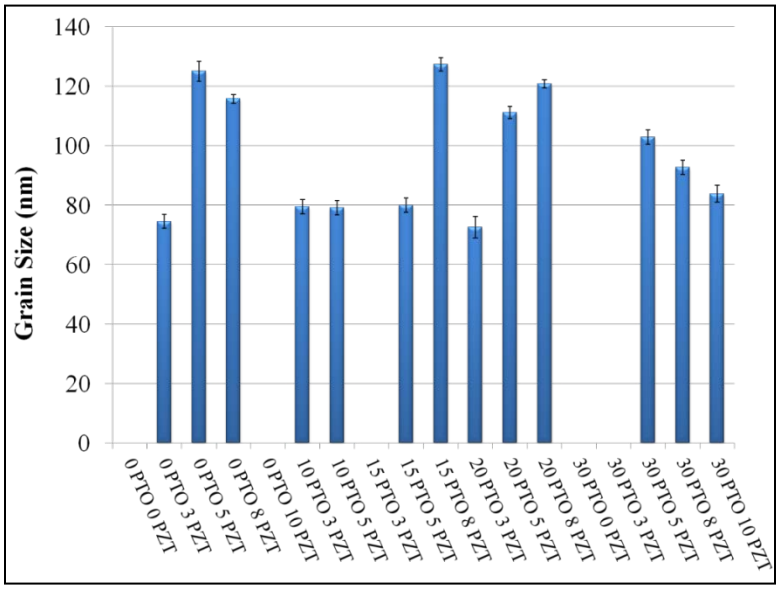

Figure 36. Effects of Pb-excess on the grain size of PZT. The data is sorted as a function of increasing Pb-excess in the PTO

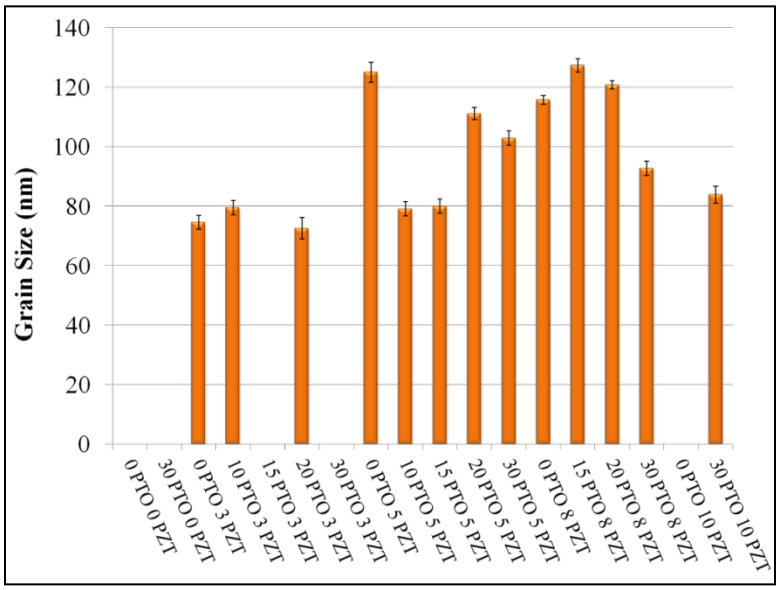

Figure 37. Effects of Pb-excess on the grain size of PZT a) data sorted as a function of Pb-excess in PTO b) data sorted as a function of increasing Pb-excess in the PZT.

5.2.3 XRD Results of Differences in Orientation

After the grain sizes of the samples were characterized, a 50 nm top Pt electrode was deposited using the CLC at 500ºC. The samples were removed from the cleanroom to perform x-ray diffraction using a Rigaku Ultima III Diffractometer with Bragg-Brentano Optics. Scans between 10º-90º were performed with a step width of 0.02 and a scan speed of 5 degrees per minute. The XRD results show strong (001) orientation in samples with 30% Pb-excess in the PTO (Figure 38). All the other samples exhibited less than 50% (001) orientation with 0 PTO 3 PZT being an exception with a (001) film orientation of 72%. The general trend showed that samples with higher Pb-excess in the PTO seed layer exhibited the highest degrees of (001) orientation. Plotting the XRD data as a function of Pb-excess in the PZT that same trend is observed (Figure 39). Within groups of the sample Pb-excess in the PZT, as the percentage of Pb-excess increases in the PTO seed layer, the percentage of (001) orientation in the film also increases. One exception was sample group of 3% Pb-excess in the PZT that did not follow this trend with the 0/3 sample having a higher texture than the 15/3 sample. The Lotgering factors of the films in the (110) and (111) directions are shown in Figure 40. In all cases, PZT films with Pb-excess less than 30% in the PTO seed layer show higher percentages of (110) and (111) orientations.

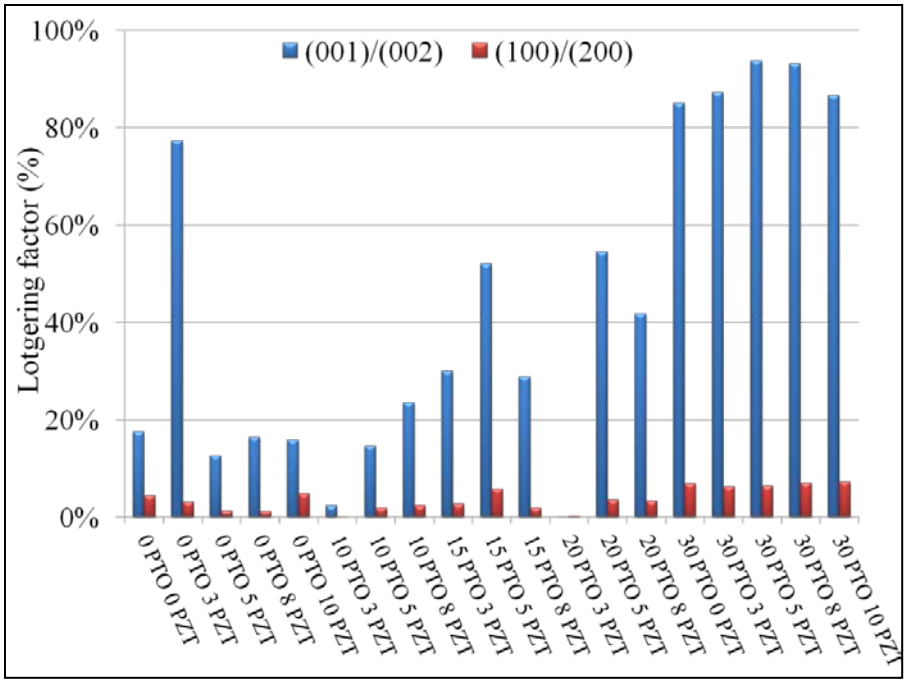

Figure 38. (001) and (100) Lotgering factor calculations for each sample represented in a bar graph, arranged as a function of increasing Pb-excess in the PTO.

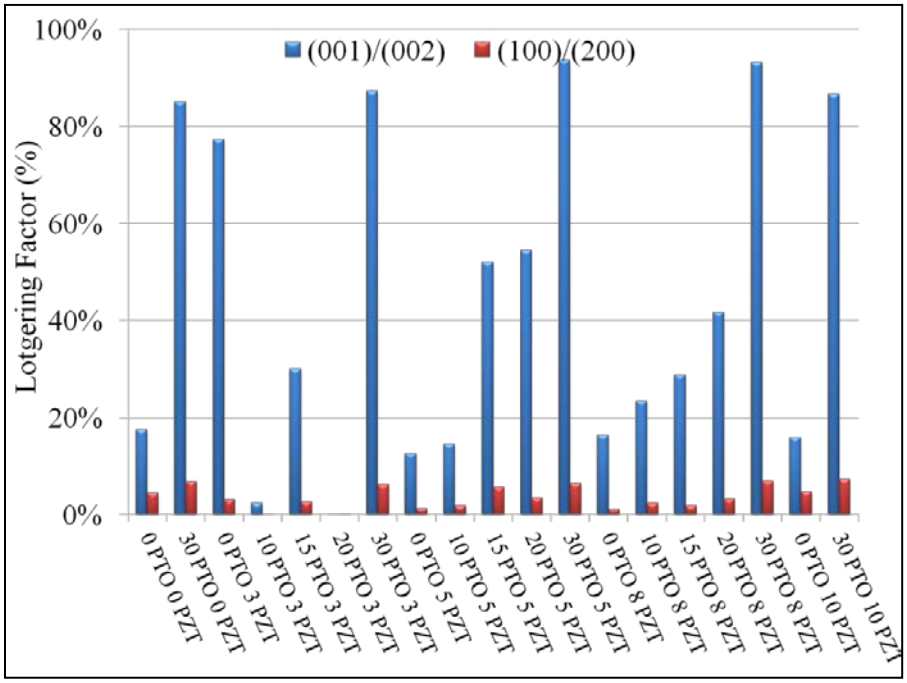

Figure 39. (001) and (100) Lotgering factor calculations for each sample represented in a bar graph, arranged as a function of increasing Pb-excess in the PZT.

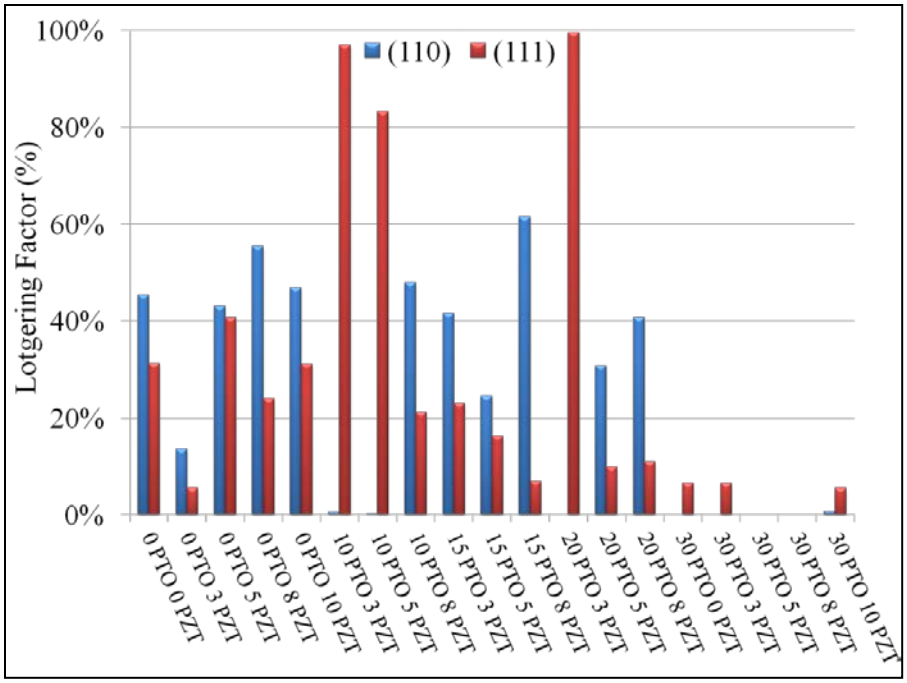

Figure 40. Lotgering factor calculations for (110) and (111) orientations in the samples, represented as a function of increasing Pb-excess in the PTO.

Several research groups have noted the influence of a TiO_2 layer on PZT orientation. The TiO_2 can be provided accidentally from a Ti adhesion layer under the platinum electrode. The Ti atoms will diffuse onto the surface of the Pt and oxidize, providing a necessary seed layer for (111) PZT growth [73]. Research performed by Willems et.al.[76] determined that a thin amount of TiO_2 on the Pt surface promotes {100} orientation in PZT as it lowers the nucleation energy of (100) oriented nuclei. However, too much TiO_2 leads to the opposite effect where the TiO_2 does not get consumed by the PZT and (111) oriented growth occur. In summary, the experiments performed in this thesis revealed the Pb-excess in the PTO seed layer solution greatly influences the final PZT film orientation more so than the additional TiO_2 that is provided from the $PbTiO_3$ seed layers. This implies that orientation is not necessarily controlled by TiO_2 on the surface of the Pt electrode which would be contributed

from the PTO seed layer, but that the amount of Pb in the initial PTO seed layer plays a major role in (100) film nucleation on the TiO_2/Pt bottom electrode.

5.2.4 Diced Samples

The electrical measurements performed on the wafers for the Pb-excess study were performed post fabrication. The wafers used in this study were diced and standard testing cells, 7.5 mm x 7.5 mm, were used (Figure 41). The testing cells were annealed in the RTA at 350°C for 2 minutes in O_2 three times to recover the PZT from fabrication induced damage; Pb and O vacancies and hydrogen implantation [94]. All measurements electrical measurements were performed on 2 capacitors on 3-5 different die for a total number of 6-10 samples per measurement for statistical purposes.

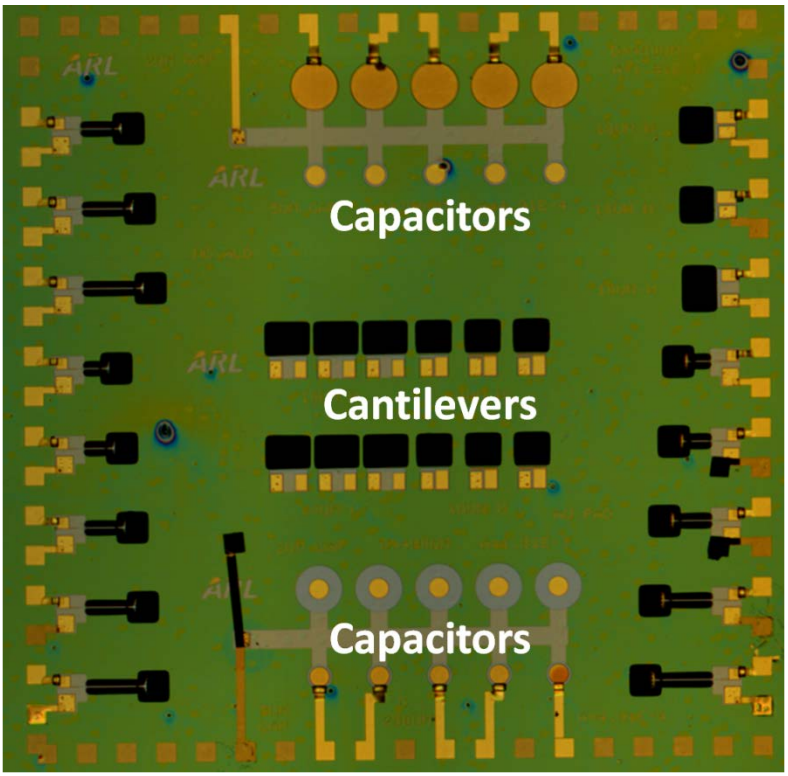

Figure 41. Test cell die used for this experiment with includes 20 individual capacitors and 15 cantilever arrays.

5.2.5 Hysteresis Measurements Performed in the Pb-Excess Study

The films processed in the Pb-excess study exhibited different degrees of tilting, shifting, and pinching in the hysteresis loops. The measurements were performed between -19V and +19V at a frequency of 50 Hz. The predominant features in most of the films are tilting and pinching of the loops. Tilting was observed in samples 0/3, 0/5, 10/5, 30/0, and 30/3 with little to no shifting or pinching in the loops. Shifted (imprinted) loops were observed in 0/0, 0/10, 30/10, and 15/5 with little to no pinching observed. The tilted and shifted hysteresis loops demonstrated higher maximum polarization values than with pinched hysteresis loops, with the exception of sample 15/5 whose tilt was large enough to show a reduced maximum polarization. Other samples exhibited pinched hysteresis that made

the loops appear to be imprinted; samples 0/8, 15/3, 15/8, 20/3, and 20/8. Overall when observing the hysteresis shapes in a matrix form as shown in Figure 42 the loops at the four extremes of the matrix show higher maximum polarization and less tilting than the loops located at the center of the matrix. The hysteresis loops also appear to become narrower, exhibiting a smaller area within the hysteresis, in the lower left quadrant, higher Pb-excess in both the PTO and PZT solutions, than in the upper right quadrant of the matrix, lower Pb-excess in both the PTO and PZT solutions.

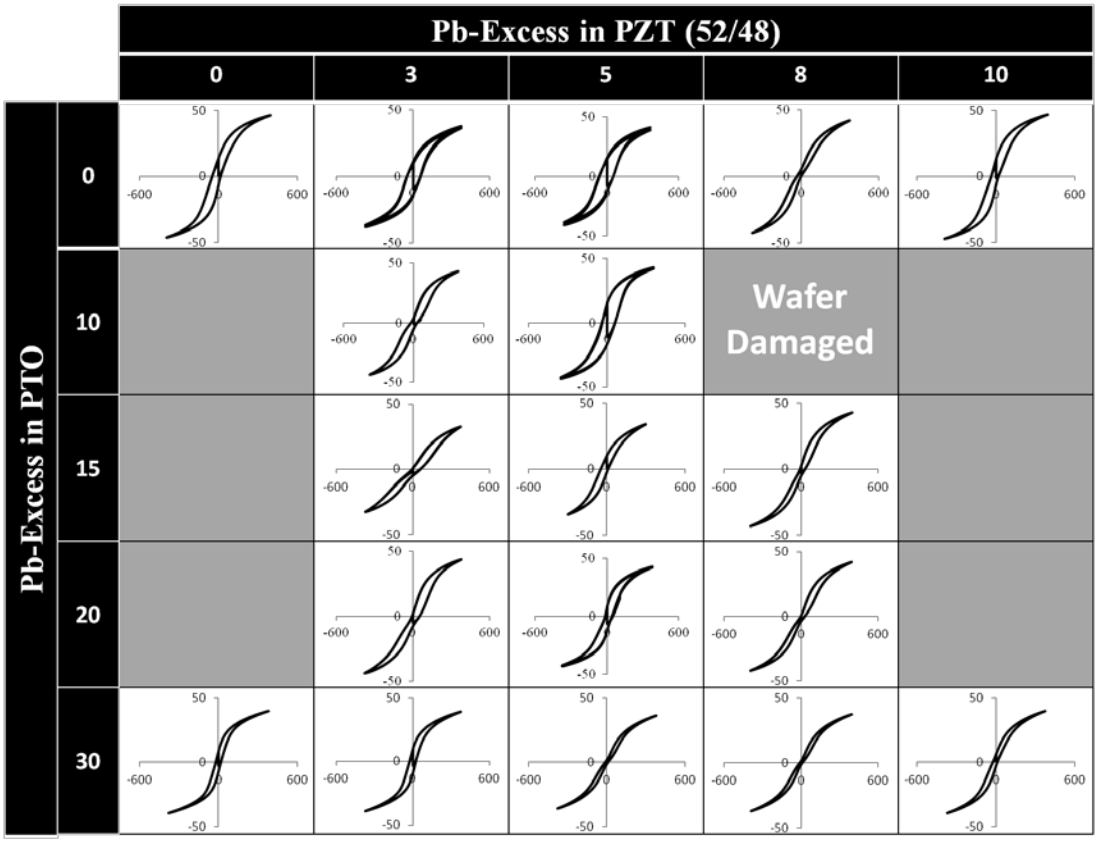

Figure 42. Hysteresis loops of films from the Pb excess study with Pb-excess percentage in the PZT on the top of the table and percentage of Pb excess in the PTO along the vertical axis. The charts are all plotted with the y-axis polarization (uC/cm2) values between -50 uC/cm^2 to 50 uC/cm^2 and the x-axis electric field (kV/cm) values between -600 kV/cm to 600 kV/cm.

The values for the maximum polarization, P_{max}, saturation polarization, P_{sat}, and remanent polarization, P_r, were plotted together first as a function of increasing Pb-excess in the PTO seed layer solution (Figure 43) and then as the Pb-excess in the PZT solution (Figure 44). Figure 43 shows that samples with a lower percentage of Pb-excess in the PTO seed layer exhibited higher P_{max}, P_{sat}, and P_r values and a decreasing value trend in samples with higher percentages of Pb-excess in the seed layer. When the data is arranged as a function of increasing Pb-excess in the PZT solution, (Figure 44), there are no trends present within the individual groups of Pb-excess in the PZT and no net change across all the samples in the P_{max} and P_{sat} values. The P_r values show a decreasing trend from samples with lower Pb-excess in the PZT solutions to samples with higher Pb-excess in the PZT solution.

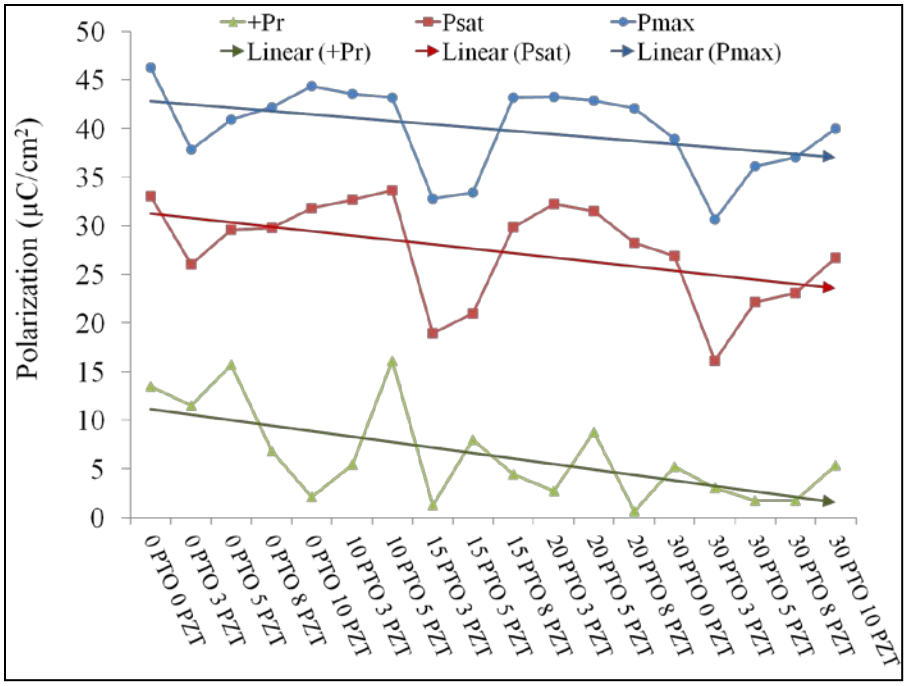

Figure 43. Hysteresis loop data plotted as a function of increasing Pb-excess in the PTO seed layer solution.

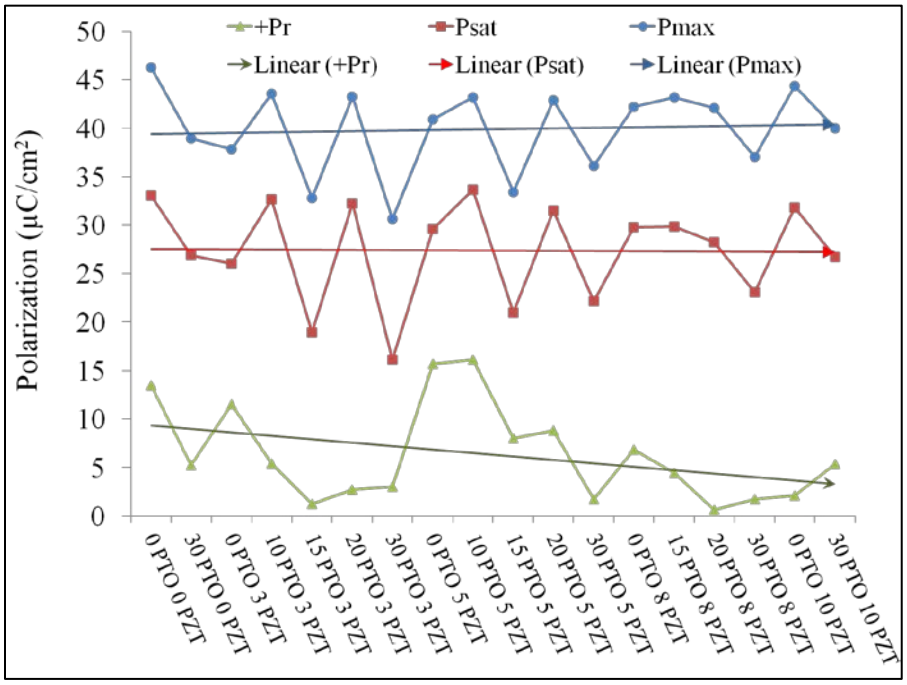

Figure 44. Hysteresis loop data plotted as a function of increasing Pb-excess in the PZT solution.

The widths of the hysteresis, corresponding to the sum of the positive and negative coercive fields, are also of importance as it describes the field required to switch the material from one state to another. The positive ($+E_c$) and negative coercive field ($-E_c$) values of the hysteresis have been plotted as a function of increasing Pb-excess in the PTO (Figure 45) and as a function of increasing Pb-excess in the PZT (Figure 46). Both figures show a trend of decreasing positive and negative coercive field values as a function of increasing Pb-excess in both the PTO and PZT solutions. This implies the hysteresis loops are narrower in samples with higher percentages of Pb-excess in both the PTO and the PZT solutions. These plots also show a few samples with disproportionate positive to negative coercive field values which are due to hysteresis loop pinching in samples 10/3, 20/5, 30/5, and 30/8, negative imprinting in samples 0/0 and 15/5, positive imprinting in samples 0/10 and 30/10, or a combination of both as in the case of samples 0/8, 15/3, 15/8, 20/3, and 20/8.

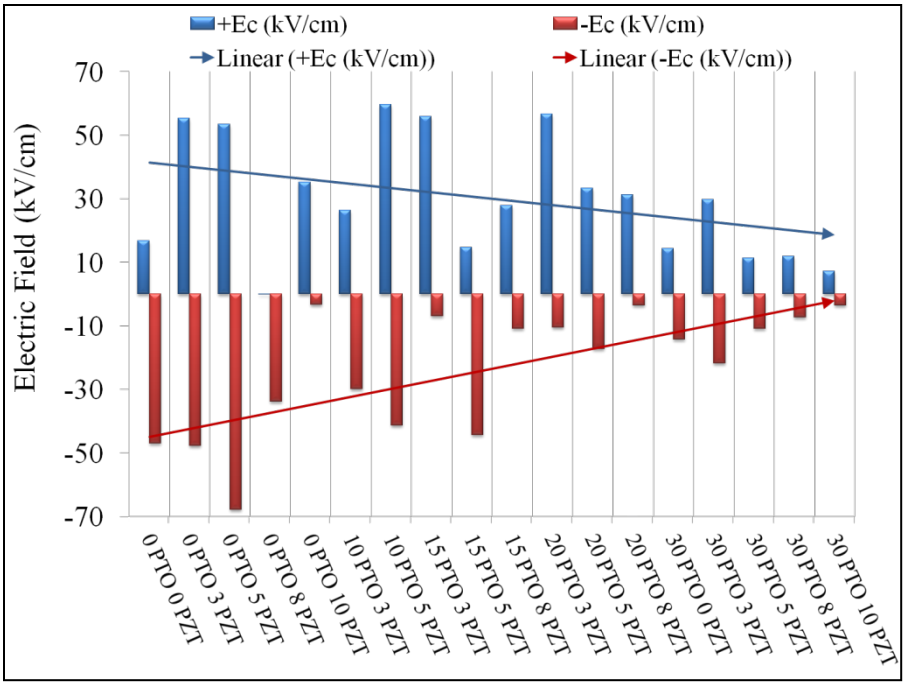

Figure 45. The coercive field values from hysteresis loop data at zero polarization plotted as a function of increasing Pb-excess in the PTO seed layer solution.

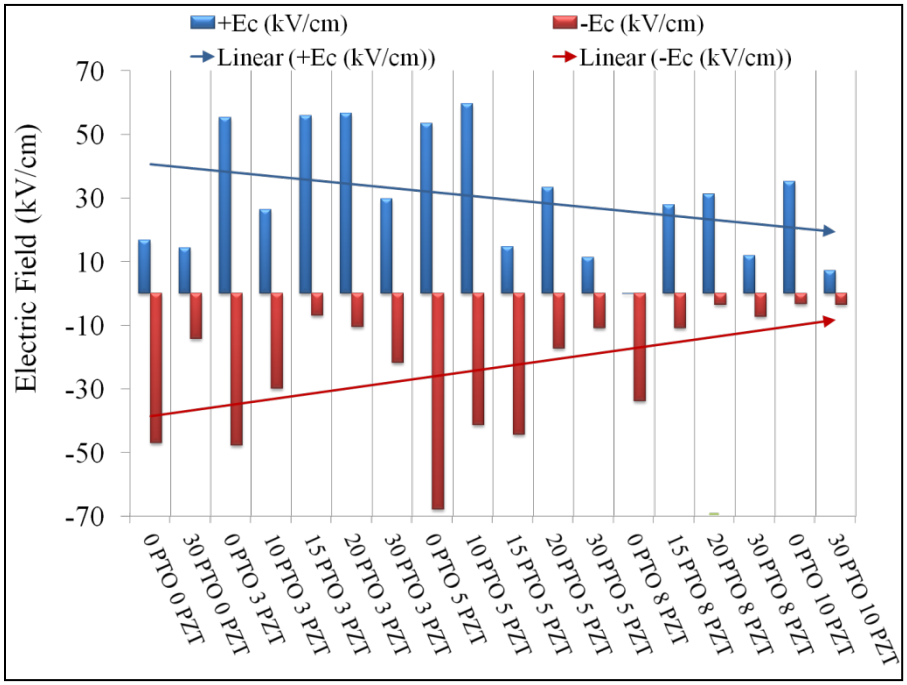

Figure 46. The coercive field values from hysteresis loop data at zero polarization plotted as a function of increasing Pb-excess in the PZT solution.

5.2.6 Electrical Sweeps in the Pb-Excess Study

Additional electrical data was collected for the Pb-Excess samples and included capacitance versus voltage data. For these tests, all samples were poled using an Agilent Technologies B1500A Semiconductor Device Analyzer. The poling voltage was set at 10 V, however the field applied on each individual sample is a function of the sample thickness. Typically, samples will be poled 2-3 times higher than the coercive voltage (~2-3 V). In this instance, the samples poling ratios were between 3-37 times the coercive field as showing in Table 10. Because of loop pinching and imprinting effects, the coercive field was taken to be half the width of the hysteresis loop.

Wafer #	PTO Pb-excess	PZT Pb-excess	Thickness (Å)	Ratio of Poling E to Coercive E
6117	0	0	4777	7
6109	0	3	5038	4
6101	0	5	5238	3
6163	0	8	4788	12
6103	0	10	4836	11
6006	10	3	5000	7
6015	10	5	5334	4
6102	15	3	5073	6
6120	15	5	6345	5
6110	15	8	4783	11
6017	20	3	4987	6
6155	20	5	5000	8
6001	20	8	4798	12
6107	30	0	5000	14
6113	30	3	5073	8
6019	30	5	5039	18
6020	30	8	4829	22
6122	30	10	5070	37

Table 10. The ratio of the poling field to half the total coercive field width.

Current measurements were taken during the 5 min poling at 10V in the Agilent Technologies B1500A device analyzer. The maximum current value was recorded after the first 50 sec of poling to ensure the system was stable. Although no significant trends are observed in the films, the addition of a linear trendline shows a general decrease in the leakage current during poling as a function of increasing Pb-excess in the PTO seed layer (Figure 47) and a smaller decrease in the leakage current data as a function of Pb-excess in the Pb-excess in the PZT (Figure 48). Several samples showed large variations in the leakage between different die. Capacitors located on the same standard device die cell showed leakage current values that were relatively close to one another however die from another location on the same wafer had very different leakage current values leading to large standard deviations in samples 0/0, 0/10, 15/3, 15/5, 30/5, and 30/8. Sample 0/8 while showing a higher leakage current than the rest of the samples, had a very low standard deviation in measurements performed on 2 capacitors in 5 different standard die cells from different sections of the wafer.

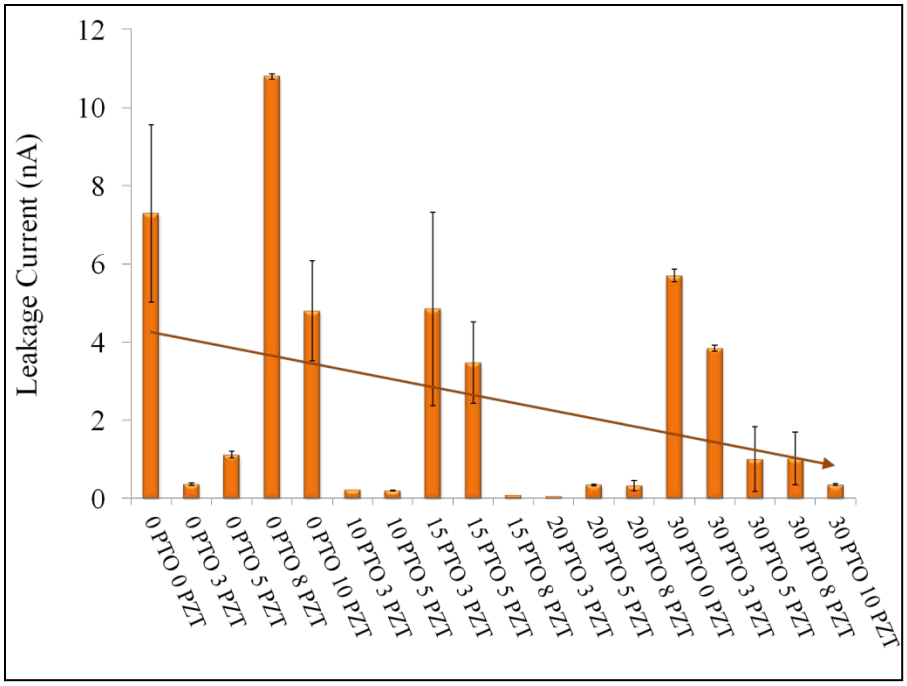

Figure 47. Maximum leakage current measured plotted as a function of increasing Pb-excess in the PTO seed layer solution.

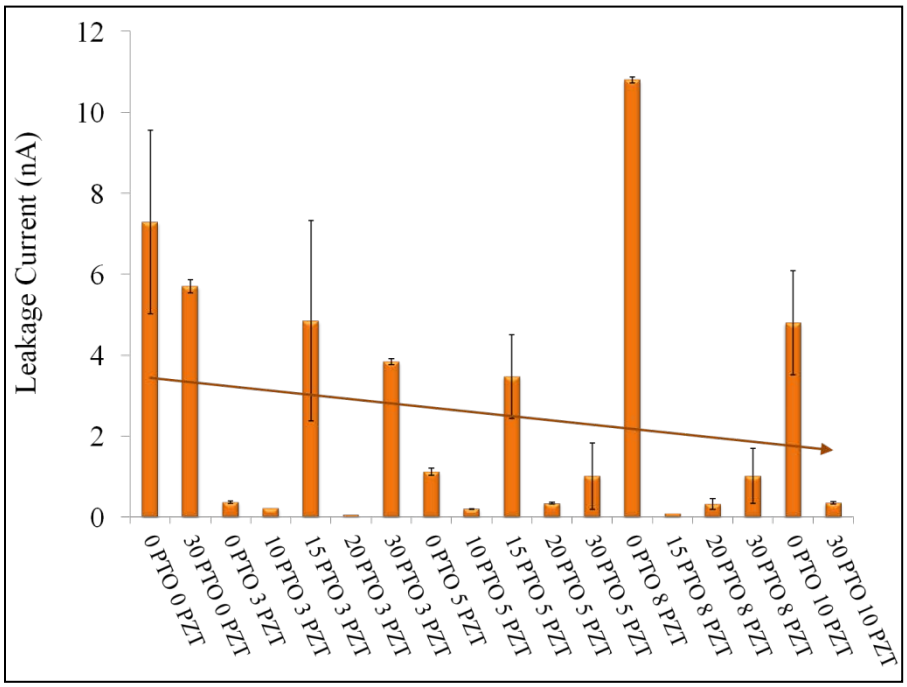

Figure 48. Maximum leakage current measured plotted as a function of increasing Pb-excess in the PZT solution.

Capacitance versus voltage (CV) sweeps were performed using the Agilent Technologies B1500A device analyzer immediately after poling for 5 min at 10 V. The films were measured between -10 V and 10 V at a frequency of 10 kHz and an AC level of 50 mV. A typical CV sweep for the PZT films is shown in Figure 49. The double hump observed in the capacitance graph is seen when there is pinching observed in the hysteresis loop. The dissipation, tanδ, for all samples were under 0.1.

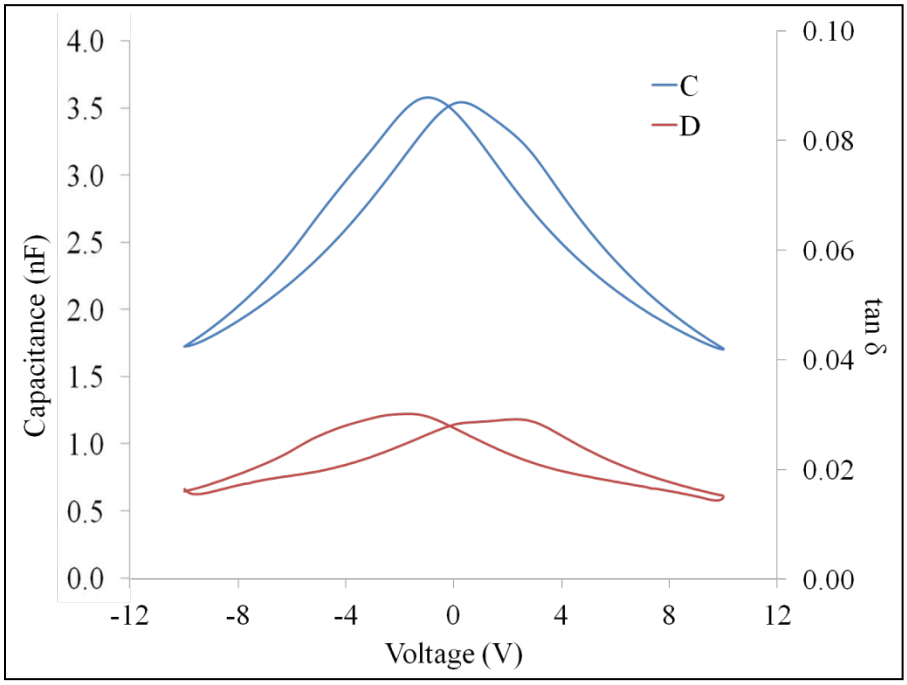

Figure 49. Capacitance and tan δ versus voltage sweep for sample 0 PTO 5 PZT.

The CV measurement was performed on all Pb-excess samples on 2 capacitors in 5 different standard die for a total of 10 measurements from each wafer. The average maximum and minimum capacitances have been plotted as well as the average tunability of the devices. The tunability of the devices, which is important in several different types of MEMS systems such as varactors and phase shifters, is the ratio between the maximum and minimum capacitance or dielectric constant of the

PZT. The average maximum and minimum capacitance, C_{max} and C_{min}, and tunability of 2 capacitors in 5 different die has been plotted as both a function of increasing Pb-excess in the PTO seed layer solutions (Figure 50) and the increasing Pb-excess in the PZT solutions (Figure 51). Linear trendlines have been added for the C_{max} and tunability for assistance. The maximum capacitance appears to increase with increasing Pb-excess in both the PTO and PZT. The increasing the Pb-excess in the PTO seed layers exhibits a larger increase in C_{max} compared to the trendline in the PZT figure. The C_{min} remained relatively close to 1.5 nF in all samples. The tunability of the films also increased, with fluctuations of about 1 or less, as a function of increasing Pb-excess in the PTO. In contrast, the tunability remained relatively constant around 2.2 when plotted as a function of increasing Pb-excess in the PZT.

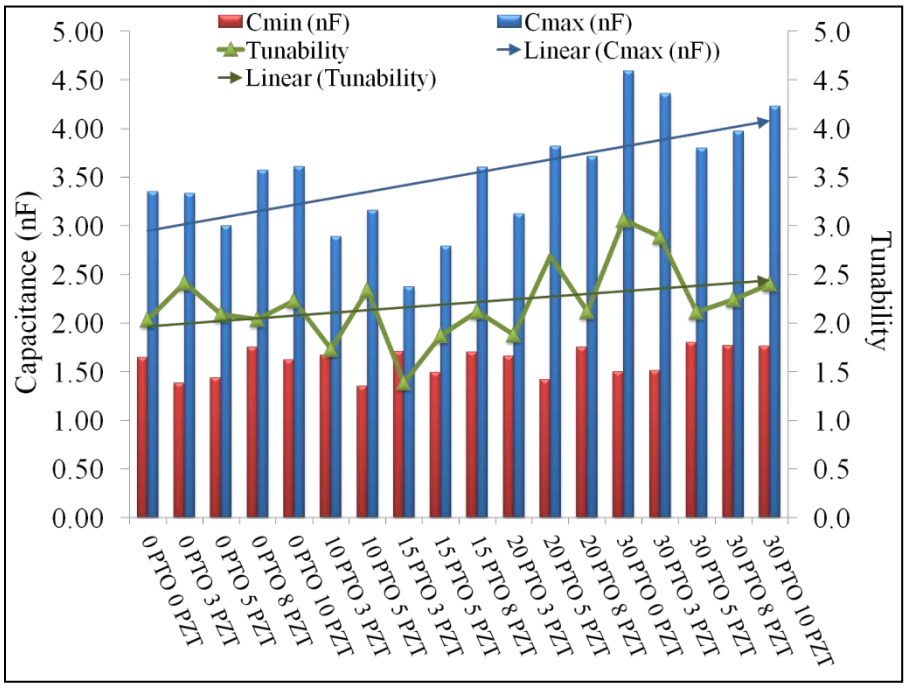

Figure 50. Maximum and minimum capacitance and tunability plotted as a function of increasing Pb-excess in the PTO seed layer solution.

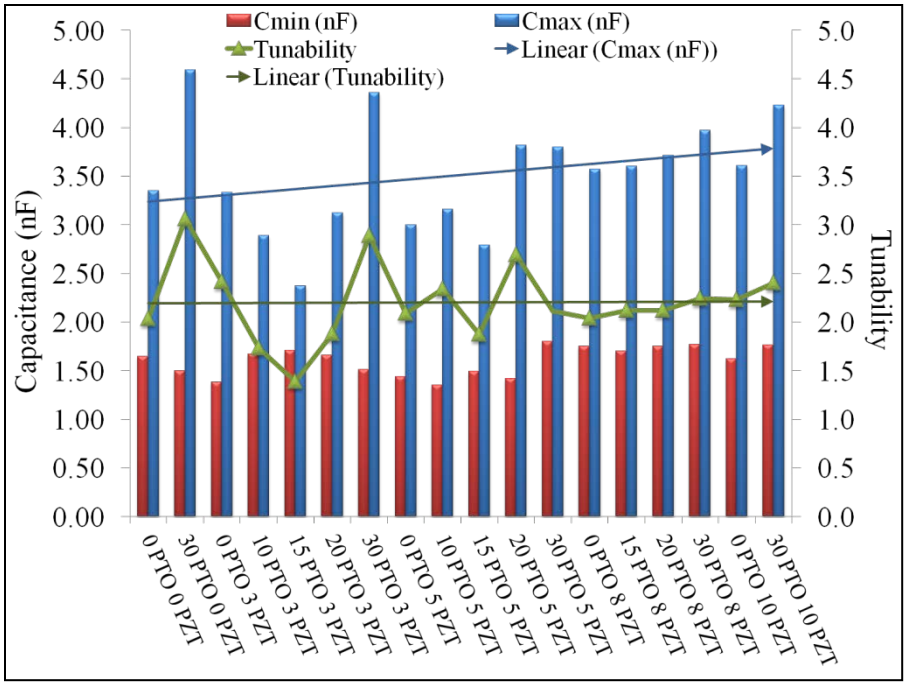

Figure 51. Maximum and minimum capacitance and tunability plotted as a function of increasing Pb-excess in the PZT solution.

The dielectric constant was calculated from the CV sweep data collected. Using the equation for capacitance of a parallel plate capacitor the capacitance, C, is known, the thickness of the dielectric, t, is the PTO/PZT film thickness, the area of the capacitors tested is 1.81E-3 cm^2, and the permittivity of free space is 8.854E-14 F/cm.

$$\varepsilon = \frac{Ct}{\varepsilon_o A}$$

The dielectric constant for all the films followed similar trends to the capacitance, which was expected. The films with 30% Pb-excess in the PTO seed layer showed the highest dielectric constants, approximately 1100 and higher (Figure 52). The same trends are observed when the data is plotted as a function of increasing Pb-excess in the PZT solution (Figure 53). The Pb-excess in the PTO plays an important role in the dielectric constant of the material as the increase in the trendline

slope is 1.5 times greater than the trendline slope for the Pb-excess in the PZT solutions.

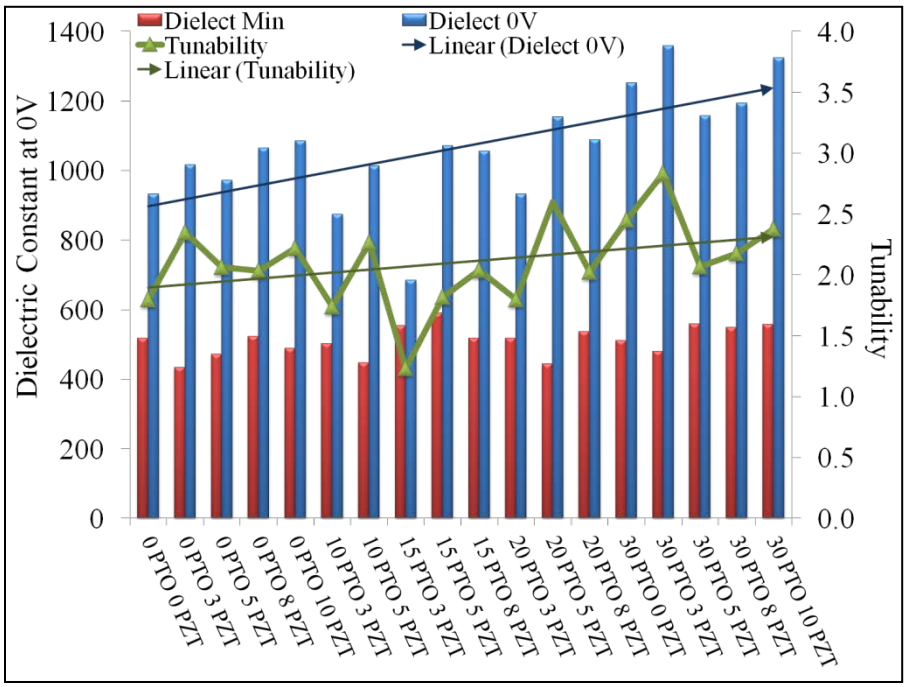

Figure 52. Dielectric constant and tunability plotted as a function of increasing Pb-excess in the PTO seed layer solution.

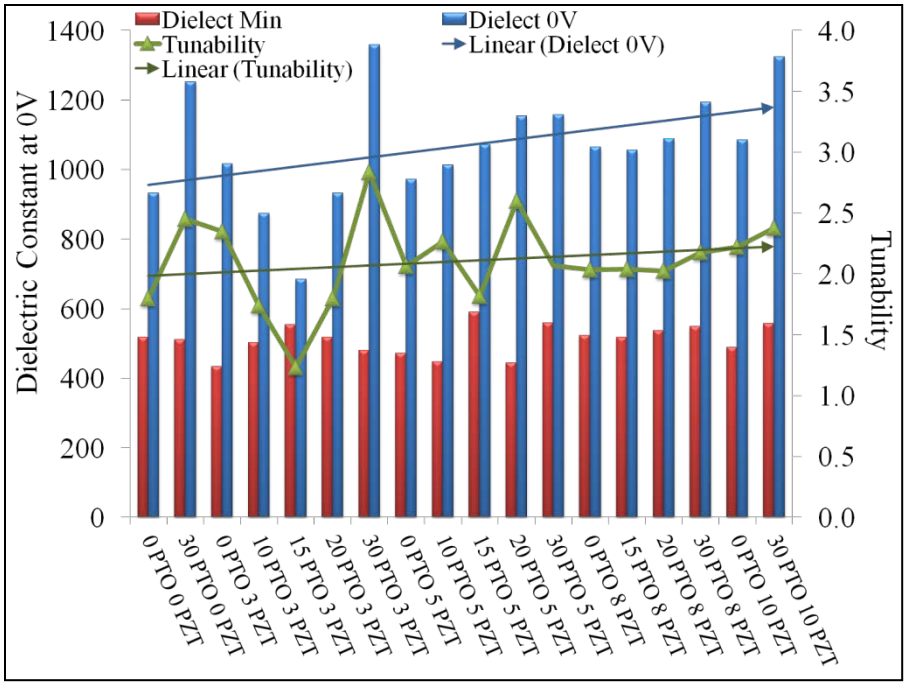

Figure 53.Dielectric constant and tunability plotted as a function of increasing Pb-excess in the PZT solution.

The electric field required to breakdown the PTO/PZT films was measured using the Agilent Technologies B1500A device analyzer. The breakdown measurement is performed as a one direction sweep from 0 V to 100 V with a compliance of 1 μA. No notable trends are observed as a function of increasing the Pb-excess in the PTO seed layer (Figure 52) or the PZT solutions (Figure 53). In Figure 53 there is a slight increase in the breakdown field in the 3% and 5% Pb-excess PZT samples. This may be related to the tilt observed in the hysteresis loop data which implies the presence of a low permittivity dielectric layer on the surface of the PZT. This low permittivity layer reduces the potential that the PZT is exposed to allowing the entire stack to operate at higher voltages even though the PZT would breakdown had that dielectric layer not been there.

$$E_{PZT} = xE_{Dielectric,\ x} + yE_{Dielectric,\ y} + \frac{\varepsilon_{Dielectric}}{\varepsilon_{PZT}} E_{Dielectric,\ z}$$

This layer would also limit the performance of these samples resulting in lower capacitance values and require higher voltages for optimal performance in these films.

$$C = 2\left(\frac{\varepsilon_{Dielectric}\varepsilon_{PZT}}{\varepsilon_{Dielectric} + \varepsilon_{PZT}}\right)\left(\frac{\varepsilon_o A}{t}\right)$$

A device with a low dielectric constant material on top of the PZT will resemble a capacitor in series, ultimately reducing the total capacitance of the device. Sample 30/10 also exhibited high breakdown abilities however it has a large standard deviation with different standard die capacitors breaking down at drastically different fields. Capacitors within the same die showed similar breakdown strengths.

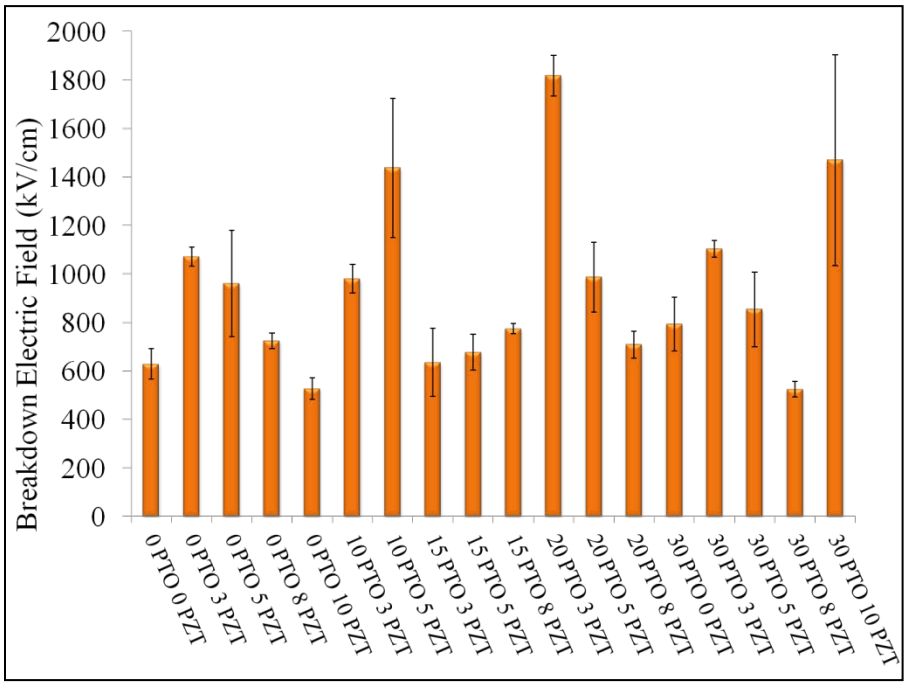

Figure 54. Breakdown field measurements plotted as a function of increasing Pb-excess in the PTO seed layer solution.

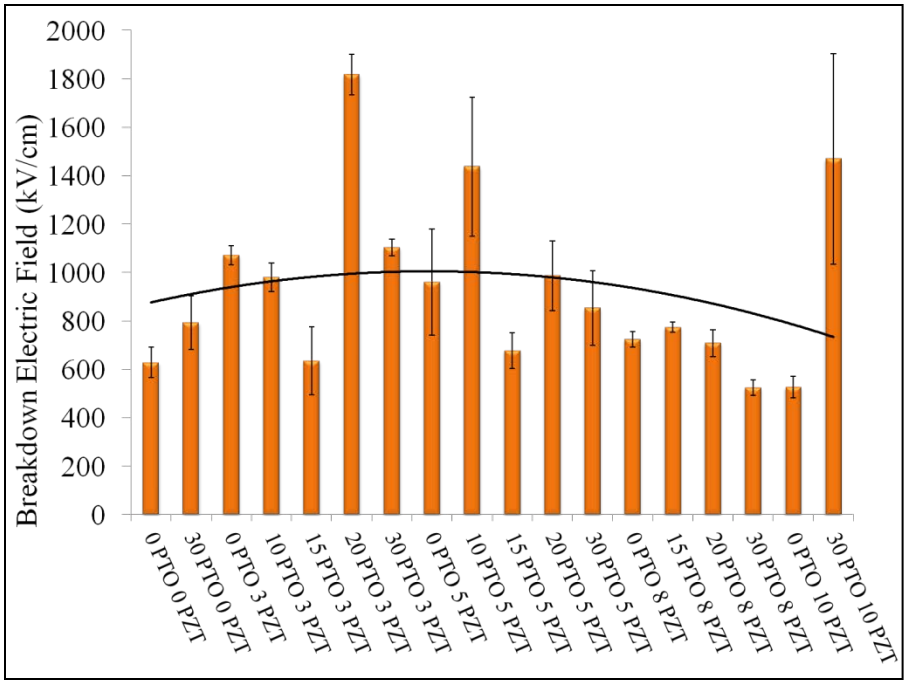

Figure 55. Breakdown field measurements plotted as a function of increasing Pb-excess in the PZT solution.

There have been several reports that have correlated larger grain sizes to improved electrical properties, in particular higher remanent polarization values [95][96][97]. In this study no correlation has been observed to state that the grain sizes influence the electrical properties of the PZT films. The normalized grain size was plotted with the normalized max and remanent polarizations (Figure 56)

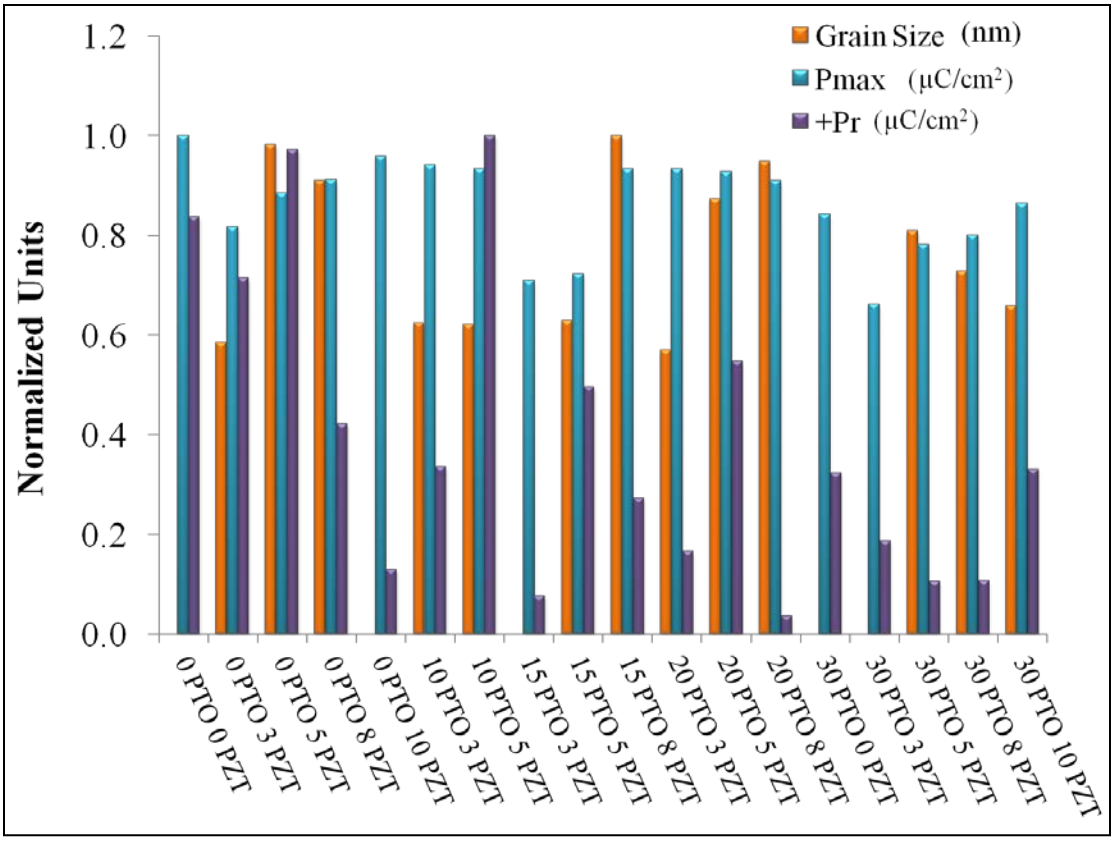

Figure 56. Comparison of the film grain sizes and polarization values plotted as a function of increasing Pb-excess in the PTO seed layer solution.

As expected the film breakdown strength and the leakage current inversely follow one another (Figure 57). Films that exhibited high breakdown strength showed low leakages. Particularly, films with 3% and 5% Pb-excess in the PZT showed high breakdown strengths and low leakage currents. There is an exception however in those films when paired with 15% Pb-excess PTO which also performed poorly in the hysteresis measurements and dielectric tunability.

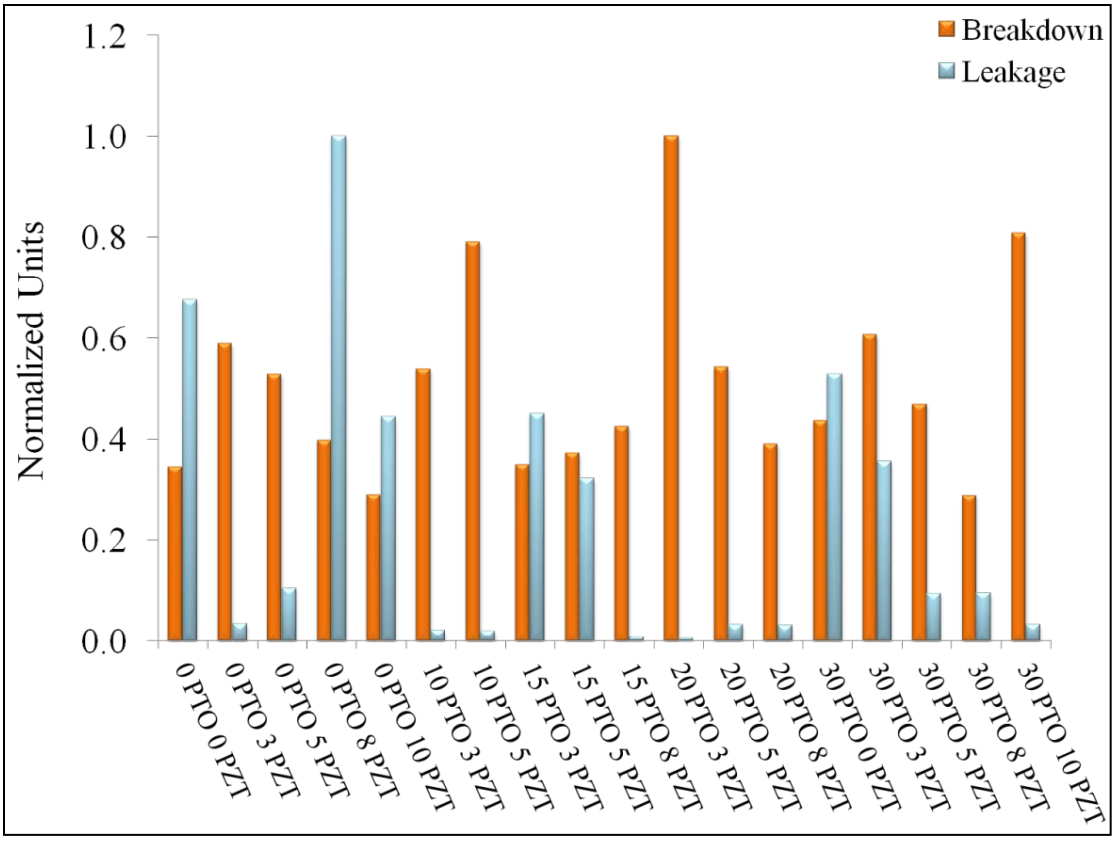

Figure 57. Comparison of the film breakdown strength and leakage current values plotted as a function of increasing Pb-excess in the PTO seed layer solution.

Investigating the influence of the different film orientations on the electrical properties of PZT showed correlation between the (111) PZT orientation and the remanent polarization of the films (Figure 58). Plotting the results as a function of increasing Pb-excess in the PZT, most of the films follow similar trends between the Lotgering factor of the (111) orientation on the films and the remanent polarization. The group of samples with 3% Pb-excess in the PZT solutions show an inverse relationship with the Lotgering (111) results.

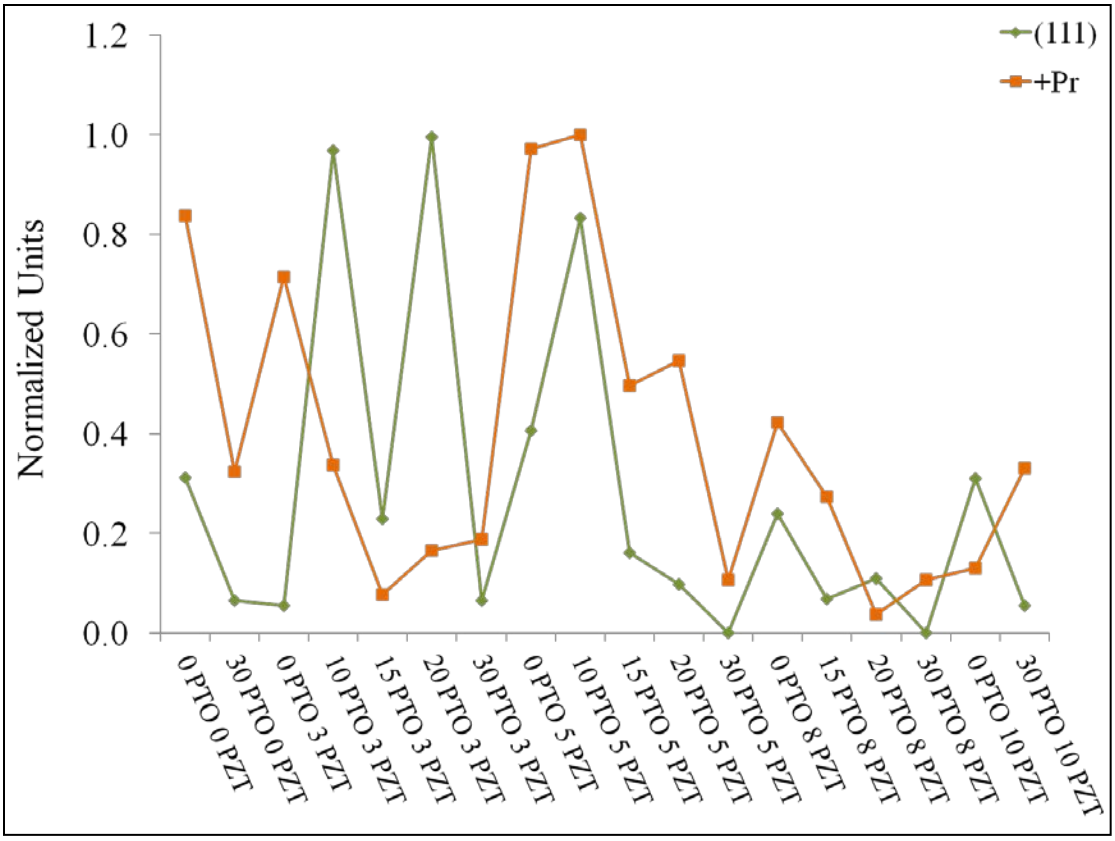

Figure 58. Comparison of the remanent polarization (P_r) and the Lotgering (111) orientation in the films.

5.2.7 Displacement Measurements in Cantilever Arrays

Using the cantilever arrays, displacement measurements were performed with a Polytec MSV laser Doppler vibrometer (LDV) system at a frequency of 2 Hz. The samples were poled at either 9.8 V or -9.8 V for 3 minutes depending on whether they were positive or negative measurements, prior to acquiring data. All the samples were swept from 9.8 V to 0 V and then from -9.8 V to 0 V ten times and 2 cantilever arrays from 2 different standard die cells were used. Due to the out-of-plane deflection/curvature of the cantilevers (Figure 59), it was nearly impossible to obtain significant displacement data especially from the longer device lengths and additionally the signal variances on each data cycle was vary large (see earlier Figure 32). To improve the data acquisition, a 30° sample holder was fabricated to provide sufficient tilt to the sample (Figure 60), enabling a larger portion of the reflected optical beam to be visible inside the optical column of the microscope.

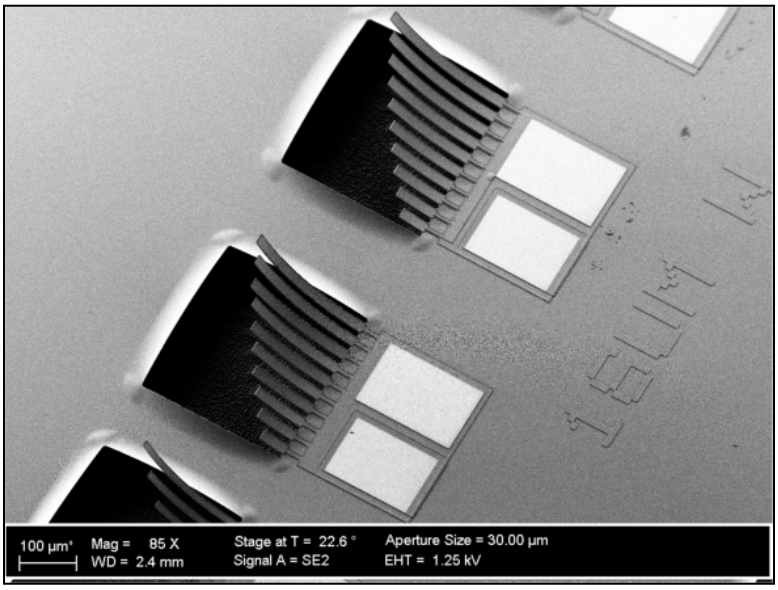

Figure 59. SEM image of cantilever arrays fabricated on a sample with 30% Pb-excess PTO and 10% Pb-excess PZT (52/48). Large deflections are observed in all films fabricated.

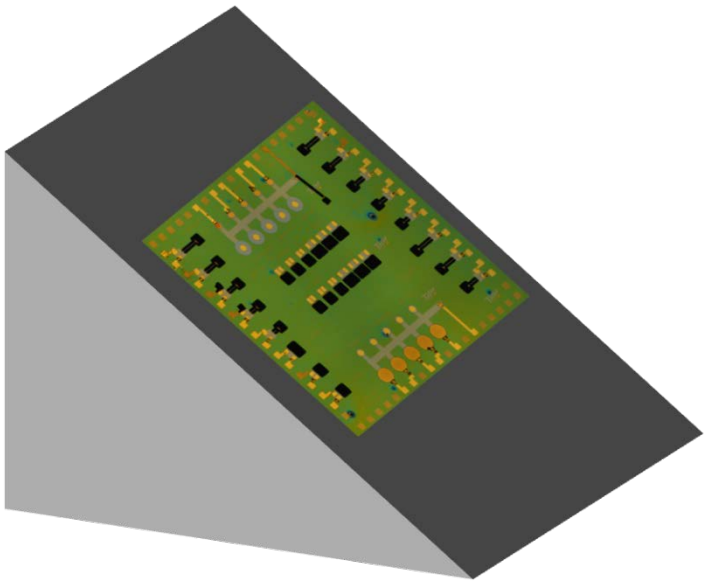

Figure 60. Schematic of the 30 degree wedge fabricated to tilt sample for LDV measurements.

The Polytec LDV system allows for non-contact displacement measurements using a laser beam to track cantilever displacement. Three points were selected on the tips of the first four cantilevers of the arrays fabricated, 52 µm, 77 µm, 102 µm, and 127 µm (Figure 61a). There were 10 sweeps performed at each point and the displacement as a function of and reference voltage as a function of time were plotted (Figure 61b).

a)

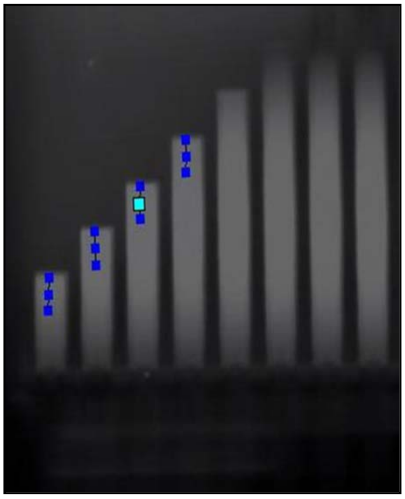

b)

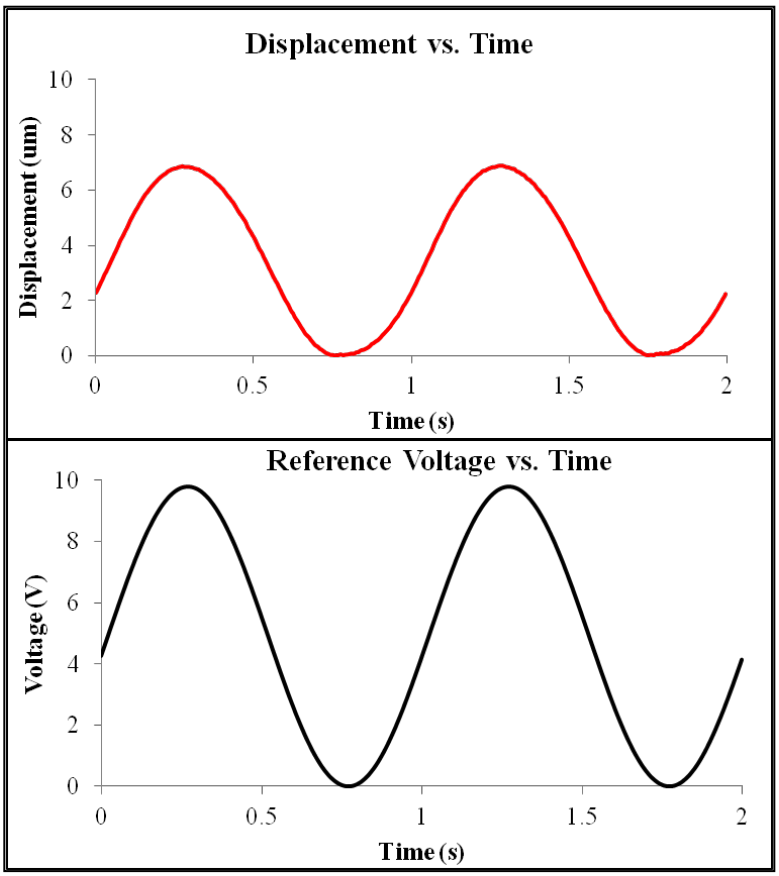

Figure 61. a) Image from the Polytec software showing the cantilevers and points about to be tested. b) Displacement versus time and reference voltage versus time, as shown by the software.

A standard unipolar sweep of the data will show hysteresis in the displacement versus voltage data, which is typical in these types of materials (Figure 62). Two unipolar sweeps for sample 0/5 is shown. The current measurement acquisition system does not allow for a bipolar sweep displacement acquisition. After poling the material for 3 minutes at – 9.8 V, a sweep from -9.8 V to 0 V, 10 times at each of the 12 points. The data does not show drift between loops which demonstrates a lack of material fatigue in the time the measurements were taken. The same procedure was performed in all samples of the Pb-excess study with the exception of samples 0/8 and 15/3 since wafers were damaged during processing.

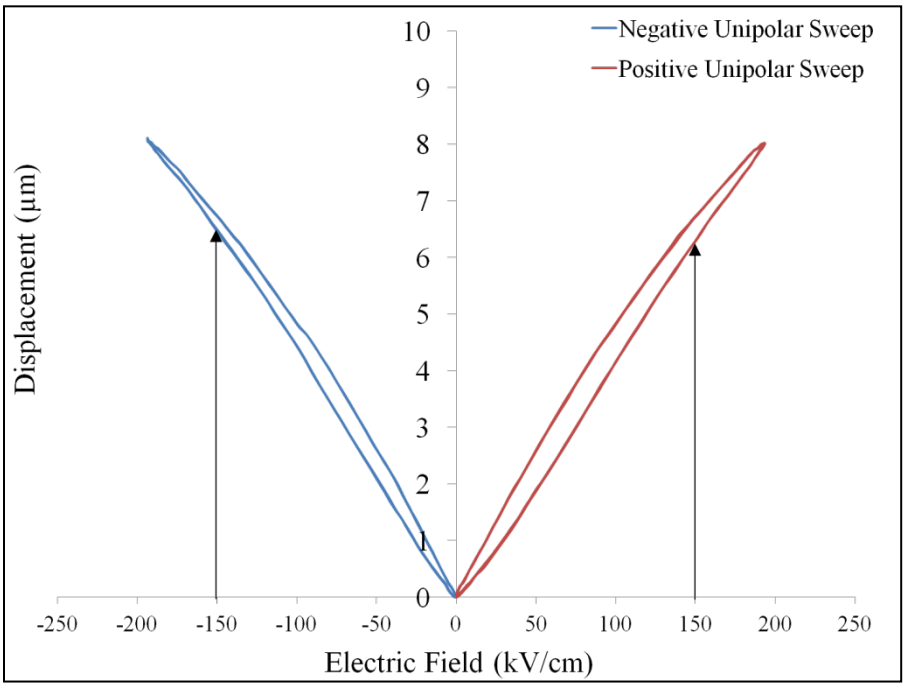

Figure 62. Unipolar sweep from -10 V to 0V and then 10 V to 0 V in a sample with 30% Pb-excess in the PTO and 10% Pb-excess in the PZT solution.

The data shown in Figure 63 and Figure 64 are plotted as a function of Pb-excess in the PTO seed layer solutions and in the PZT solutions and were taken on a

cantilever of 127 µm length. The data was plotted at two measured fields, -150 kV/cm and +150 kV/cm, for simplicity, as designated by the two black arrows in Figure 62. The general trends show that films with the higher Pb-excess in the PTO seed layer exhibited higher deflection values (Figure 63). Sample 30/10 showed the most symmetrical loops while most of the samples exhibited preferential positive displacement. Sample 0/10 exhibited the highest displacement

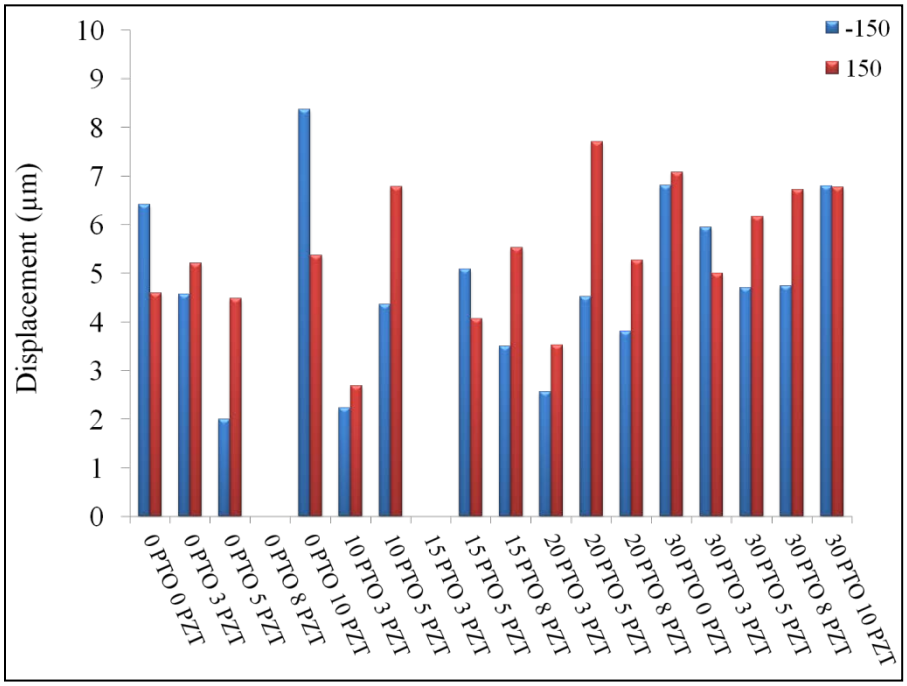

Figure 63. Displacement data for cantilevers with a length of 127 µm at a field of -150 kV/cm and 150 kV/cm are plotted as a function of increasing Pb-excess in the PTO seed layer solution.

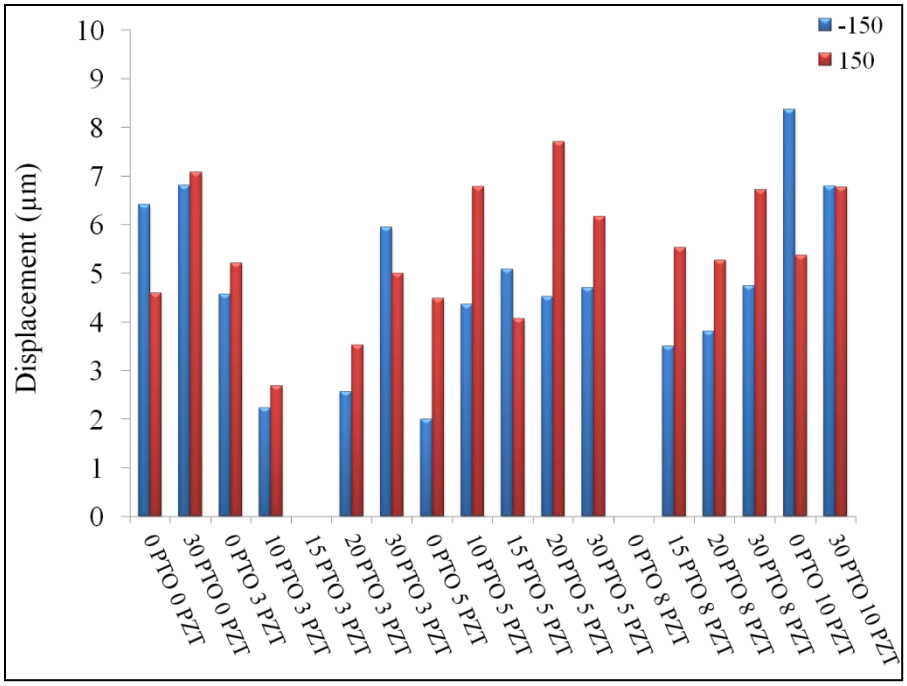

Figure 64.Displacement data for cantilevers with a length of 127 µm at a field of -150 kV/cm and 150 kV/cm are plotted as a function of increasing Pb-excess in the PZT solution.

To further understand the displacement results of the films, the hysteresis loops and both positive and negative unipolar displacement measurements were plotted together for samples 0/5, 0/10, and 30/10 (Figure 65). Sample 0/5 exhibited the hysteresis loop with the largest coercive field as well as lower displacement values. Sample 0/10 showed the largest negative displacement and asymmetric, pinched, and tilted hysteresis loop. The negative electric field had the narrower half of the hysteresis and also had the higher displacement curves. Sample 30/10 had nearly symmetric unipolar displacement loops and nearly no pinching in the symmetric hysteresis loops. There appears to be a relationship between the widths of hysteresis loop to the maximum displacement. Sample 0/5 depicts a material that requires a larger electric field to switch the domains in the direction of the field. It seems reasonable to assume that a material requiring higher fields for switching would result in cantilevers that have lower displacement values than a material that needs lower fields for the same switching behavior. That being the case figure 65 a, b, and c depict the influence the width of the hysteresis loop has on the displacement as the switching behavior is related to the strain.

a)

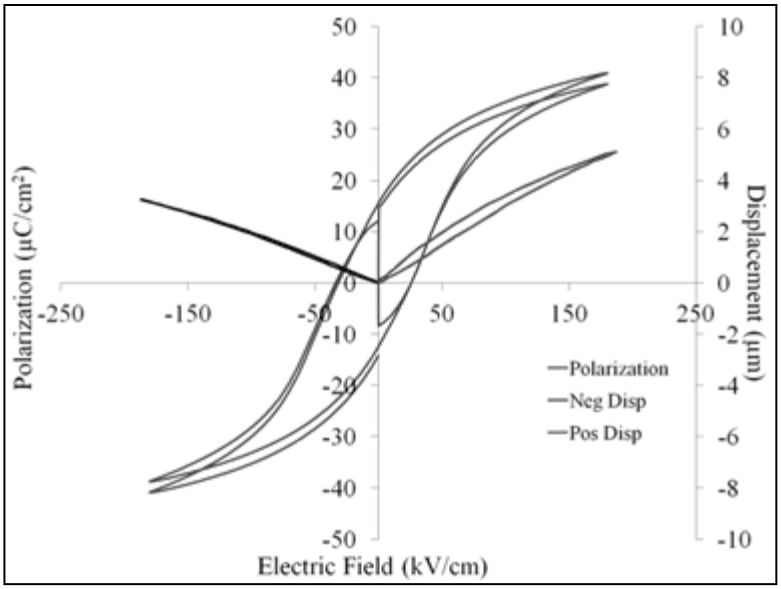
Polarization (μC/cm²)
Displacement (μm)
Electric Field (kV/cm)
Polarization
Neg Disp
Pos Disp

b)

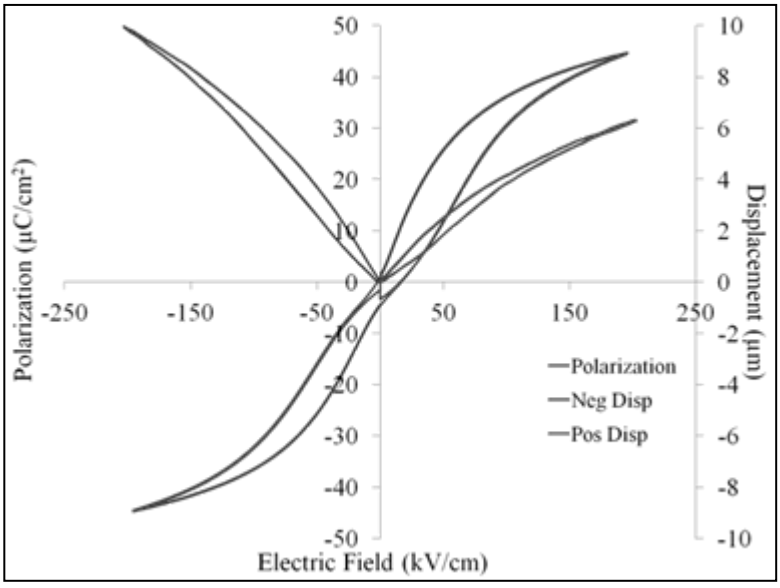
Polarization (μC/cm²)
Displacement (μm)
Electric Field (kV/cm)
Polarization
Neg Disp
Pos Disp

c)

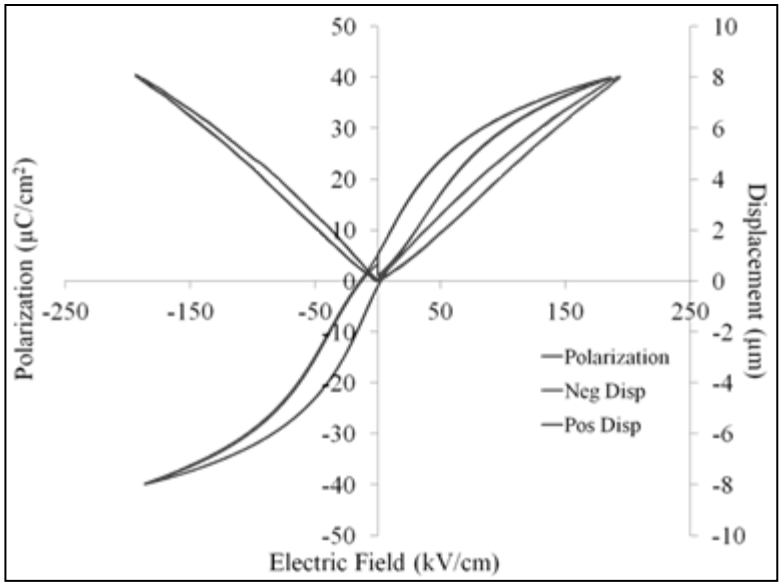

Figure 65. Hysteresis and displacement measurements of samples a) 0/5 b) 0/10 and c) 30/10.

The main contributor in the influence of the electrical properties of PZT(52/48) is the percentage of Pb-excess in the PTO solution. Higher percentages of Pb-excess used in the PTO seed layer solutions led to decreases in the percentage of (110) and (111) orientations, P_{max}, P_{sat}, and P_r, E_c and leakge currents while increasing the percentage of (001) and (100) orientations, C_{max}, dielectric constant, tunability, and piezoelectric induced actuator displacement.

The PTO seed layer with a 30% Pb-excess showed the most improvements with greater than 90% (001) orientation and dielectric constants larger than 1000.While the Pb-excess the PZT did not show a large influence in the electrical and piezoelectric properties of the PZT films, the film with 30% Pb-excess in the PTO and 3% Pb-excess in the PZT showed the best film properties. Higher amounts of Pb-excess in the PZT may oversaturate the film leading to excess lead in the grain boundaries which may provide conduction pathways for shorting, breakdown, in the film.

	30 PTO 3 PZT	**30 PTO 5 PZT**	**30 PTO 8 PZT**	**3 PTO 10 PZT**
Displacement	1.7 µm	1.4 µm	1.4 µm	1.5 µm
Dielectric Constant	1380	1180	1190	1320
Breakdown	1100 kV/cm	830 kV/cm	510 kV/cm	1480 kV/cm
***f*(001)**	0.93	1.00	1.00	0.94

Table 11. Summary of samples with 30% Pb-excess in the PTO seed layer.

Chapter 6: Orientation Control in PZT (52/48) Multilayer Actuators

6.1 Benefits of Multilayered Systems

A literature search shows a large amount of research focused on multilayer capacitors using different piezoelectric materials deposited through various techniques. Higher capacitance values can be obtained by increasing the active electrode area or by decreasing the film thickness as shown in the equation for the capacitance of a parallel plate capacitor.

$$C = \frac{k\varepsilon_o A}{t}$$

Thinner and denser dielectric films for multilayer capacitors have been reported using chemical solution deposition [98]. These films ranged from 50 nm – 250 nm in thickness. More recently, reported research on multilayer actuators has increased showing an improvement in capacitor density, smaller packaging, and faster response times with lower power consumption [99][100][101]. A very thorough publication on piezoelectric multilayer capacitors can be found in [102] and [103] and a brief theoretical understanding of multilayer actuators can be found in [104]. However, these previous efforts fail to provide information on the texture of each individual piezoelectric thin film. As the material properties are highly dependent on the texture of the film, a controlled method of maintaining high (001) texture within each of the piezoelectric thin film layers is desirable.

Incorporating a multilayer configuration in PZT thin film based MEMS actuators can overcome one of the principle limitations of traditional MEMS unimorph actuators, namely, the inability to achieve large bi-directional displacements at electric fields larger than the coercive field. In contrast, multilayer actuators can independently control PZT layers both above and below the neutral axis, enabling true bi-directional displacements for the same strain state in the piezoelectric multilayer composite. Moreover, multilayer MEMS actuators offer several additional advantages including lower power, lower drive voltages, higher forces, and increased actuator work per unit areas.

As shown in Figure 66 for a cantilever actuator comprised of a SiO_2 elastic layer and Pt/PZT/Pt actuator layers (with a PZT thickness of 0.25μm), the predicted blocking force and maximum work per unit area increases for each additional PZT actuator layer added to the overall structure (Figure 67). The blocking force is the force exerted by a piezoelectric actuator while fully mechanically clamped or equivalently the maximum force that can be generated by the actuator. For this model, the piezoelectric coefficient of the actuators is assumed to be the same for each additional actuator layer. To achieve the benefits highlighted above, maintaining a high degree of (001) texture and therefore a high piezoelectric coefficient for each actuator layer is crucial. This chapter discusses a method of fabricating a highly (001) textured multilayer PZT thin film composite and reports on the experimental results from both multilayer capacitors and actuators.

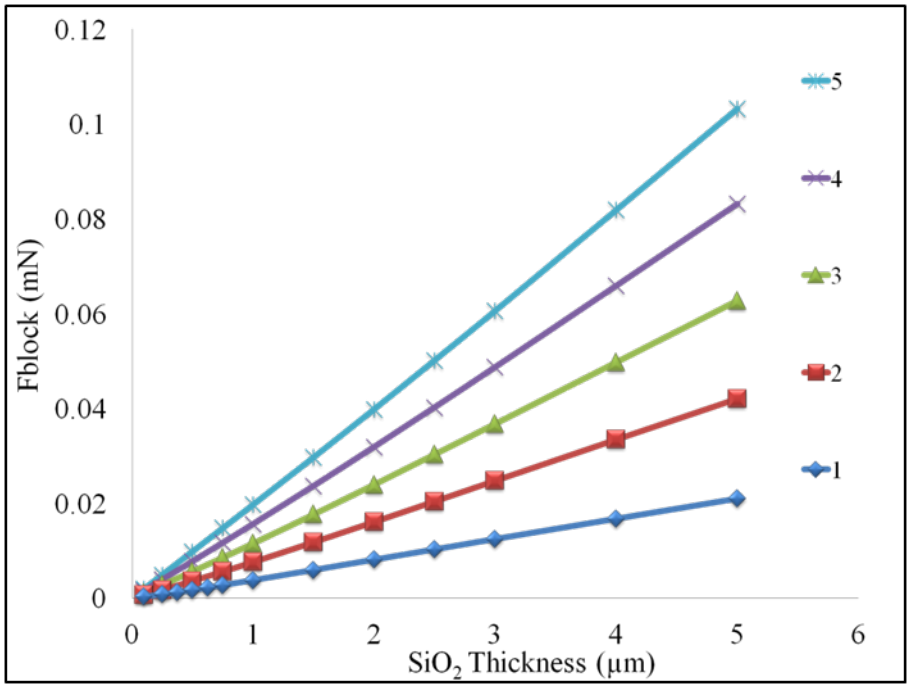

Figure 66. Predicted blocking force for a sample with varying SiO_2 thicknesses and additional Pt/PZT/Pt layers. Model provided by Jeffrey Pulskamp of the US Army Research Laboratory, Adelphi, MD.

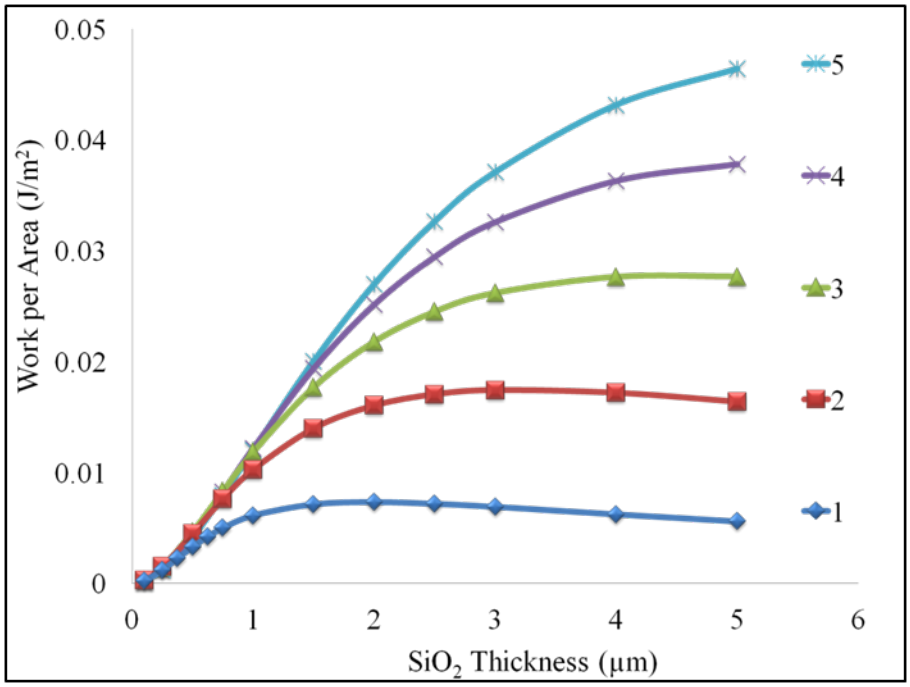

Figure 67. Predicted work per area for samples with varying SiO_2 thicknesses and additional Pt/PZT/Pt layers. Model provided by Jeffrey Pulskamp of the Army Research Laboratory Adelphi MD.

6.1.1 Sol-gel Procedures for Multilayered Capacitors and Actuators

The 0.15 Molar 30% Pb-excess PTO and 0.4 Molar 10% Pb-excess PZT (52/48) films were prepared as described in section *3.1*. The films were deposited following the same sol-gel procedures used throughout this thesis to a film thickness of approximately 250 nm. Following the final crystallization anneal, the PZT layer was coated with 500 Å Pt using the CLC at 500°C. After this coating the samples were x-rayed with a Rigaku Ultima III Diffractometer with Bragg-Brentano Optics. To create the multi-layer coatings, the samples were coated with another 250 nm of PZT with and without a PTO seed layer in subsequent layers as shown in sample A in Figure 68. Again a 500 Å Pt layer was deposited and x-ray diffraction measurements were performed. This sequence was repeated until a 4-layer Pt/PZT multilayer structure was created (Figure 68).

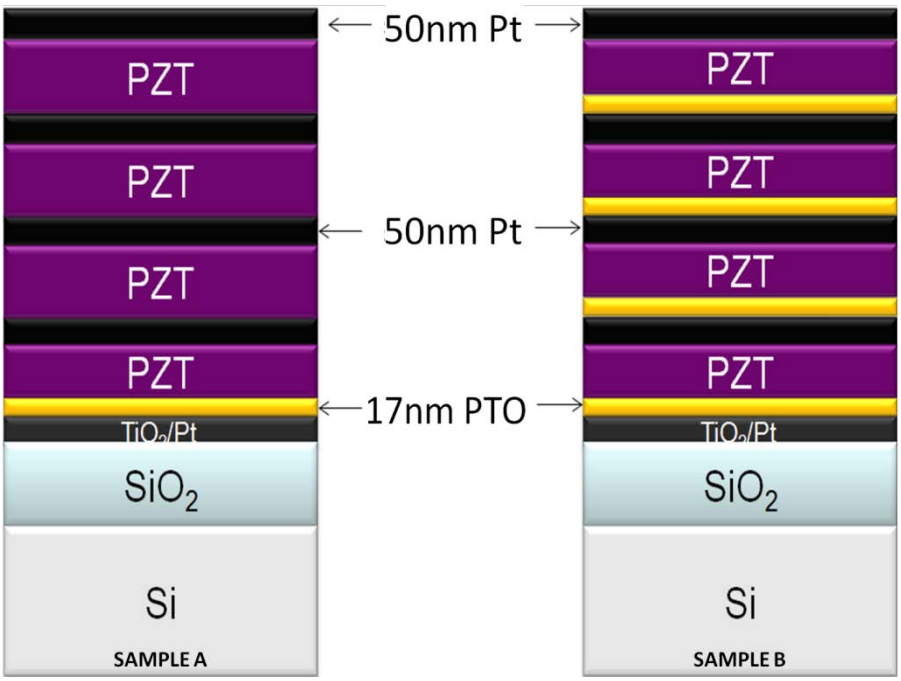

Figure 68. The two different multilayer stack configurations. One sample had the PTO seed layer only on the first Pt/PZT layer the other layer had the PTO seed layer between each Pt/Pzt layer.

To investigate the texture control within the multilayers, two samples were prepared. Sample A used the $PbTiO_3$ seed layer on only the first, closest to the Si wafer, Pt interface. Sample B included the $PbTiO_3$ on all Pt/PZT interfaces for orientation control (Figure 68). The purpose was to determine if the texture obtained on the initial PZT layer could be maintained throughout the entire multilayer stack. In addition to x-ray characterization, the ferroelectric, dielectric, and piezoelectric properties of the multi-layer coatings was evaluated. Testing of the multilayer PZT samples involved fabricating capacitors and cantilever arrays capable of making contact to all 5 Pt layers. Dielectric properties were measured with HP 4192A LCR impedance analyzer with a small signal, 50 mV rms, wave at a frequency of 10 kHz. The piezoelectric induced displacements were measured with a Polytec MSV Laser Doppler vibrometer.

6.1.2 Fabrication of Multilayered PZT Devices

The capacitors and cantilever arrays were fabricated using a five ion-mill process to pattern the PZT and Pt layers. The wafers were coated with Clariant AZ5214E photoresist using an EVG 120 Automated Resist Processing System. A Karl Suss MA/BA6 contact aligner was used for photolithography. After the exposure the image was developed in AZ300MIF. A 5 minute descum with an oxygen plasma was performed using the Metroline/IPC Plasma Photoresist Stripper to remove any unpatterned resist that remained on the surface. In preparation for ion milling, the wafer was then UV cured using an Axcelis UV Photostabilizer, which further hardens the resist. A 4wave 4W-PSIBE Ion Beam Etch system is used for ion milling. Using a secondary ion-mass spectrometer endpoint detection system during the etch, the ion-milling process was terminated after exposing and removing a Pt layer. Subsequently, the resist was removed and this process was repeated using a slightly larger photomask area (approximately 5 μm offset between layers) until all electrodes are exposed (Figure 69).

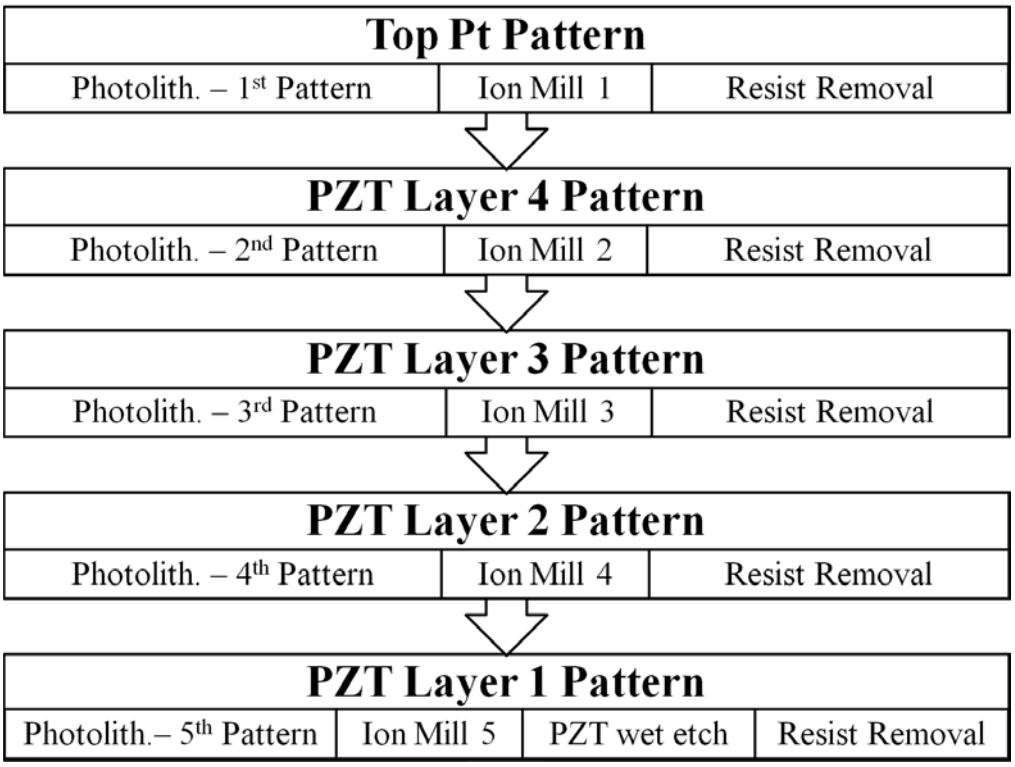

Figure 69. Ion mill processing procedures to expose bottom Pt electrode in a 4 PZT layer multilayer device.

6.2 PZT (52/48) Properties in Multilayer Devices

6.2.1 XRD Analysis of Orientation Control in 4-Layer Stacks

The samples were analyzed using X-Ray Diffraction (XRD) after every PZT/Pt layer to determine the effects of each additional layer on film orientation. The XRD data shows a contribution of all deposited layers to the overall film orientation at the time the data was collected. Figure 70 shows the (001) and (100) orientation as a function of deposition layer for sample A. The first layer consisted of the bottom Pt/PTO/PZT and a strong {100} peak is observed. Peak broadening is noted in subsequent layers and peak intensity diminishes in the overall stack by the final layer. Using the Lotgering factor to quantify the percentage of orientation in the {100}

family, a significant decrease in orientation is observed. The first PZT layer is nearly 100% oriented along the (001) and (100) directions. By the second, third, and fourth layers the orientation across the deposited film has dropped by 7%, 17%, and 44% relative to the first layer, respectively (insert in Figure 70). By the top most PZT layer deposition, orientation across the entire stack resembles a randomly oriented PZT without any film optimization on Ti/Pt electrodes instead of highly (111) optimized TiO_2/Pt electrodes as described in chapter 4.

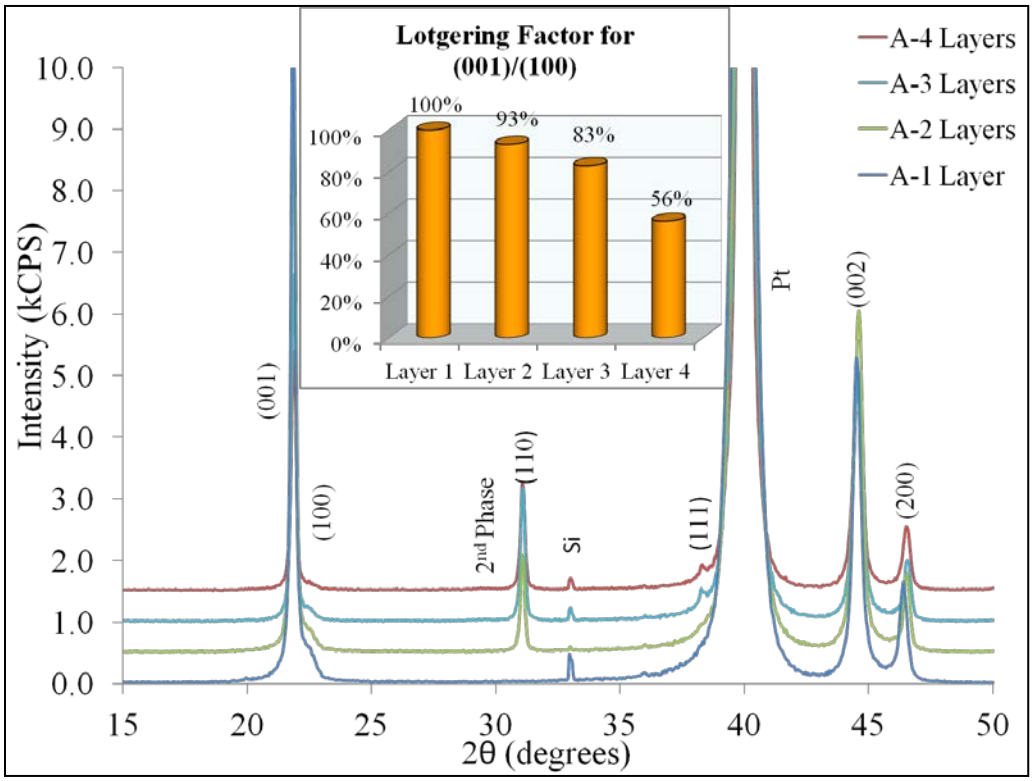

Figure 70. XRD data for Sample A showing degradation in film orientation in the overall film texture.

Sample B (Figure 68) using the PTO seed layer in between every Pt and PZT layer exhibited a significantly improved orientation compared to Sample A (Figure 71). High degrees of {001} orientations with {100} Lotgering factors values of 90% and greater were maintained in all four layers of the multilayer stack, as shown in the insert in Figure 71, leading to a high degree of orientation across the entire stack. The 30% Pb-excess PTO seed layer was crucial to maintaining the high {001} orientation and is required for every PZT layer within the multilayer stack.

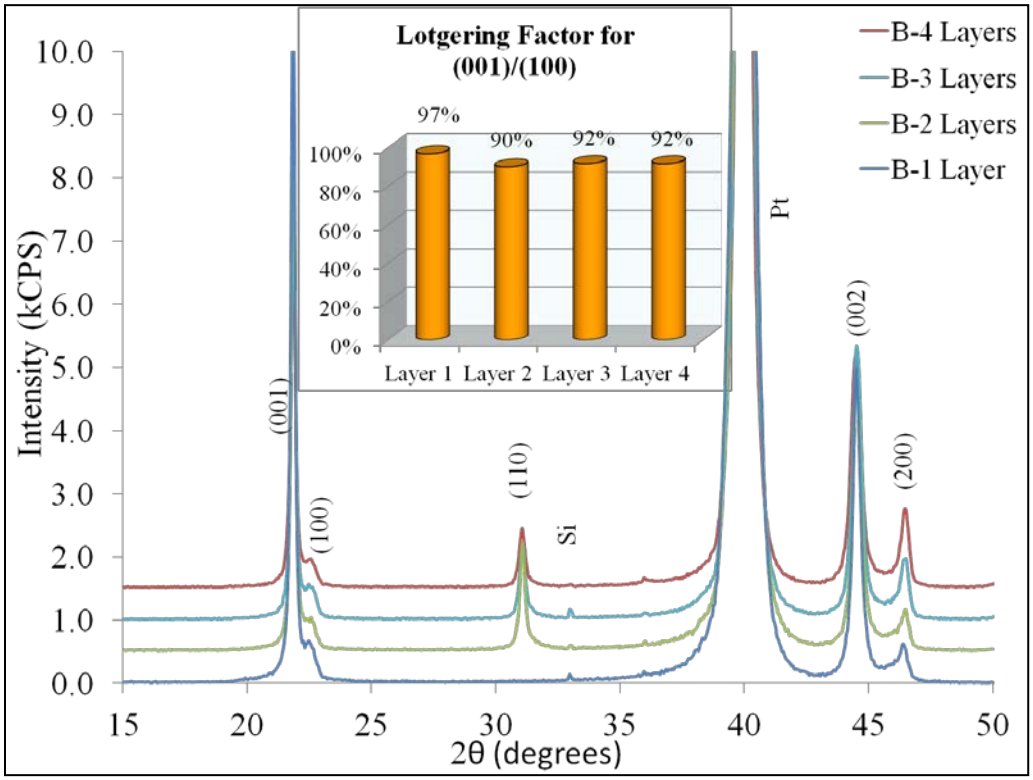

Figure 71. XRD data for Sample B showing minimal degradation in film orientation in the overall film texture.

6.2.2 Dielectric Properties Studies of a 4-Layer Stack

Parallel plate capacitors were fabricated as described in Figure 69, with all 5 platinum electrodes exposed to allow access for electrical contact (Figure 72). The color variations shown in Figure 72 are due to the variations in the multilayer stack thickness with the ~50nm Pt electrodes semitransparent to optical light. There is a small variation in the capacitor electrode area (Table 11) to prevent shorting between layers with the top most electrode, PZT layer 4, consisting of the smallest area and the bottom most, PZT layer 1, with the largest area.

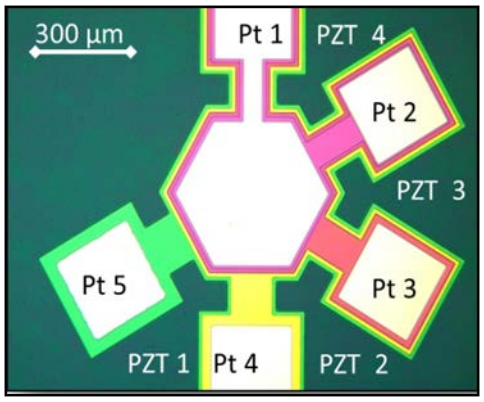

Figure 72. Optical Microscope image of a multilayer capacitor. The color variations result from the thickness differences in the patterned and exposed PZT/Pt multilayer composite.

PZT Layer	Cap. Area (μm^2)	Cap. (nF)	Dielectric Const.
PZT 4	1.51×10^5	5.6	1071
PZT 3	2.31×10^5	11.7	1423
PZT 2	3.32×10^5	12.5	1029
PZT 1	4.53×10^5	14.3	822

Table 12. Capacitor areas and dielectric properties at 0V as a function of PZT layer.

Shown in Figure 72, individual capacitors within the multilayer stack were electrically active. It should be noted that overall yield for these capacitors was limited to 20% - 25% of the devices due to fabrication related defects, electrical shorting between electrode layers and inadvertent high electric field application during initial testing. These issues will be addressed in future research. It has been reported that during the fabrication of multilayer capacitors pinhole defects in the PZT and small electrode areas lead to electrical shorts in between the different electrode layers [98]. Individual layer capacitance values at 0V varied between 6 and 14 nF with the corresponding relative dielectric constants varying between 822 and 1423. The variability in relative dielectric constant observed in the individual layers can possibly be attributed to the changes in texture between the layers based on the observations of dielectric properties versus texture (see section 5.2) . Additional analysis on the individual layer variances will be continued in future work.

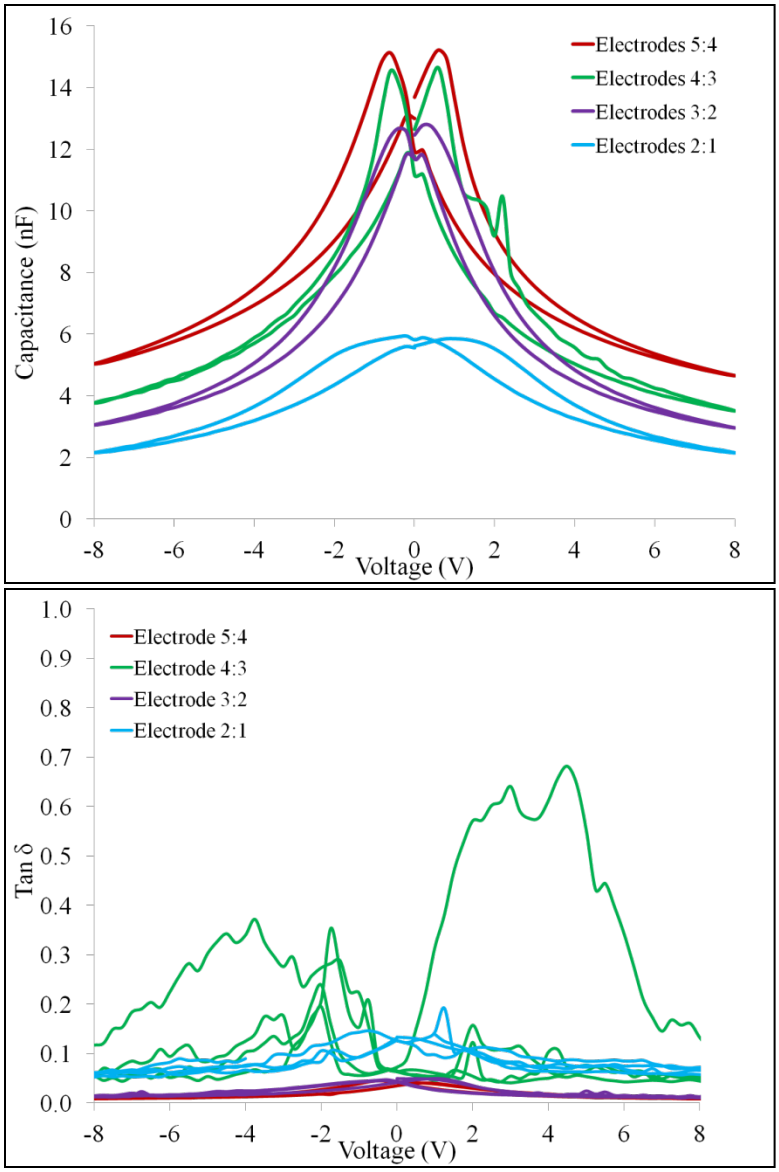

Figure 73. Capacitance and tan δ as a function of voltage for the individual PZT layers in a multilayer device.

In addition to testing individual PZT layers, alternating electrodes were connected to create a parallel connection with the capacitors (Figure 74). In this configuration, Pt layers 2 and 4 and Pt layers 1, 3, and 5 were electrically coupled, respectively. Using the HP 4192A LCR impedance analyzer a capacitance versus voltage sweep was performed twice, the first measurement looked at electrically

grounded Pt layers 2 and 4 while the second measurement electrically grounded Pt layers 1, 3, and 5. At 0 V the device capacitance areal density was $3.77x10^3$ nF/cm^2. This corresponds to the summation of the individual capacitance, 44.1 nF, of each of the 4 layers summarized in Table 11 at 0 V.

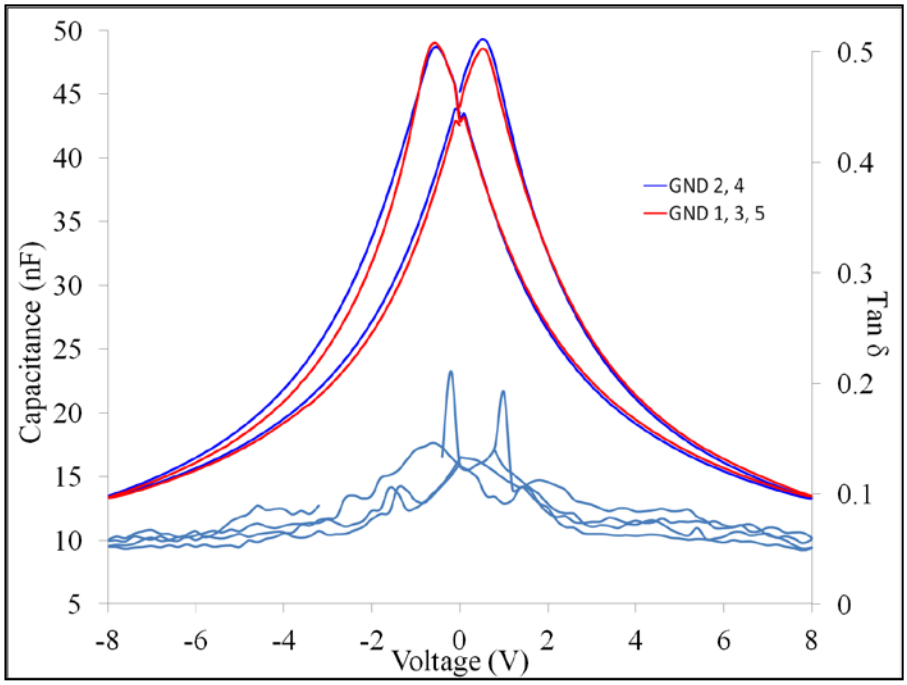

Figure 74. Capacitance as a function of voltage for the multilayer device connected in parallel.

6.2.3 Comparing a 4-Layer Stack to Other Comparable Stacks

A second set of samples was prepared to evaluate the piezoelectric induced deformation in cantilevers. For this set of experiments, three wafers were fabricated with a total PZT thickness target of one micron with a single layer, two 500nm layers, or four 250 nm layers of PZT as depicted in Figure 75. Similar to the earlier samples, XRD measurements were performed after each Pt deposition. Unfortunately, technical problems with RTA temperature ramp rate limited this new set of wafers to

a ramp rate of ~40º C/sec instead of the optimized ~199º C/sec. The issues with the RTA led to reduced [001] orientations in the films, particularly noticeable in layer 2 of the 2-layer stack and layers 3 and 4 in the 4-layer stack as observed in the {100} Lotgering factors (Figure 76).

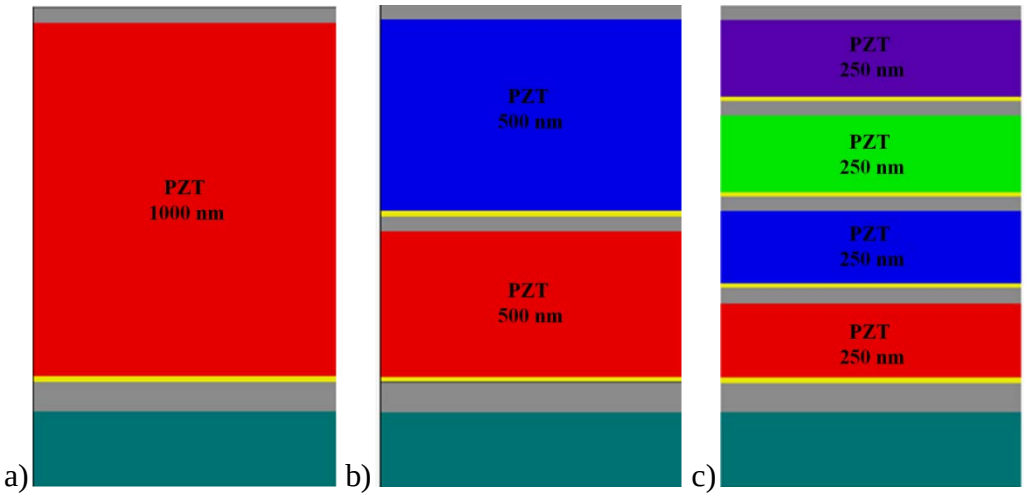

Figure 75. Schematic of the PZT multilayer stacks of a) 1 layer - 1000nm thick PZT b) 2 layers - 500nm thick PZT each c) 4 layers - 250nm thick PZT each

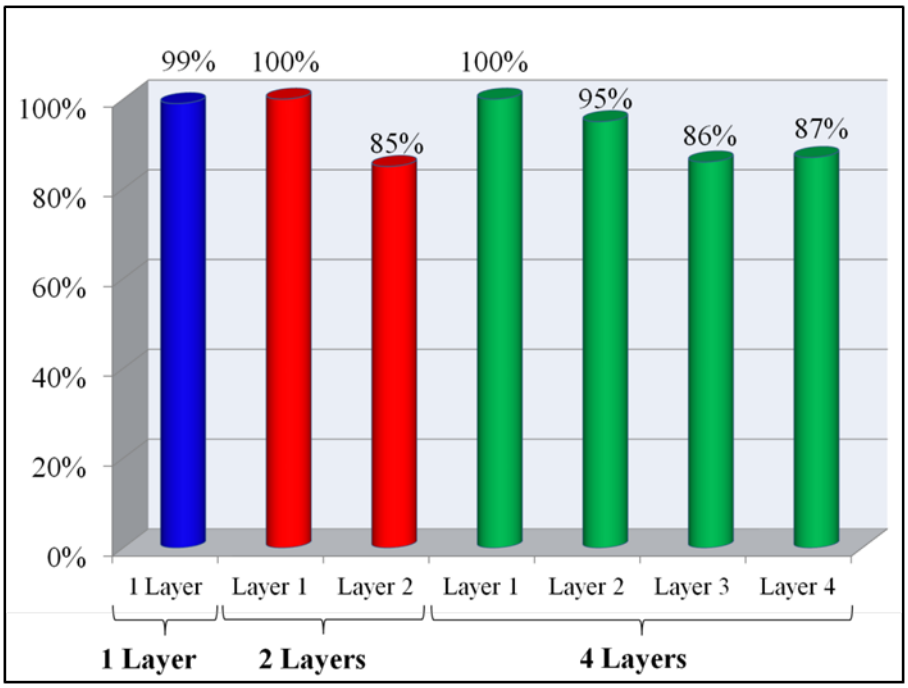

Figure 76. The Lotgering factor for the (001)/(100) orientations for each of the stacks described in Figure 75.

The cantilever devices followed the same fabrication procedure outlined in Figure 69 with the addition of a reactive ion etch of the 500nm SiO_2 elastic layer to expose the Si substrate to a XeF_2 release etch at the end of processing to release the cantilevers (Figure 78). Ferroelectric data for the films connected in parallel was characterized with a Radiant Technologies Precision Ferroelectric Tester from -10 V to 10 V (Figure 77). Both the 1 layer and 2 layer films exhibit hysteresis loop asymmetry and pinching. The 4 layer sample exhibits higher polarization values for the same voltages, but a higher applied electric field since the films were thinner, with no pinching observed potentially due to fewer defects in the thinner PZT layers.

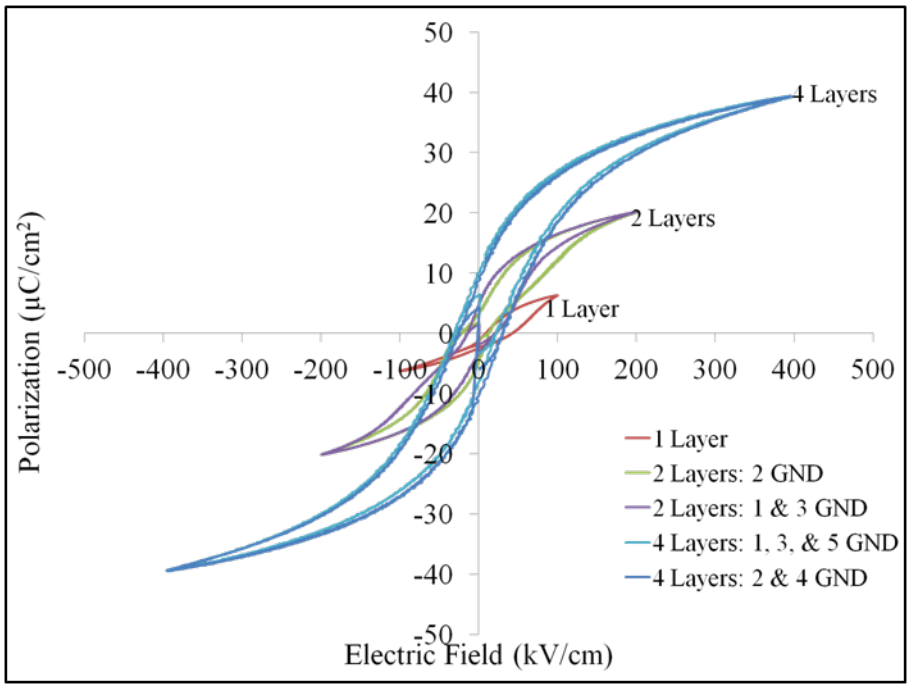

Figure 77. PE - Hysteresis data for 1 layer, 2 layer, and 4 layer capacitors connected in parallel.

A Polytec MSV Laser Doppler Vibrometer (LDV) system was used for non-contact displacement measurements using a frequency of 2 Hz and a poling voltage of 10V. Displacement data presented in Figure 79 shows piezoelectric induced displacement using both positive and negative unipolar drive sweeps from -5 V to 0 V and +5 V to 0 V for the 1-layer stack, the 2-layer stack, and PZT layers 1 and 2 in the 4-layer stack of a cantilever with a length of 180 microns. Similar to the data presented earlier, LDV data was limited to the smaller length cantilevers as a result of the large positive residual stress induced curvature in the cantilevers. The same data is presented as a function of electric field in Figure 80. The thinner multilayer films exhibited greater displacements due to higher applied fields across the film. Ultimately this would allow lower applied voltages to achieve similar displacements to single layer thicker films.

a)

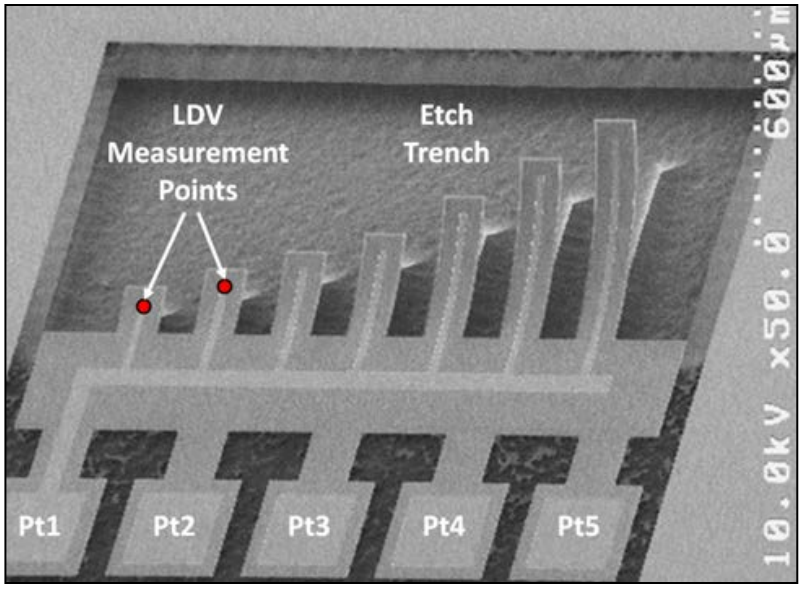

b)

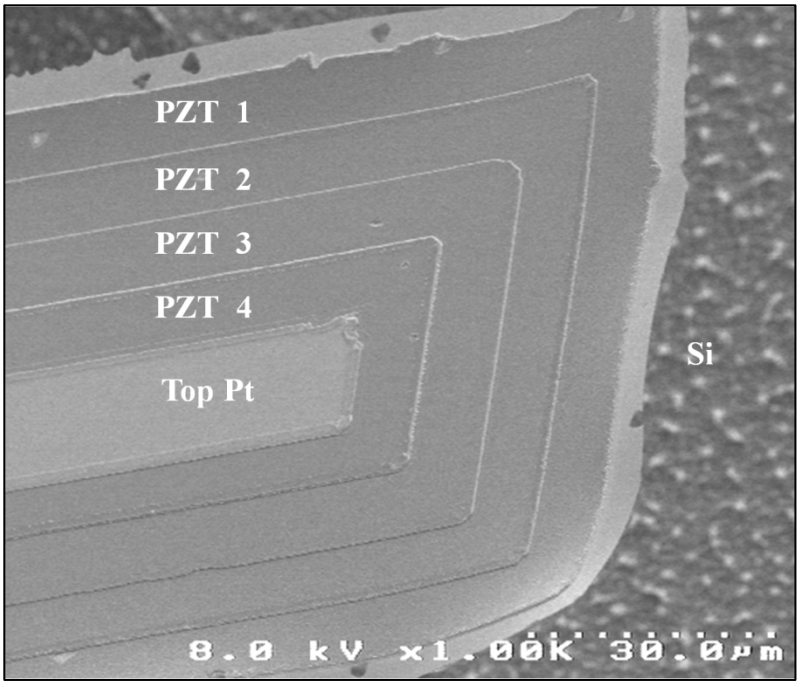

Figure 78. SEM images of a) released cantilever arrays and b) a cantilever beam showing the 4-layer multilayer stack.

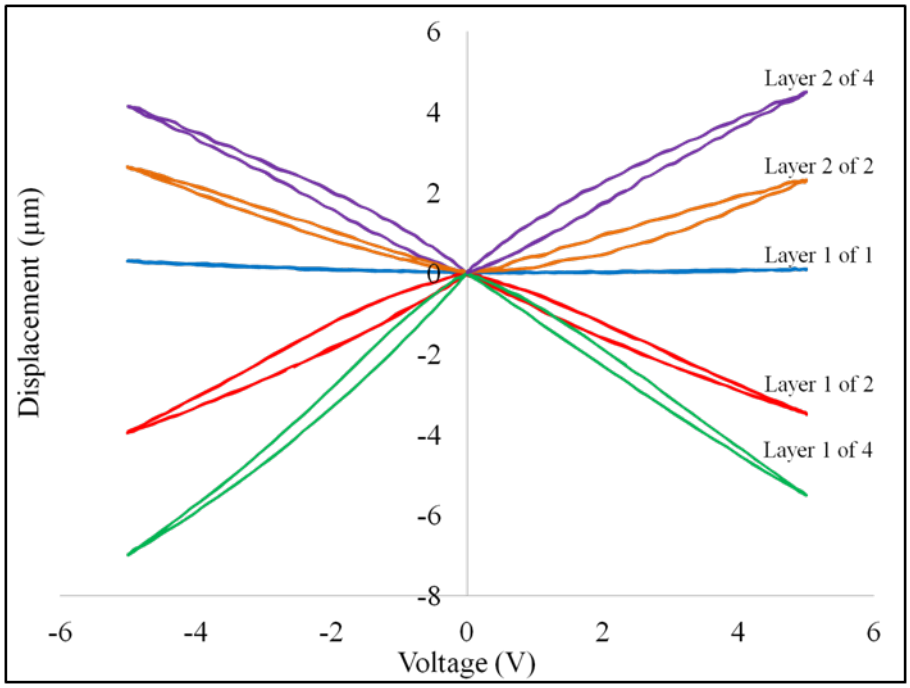

Figure 79. Unipolar displacement curves of the different layers in the multilayer capacitors from - 5 V to 0 V and from +5 V to 0 V.

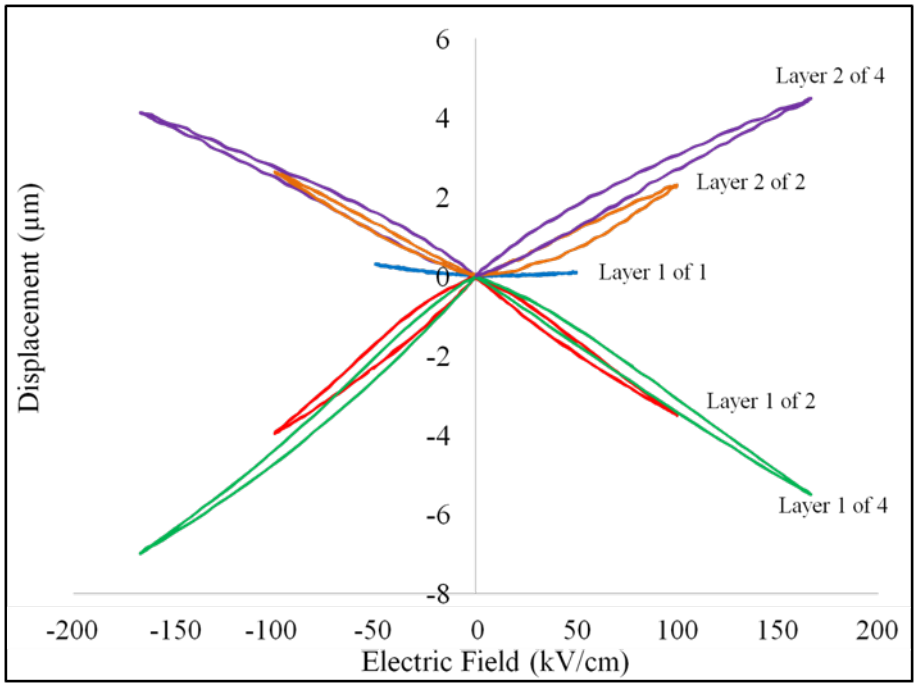

Figure 80. Unipolar displacement curves of the different layers in the multilayer capacitors as a function of the electric field.

Upon initial examination of the displacement, the choice of the elastic layer thickness and the location of the neutral axis of the cantilevers determine the displacement direction and amplitude for the different multilayer configurations (Figure 80). For the single layer case, the neutral axis resides roughly in the bottom third of the PZT layer (Figure 81a). As a result, the PZT section above and below the neutral axis effectively work against one other limiting the amplitude of the bending deflection. For the 2-layer case, the neutral axis resides just below the middle Pt electrode (Figure 81b). As a result, the cantilevers deform in the negative z-direction (into the wafer) when PZT layer 1 is actuated and deform in the positive z-direction (out of the wafer) when PZT layer 2 is actuated. Similarly for the 4-layer case, the neutral axis resides close to the Pt layer between PZT layer 1 and 2 (Figure 81c). As a result, the cantilevers deform in the negative direction when PZT layer 1 is actuated and positive direction when actuated with PZT layer 2, 3, or 4. Note, data for layers 3 and 4 of the 4-layer stack was unavailable due to both device yield and aforementioned inadvertent overdriving of these layers during testing.

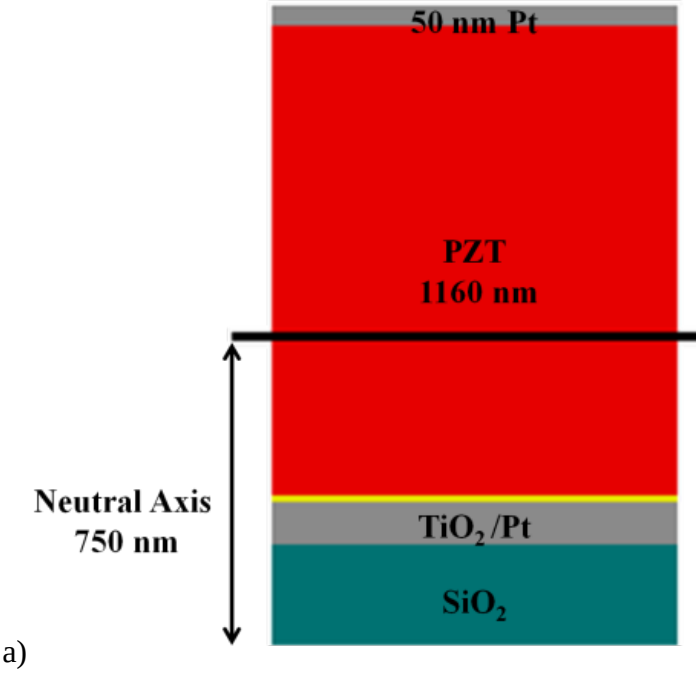
50 nm Pt
PZT
1160 nm
Neutral Axis
750 nm
TiO2/Pt
SiO2

a)

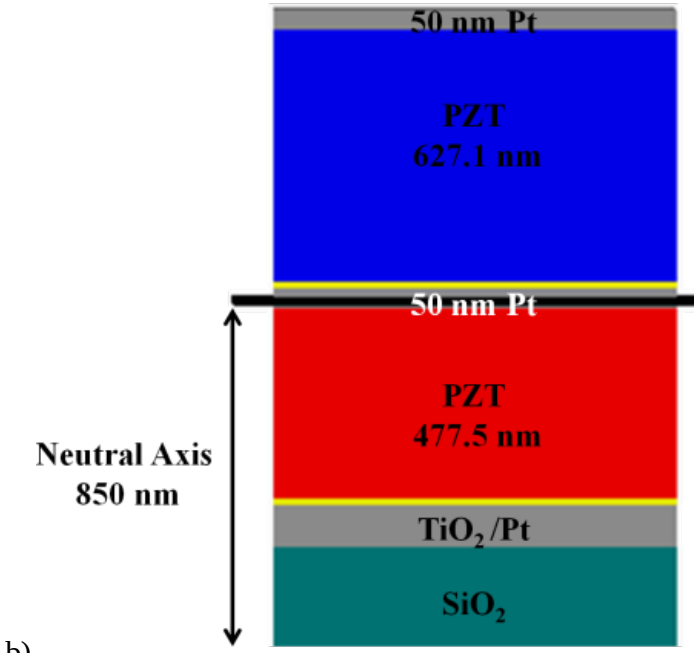
50 nm Pt
PZT
627.1 nm
50 nm Pt
PZT
477.5 nm
Neutral Axis
850 nm
TiO2/Pt
SiO2

b)

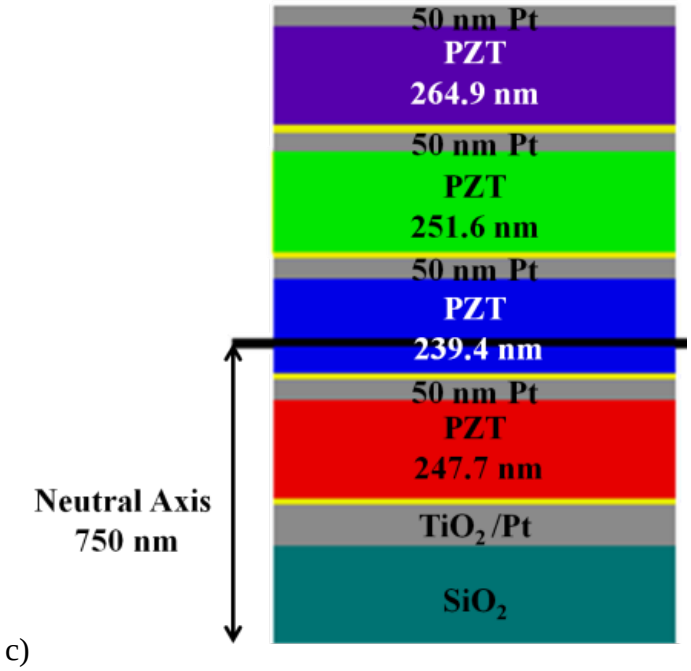

Figure 81. Schematic of the Pt/PZT/Pt multilayer stacks with the neutral axis drawn in position based off calculations from the stacks fabricated. Neutral axis locations were calculated by Gabriel Smith of the US Army Research Laboratory, Adelphi, MD. The neutral axis was located at (a) 750nm in the 1 layer stack (b) 850 nm in the 2 layer stack and (c) 750 nm in the 4 layer stack.

Cantilevers that can actuate at large electric fields with either positive or negative vertical displacements will allow for the creation of large bi-directional actuation in multi-layer actuators compared to vertical-direction unimorph actuators. Additionally, Figure 80 compares the displacement of the different multilayer configurations as a function of the electric field experienced by the different layer thicknesses. The results in Figure 80 illustrate how the multilayer actuators leverage higher electric field actuation using significantly lower voltages than a single layer of the same total thickness.

The first demonstration of bi-directional actuation in a unimorph actuator has been shown. The bi-directional actuation enables enhanced restoring force in MEMS switches by adding an active piezoelectric force rather than just relying entirely on the passive mechanical restoring force. Similarly, MEMS switches requiring small gaps between the cantilever and a contact electrode may benefit from bi-directional actuation as it can control the distance between the two instead of depending entirely on fabrication process controls.

Chapter 7: Moving Forward

7.1 Orientation Control in PZT (52/48)

The impact of obtaining highly (001) oriented morphotropic phase boundary PZT (52/48) has been reported to greatly improve the electrical properties of thin film PZT (52/48). Ultimately, improvements in orientation are stated to increase the piezoelectric, e_{31} coefficient which results in increased actuator displacements and reduced actuation voltages for the same values of a film that has not been optimized. Attempts have been made to produce (001) oriented chemical solution deposition sol-gel thin films PZT films and optimize their electrical and displacement characteristics through the use of $PbTiO_3$ (PTO) seed layers, annealing experiments and variations in the solution Pb-excess.

7.1.1 Summary of Results: Improving PZT (52/48) Texture through $PbTiO_3$ Seed Layers and Platinum Metallization

Initial experiments investigated the influence of a single layer ~20 nm PTO seed layer on the orientation of 500 nm PZT (52/48) thin films. The PTO seed layer was tested with the use of 7% acetic acid to compensate for Pb loss during high temperature annealing and without the acetic acid. The x-ray diffraction (XRD) data from films with the PTO seed layer showed (001) and (100) peak splitting with reductions in the (110) and (111) peak intensities when compared to the PZT (52/48) control sample without PTO. Films that used the acetic acid exhibited 10% higher dielectric constants (1299), 2% improvement maximum polarization (41 $\mu C/cm^2$) and

20% improvement in remanent polarization (15 $\mu C/cm^2$) from a control sample of PZT (52/48) without the PTO seed layer. Static displacement measurements of fabricated cantilevers taken with a Wyko optical profilometer at 10V showed an improvement of 40% in piezoelectric induced cantilever displacement in films using the PTO seed layer.

Leveraging the optimization research of colleagues on Pt electrodes lead to further improvements in (001) orientation in PZT (52/48). The bottom electrode was changed from a Ti/Pt electrode to a TiO_2/Pt electrode with a highly (111) Pt (FWHM ranging from 2 – 3 degrees). XRD measurements for Ti/Pt/PZT (52/48) films exhibited a {001} Lotgering factor of 59% while films with the Ti/Pt/PTO/PZT (52/48) stack had a (001) Lotgering factor of 87%. The TiO_2/Pt/PZT (52/48) stack resulted in a (001) Lotgering factor of 10% with the PZT nucleating predominantly as (111) matching the underlying Pt layer. The addition of the PTO seed layer on the TiO_2/Pt bottom electrode showed a (001) PZT Lotgering factor of 96% for films. Transmission electron microscopy (TEM) images of the 10% Pb-excess PZT (52/48) with the PTO seed layer showed the columnar PZT grains templating off the PTO which templated off the individual Pt grains.

7.1.2 Summary of Results: The Effects of Thermal Treatment and Lead Excess

Further refinements to the PZT process were examined through thermal treatment on the orientation and displacement characteristics of the PTO/PZT (52/48) films. A final crystallization temperature of 700°C was used in three different ramping conditions, a slow ramp (SR) of 4 °C/sec to 700 °C for 60 sec, a rapid ramp (RR) of 199 °C/sec to 700 °C for 60 sec, and a double ramp (DR) 199 °C/sec to 550

°C with a 2 minute hold followed by a second ramp of 199 °C/sec to 700 °C for 30 sec. Improvements in (001) and (100) orientations along with decreased (110) PZT orientation were observed in films with the RR and DR annealing processing. Preliminary tests on the influence of Pb-excess on PZT orientation were performed by using PZT (52/48) solutions with lead excess values of 8%, 10%, and 15%. 10% Pb-excess in the PZT (52/48) solutions exhibited the best {001} Lotgering factors of 99% for samples annealed under DR conditions and 98% for films annealed under RR conditions. While films with 15% Pb-excess PZT (52/48) also showed high percentages of (001) orientation, fabricated capacitor devices broke down upon the application of low voltages (< 2 V) corresponding to excess PbO in the grain boundaries. Static piezoelectric displacement measurements at 10 V for the 10% Pb-excess PZT (52/48) films showed improvements of 50% for films annealed at DR conditions and a 230% improvement for films annealed at RR conditions when compared to films with no PTO seed layer used. In summary, the stack with TiO_2/ Pt /30% Pb-excess PTO/ 10% Pb-excess PZT (52/48) films exhibited a 99% improvement in cantilever deflection when compared to films without the PTO seed layer.

7.1.3 Summary of Results: The Influence of Pb-Excess on Device Properties

A more intensive study on the effects of Pb-excess in the PTO and PZT (52/48) solutions was conducted. From earlier experiments it was determined that PZT (52/48) solutions with 15% Pb-excess would not yield electrically usefully films for MEMS devices. The Pb-excess was varied in the PTO seed layer solution: 0%, 10%, 15%, 20%, and 30% Pb-excess solutions. The Pb-excess in the PZT (52/48)

films were also varied: 0%, 3%, 5%, 8%, and 10%. XRD measurements showed that higher percentages of Pb-excess in the PTO seed layer solutions, 20% and in particular 30%, have the highest (001) orientation in the PZT (52/48) films. The PZT (52/48) with 30% Pb-excess PTO solution films showed significant reductions in (110) and (111) orientations compared to PTO solutions with the other Pb-excess percentages tested. In the electrical studies of the films, the percentage of Pb-excess in the PTO showed the greatest influence in polarization values and hysteresis widths, dielectric constants and tunability, leakage currents, and breakdown field. While variations in the Pb-excess of the PZT (52/48) solution were also observed, the Pb-excess in the PTO had the greatest influence in film properties. Most films with less than 30% Pb-excess in the PTO seed layer showed very small (222) and/or (400) pyrochlore phases. Minute amounts of the PbO deficient phase can result in reduced electrical properties. Pb and O vacancies in the perovskite unit cell will result in pinned domains and domain walls.

7.1.4 Future Work in Orientation Control of PZT (52/48)

While the impact of the Pb-excess in the PTO seed layer has been described, further research is required to gain better understanding of how the electrical properties are influenced by the Pb-excess in the sol-gel solutions. In this study, the hysteresis measurements performed do not show saturated hysteresis due to a limit of +/- 19V. In addition, while polarization hysteresis loops provide important information about the PZT films, leakage currents in the film may influence hysteresis shape and provide higher remanent polarization values than what is true of the material. Future work consists of performing positive up negative down (PUND)

measurements (Figure 82a) from 0 V – 200 V to avoid these problems and separate ferroelectric switching from artifacts. The PUND measurement involves an initializing pulse, labeled as the “set” pulse in Figure 82a, which is the equivalent to a first loop in hysteresis measurements that is performed prior to the actual measured loop to set the material in a definite polarization state. The second pulse, P, in the PUND measurement switches the film polarization in the direction of the applied field. When comparing this to a hysteresis loop (Figure 82b) point 1 and 2 in Figure 82a corresponds to the polarization value between the negative remanent polarization to the maximum positive polarization. Between points 2 and 3 the film polarization back switches to the positive remanent polarization state. After a pre-established pulse delay time, which is determined as a function of the films relaxation or back switching time, a third pulse, U, in the same direction and magnitude as a the P pulse is applied. The U pulse is the non-switching polarization as it is the change in polarization between the positive remanent polarization, point 3 in Figure 82b and the films return to the positive maximum polarization, point 4 in Figure 82b. After the U pulse, a fourth pulse in the negative direction, N, is applied, switching the internal polarization and resulting in a polarization value which is equivalent to the positive remanent polarization to the negative maximum polarization. A set pulse is not required since the polarization has already been set previously. Finally, a fifth pulse is applied, D, which measures the polarization values between the negative remanent polarization and the internal polarizations return to the negative maximum polarization.

a)

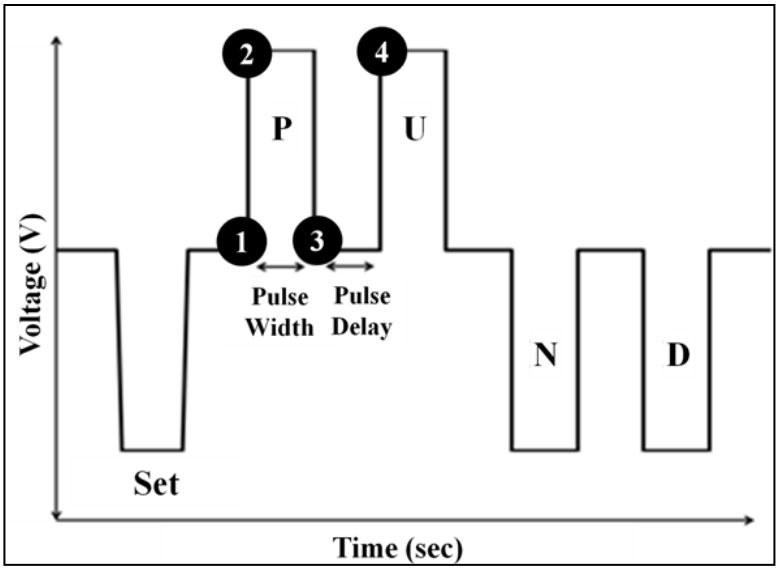

b)

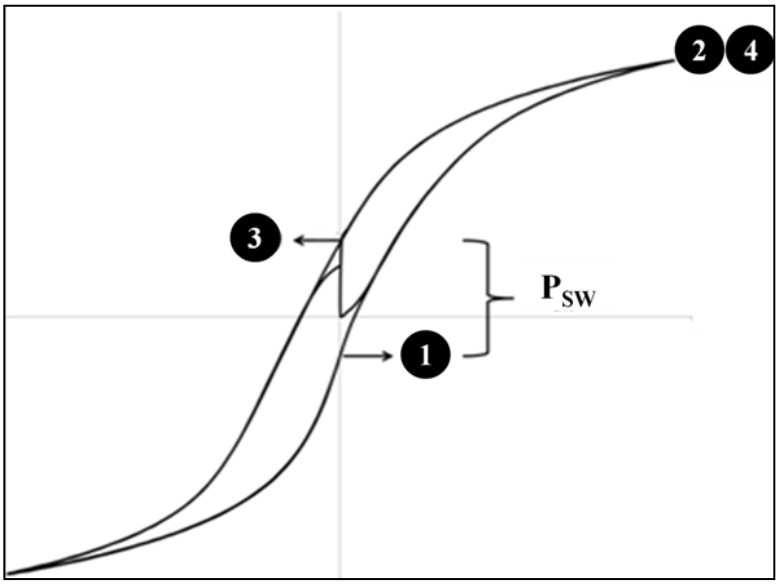

Figure 82. Schematic of the a) PUND measurement pulses and b) how the pulses relate to a typical polarization hysteresis loop.

In a full test sweep, after the first PUND measurements have been preformed, the voltage is increased and another PUND measurement is preformed (Figure 83a). This process continues until the measurement has reached the desired maximum voltage or film breakdown voltage. The results from the full sweep will provide the true maximum polarization of the film at a saturation voltage (Figure 83b) in both the positive, P_{sw}, and negative, N_{sw}, directions. The switchable polarization, Q_{sw}, is determined by subtracting P_{sw} from N_{sw} and dividing by 2.

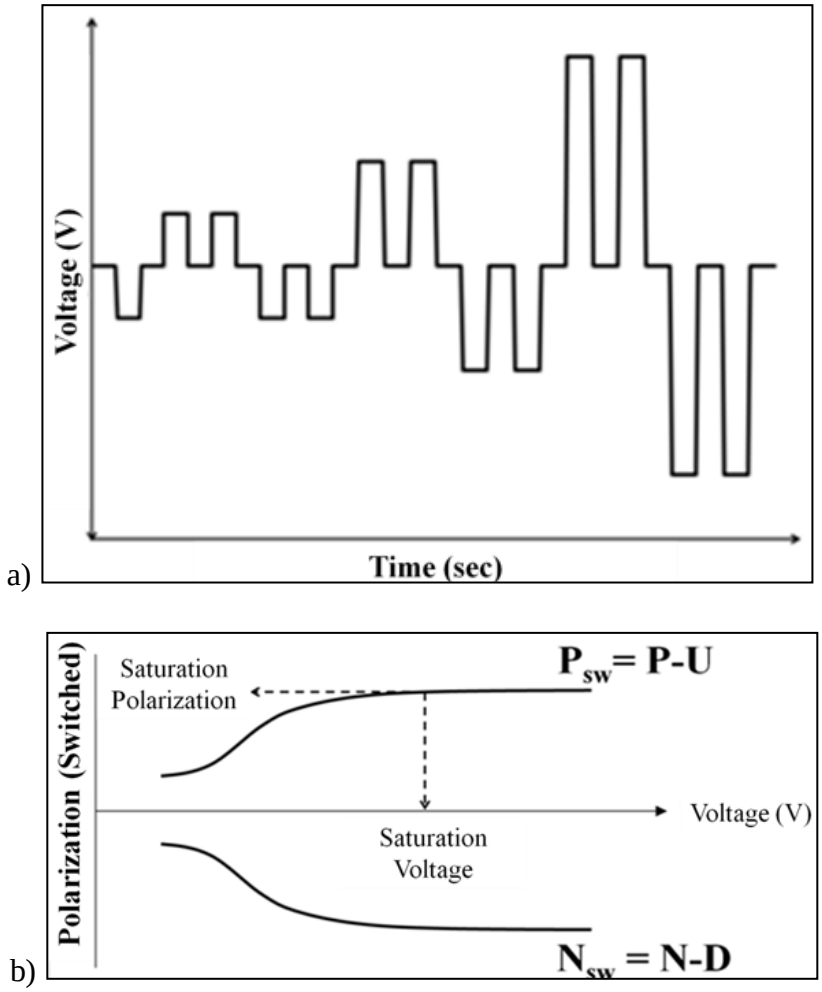

Figure 83. Schematic of a) a PUND measurement sweep at different voltages and b) the results of a PUND sweep at increasing voltages.

Performing this test on the Pb-excess samples will provide a wealth of knowledge on the true polarization characteristics of the film and how differences in the hysteresis shape, tilt, and imprint of the different samples ultimately contribute to the electrical properties of the PZT films. The PUND measurements can also highlight greater differences between the films from the Pb-excess study and determine the films retention capabilities, which is a measure of the films ability to hold its polarization before back switching.

In addition to further expanding our knowledge on the effects of the Pb-excess on the electrical properties of PZT (52/48) films, more research on the influence of pyrolysis and annealing ramps and temperature are needed. While several research groups have reported improved dielectric and polarization properties at the MPB of highly (001) oriented films, this research has not observed such extreme improvements. This may be due to a high defect density within the films which pin domains. Preisach measurements would enable the study of the reversible and irreversible contributions in a hysteresis measurement. Performing a Preisach measurement on a series of samples with varying pyrolysis and annealing ramps and temperatures would provide further insight into the defect formation process and how to reduce the occurrences.

Processing conditions and stress may also shift the morphotropic phase boundary. If a shift in the MPB occurred, then the improved dielectric and piezoelectric properties that were expected in the films would not be observed. Future tests would require analyzing PZT films with Zr/Ti compositions around (52/48) to determine the region of optimal performance when using a 30% Pb-excess PTO seed

layer. This experiment will ensure the use of high performance PTO/PZT films at the MPB.

7.2 Multilayered PZT Devices

Several groups have reported the fabrication of multilayer PZT devices with alternating Pt/PZT/Pt layers. Using a multilayer PZT device allows for lowered operating voltages and more importantly greater contact forces in switches. In addition to fabricating multilayer capacitors and actuators in this study, (001) oriented PZT was used to achieve better performance from these devices.

The results presented showed the ability to maintain greater than 90% (001) orientation across the entire 4 layer Pt/PZT/Pt stack when using a single layer ~17nm thick 30% Pb-excess PTO seed layer between every Pt/PZT layer compared to 56% when using the seed layer in only the first Pt/PZT layer. Using the 5 ion-mill etch procedure to expose each Pt layer in the stack, capacitors and cantilever devices were fabricated. Initial testing showed the ability to measure the capacitance of the devices in the individual Pt/PTO/PZT/Pt layers as well as connecting every other layer together to measure the layers in parallel connections.

In a subsequent experiment, a 4 layer 0.25 μm PZT multilayer device was fabricated to compare with a 2 –layer multilayer 0.5 μm PZT device and a single layer 1 μm PZT stack. Problems with ramp rates in the rapid thermal annealing (RTA) equipment led to reduced (001) orientation intensities of the films but still greater than the films that did not use the PTO seed layer between every Pt/PZT layer. There were also yield problems in this set of devices that affected the top 2 layers of the 4-layer PZT cantilevers which did not allow displacement measurements of these

2 layers. Unipolar driven piezoelectric induced displacement measurements performed from -5 V to 0 V and from 5 V to 0 V, showed 45x greater displacements observed in the bottom 2 layers of the 4 layer devices when compared to a single layer 1 µm PZT stack and 2x greater displacement when compared to a 2 layer 0.5 µm stack. The 2 layer stack showed 23x greater displacement than the 1 layer stack. Ultimately the greater displacements observed were a function of greater applied fields across the individual films due to the thickness differences in the PZT film, it still paves a way to fabricate devices that require lower operating voltages to achieve the same displacement metrics as a single layer film. The selected elastic layer for the multilayer PZT experiments resulted in the neutral axis of a cantilever beam being uniquely located in three different locations for the 3 different multilayer composites.

Future work involves optimizing a unique fabrication process to minimize the number of ion-mills required for device fabrication. This will significantly reduce the time, masks, and fabrication steps required to process devices as well as lessen the damage to the PZT films that will influence the electrical performance. Additional electrical testing is required in all 4 layers of the 4 layer PZT stack to gain further insight on control of cantilever deflection in these devices. Further electrical studies will also be performed such as capacitance, leakage, breakdown, and PUND of the individual PZT layers as well as the devices connected in parallel.

Chapter 7: Publication Summary

7.1 Poster Presentation

- *Optimization of $PbTiO_3$ Seed Layers for PZT MEMS Actuators*
  - 2008 ARL Summer Student Symposium

- *PZT Optimization by High Temperature Post Fabrication Recovery Anneals*
  - 2009 ARL Summer Student Symposium

- *Improving PZT Thin Film Texture through Improved Platinum Metallization and Seed Layers*
  - 2009 U.S. Navy Workshop on Acoustic Transduction Materials and Devices
  - 2010 U.S. Navy Workshop on Acoustic Transduction Materials and Devices
  - 2010 Materials Research Society (MRS Fall Meeting)
  - 2011 Materials Science & Technology (MS&T)

- *Effects of Pb-Excess in PZT (52/48) Thin Films for Use in Multilayer Actuators*
  - 2013 ARL Summer Student Symposium
  - 2013U.S. Navy Workshop on Acoustic Transduction Materials and Devices
  - 2013 US-Japan Seminar on Dielectric and Piezoelectric Materials

- *Orientation Control in PZT (52/48) Thin Films for Use in Multilayer Actuators*
  - 2012 ARL Summer Student Symposium
  - 2012 U.S. Navy Workshop on Acoustic Transduction Materials and Devices

7.2 Oral Presentations

- *Improving PZT Thin Film Texture through Improved Platinum Metallization and Seed Layers*
    - 2011 U.S. Navy Workshop on Acoustic Transduction Materials and Devices
    - 2011 International Workshop on Piezoelectric Materials and Applications (IWPMA)
    - 2011 International Symposium on Applications of Ferroelectrics (ISAF)

- *Effects of Pb-Excess in PZT (52/48) Thin Films for Use in Multilayer Actuators*
    - 2013 Electronic Materials and Applications (EMA)
    - 2013 U.S. Navy Workshop on Acoustic Transduction Materials and Devices

- *Orientation Control in PZT (52/48) Thin Films for Use in Multilayer Actuators*
    - 2012 Electronic Materials and Applications (EMA)
    - 2012 U.S. Navy Workshop on Acoustic Transduction Materials and Devices
    - 2012 ARL Summer Student Symposia
    - 2012 Materials Research Society (MRS Fall Meeting)

7.3 Publications and Patents

- *Luz M Sanchez* and Ronald G Polcawich, "Optimization of PbTiO3 Seed Layers for PZT MEMS Actuators," Army Research Laboratory, Adelphi, TR 4697, 2008

- Daniel M. Potrepka, Glen. R. Fox, *Luz M. Sanchez*, and Ronald G. Polcawich, "Pt/TiO2 Growth Templates for Enhanced PZT films and MEMS Devices," *MRS Online Proceedings Library*, vol. 1299, no. 1, 2011.

- *Luz M. Sanchez*, Daniel M. Potrepka, Glen R. Fox, Ichiro Takeuchi, and Ronald G. Polcawich, "Improving PZT Thin Film Texture Through Pt Metallization and Seed Layers," *MRS Online Proceedings Library*, vol. 1299, no. 1, 2011.

- Daniel M. Potrepka, *Luz M. Sanchez*, and Ronald G. Polcawich, "Atomic layer deposition of Pt growth template for orienting PbZrxTi1-xO3 thin films," *Journal of Vacuum Science Technology A: Vacuum, Surfaces, and Films*, vol. 30, no. 1, pp. 01A129 –01A129–7, 2012.

- Gabriel L. Smith, Jeffrey S. Pulskamp, *Luz M. Sanchez*, Daniel M. Potrepka, Robert M. Proie, Tony G. Ivanov, Ryan Q. Rudy, William D. Nothwang, Sarah S. Bedair, Christopher D. Meyer, and Ronald G. Polcawich, "PZT-Based Piezoelectric MEMS Technology," *Journal of the American Ceramic Society*, vol. 95, no. 6, pp. 1777–1792, 2012.

- *Luz M. Sanchez*, Daniel M. Potrepka, Glen R. Fox, Ke Wang, Leonid Bendersky, Ichiro Takeuchi, Ronald G. Polcawich, "Optimization of PbTiO3 Seed Layers and Pt Metallization for PZT Based PiezoMEMS Actuators" *Journal of Materials Research*, vol. 28, no. 14, pp 1920-1931, 2013.

- *Luz M. Sanchez*, Alden Grobicki, Gabriel Smith, Jeffrey Pulskamp, Ichiro Takeuchi, Ronald G. Polcawich, "Texture Control in Lead Zirconate Titanate Multi-layer Thin Films" *Transactions on Ultrasonics, Ferroelectrics, and Frequency Control IEEE*. - ACCEPTED

Bibliography

[1] N. Yazdi, A. Salian, and K. Najafi, "A high sensitivity capacitive microaccelerometer with a folded-electrode structure," in *Twelfth IEEE International Conference on Micro Electro Mechanical Systems, 1999. MEMS '99*, 1999, pp. 600–605.

[2] H. Emmerich and M. Schofthaler, "Magnetic field measurements with a novel surface micromachined magnetic-field sensor," *IEEE Trans. Electron Devices*, vol. 47, no. 5, pp. 972–977, 2000.

[3] Y. Rosen and N. Elman, *Biomaterials Science: An Integrated Clinical and Engineering Approach*. CRC Press, 2012.

[4] L. E. Larson, "Microwave MEMS technology for next-generation wireless communications," in *Microwave Symposium Digest, 1999 IEEE MTT-S International*, 1999, vol. 3, pp. 1073–1076 vol.3.

[5] S. Leroy, "Top 30 MEMS Companies 2010." Yole Developpment, 2011.

[6] R. G. Ballas, *Piezoelectric Multilayer Beam Bending Actuators: Static and Dynamic Behavior and Aspects of Sensor Integration*. Springer, 2007.

[7] S. B. Lang, "Pyroelectricity: From Ancient Curiosity to Modern Imaging Tool," *Phys. Today*, vol. 58, no. 8, pp. 31–36, 2005.

[8] J. Curie and P. Curie, "Développement, par pression, de l'électricité polaire dans les cristaux hémièdres à faces inclinées.," *Comptes Rendus*, vol. 91, pp. 291–295, 1880.

[9] R. F. Mould, "Pierre Curie, 1859-1906," *Curr. Oncol.*, vol. 14, no. 2, pp. 74–82, Apr. 2007.

[10] S. Katzir, *The Beginnings of Piezoelectricity: A Study in Mundane Physics*. Springer, 2007.

[11] R. Arshadi and R. S. C. Cobbold, "A pioneer in the development of modern ultrasound: Robert William Boyle (1883–1955)," *Ultrasound Med. Biol.*, vol. 33, no. 1, pp. 3–14, Jan. 2007.

[12] R. S. Dahiya and M. Valle, *Robotic Tactile Sensing: Technologies and System*. Springer, 2012.

[13] H. De and H. De, "Electric Ignition System," 224857408-Jul-1941.

[14] T. J. Pope and T. J. Pope, "Compressional Wave Translating," 240560413-Aug-1946.

[15] C. Paslay and C. Paslay, "Method and Means for Surveying," 246569629-Mar-1949.

[16] A. L. W. Wilhams, "Piezoelectric Device," 222205619-Nov-1940.

[17] W. J. Brown and W. J. Brown, "Piezoelectric Motor," 243949913-Apr-1948.

[18] C. A. Bieling and C. A. Bieling, "Piezoelectric Device," 212322712-Jul-1938.

[19] R. W. T. Camden and R. W. T. Camden, "Piezoelectric Device," 247217907-Jun-1949.

[20] B. S. T. Journal, "Piezoelectric Transducer," 232847831-Aug-1943.

[21] S. Teslic, T. Egami, and D. Viehland, "Local atomic structure of PZT and PLZT studied by pulsed neutron scattering," *J. Phys. Chem. Solids*, vol. 57, no. 10, pp. 1537–1543, Oct. 1996.

[22] M. J. Haun, E. Furman, T. R. Halemane, and L. E. Cross, “Thermodynamic theory of the lead zirconate-titanate solid solution system, part IV: Tilting of the oxygen octahedra,” *Ferroelectrics*, vol. 99, no. 1, pp. 55–62, 1989.
[23] M. E. Lines and A. M. Glass, *Principles and Applications of Ferroelectrics and Related Materials*. Oxford New York: Oxford University Press, 2004.
[24] A. K. Tagantsev, M. Landivar, E. Colla, and N. Setter, “Identification of passive layer in ferroelectric thin films from their switching parameters,” *J. Appl. Phys.*, vol. 78, no. 4, pp. 2623–2630, 1995.
[25] A. M. Bratkovsky and A. P. Levanyuk, “Very large dielectric response of thin ferroelectric films with the dead layers,” *Phys. Rev. B*, vol. 63, no. 13, p. 132103, Mar. 2001.
[26] D. Damjanovic, “Hysteresis in Piezoelectric and Ferroelectric Materials,” *Sci. Hysteresis 3*, pp. 337–465, 2005.
[27] R.-A. Eichel, “Defect structure of oxide ferroelectrics—valence state, site of incorporation, mechanisms of charge compensation and internal bias fields,” *J. Electroceramics*, vol. 19, no. 1, pp. 11–23, Sep. 2007.
[28] U. Robels and G. Arlt, “Domain wall clamping in ferroelectrics by orientation of defects,” *J. Appl. Phys.*, vol. 73, no. 7, pp. 3454–3460, 1993.
[29] W. L. Warren, D. Dimos, G. E. Pike, K. Vanheusden, and R. Ramesh, “Alignment of defect dipoles in polycrystalline ferroelectrics,” *Appl. Phys. Lett.*, vol. 67, no. 12, pp. 1689–1691, 1995.
[30] D. C. Lupascu, Y. A. Genenko, and N. Balke, “Aging in Ferroelectrics,” *J. Am. Ceram. Soc.*, vol. 89, no. 1, pp. 224–229, 2006.
[31] J. Weertman and J. R. Weertman, *Elementary Dislocation Theory*. Oxford New York: Oxford University Press, 1992.
[32] S. Trolier-McKinstry and P. Muralt, “Thin Film Piezoelectrics for MEMS,” *J. Electroceramics*, vol. 12, no. 1–2, pp. 7–17, Jan. 2004.
[33] D.-M. Chun, M. Sato, and I. Kanno, “Precise measurement of the transverse piezoelectric coefficient for thin films on anisotropic substrate,” *J. Appl. Phys.*, vol. 113, pp. 1–9, 2013.
[34] L. E. Barton, “Method of Making Lead Pigments,” 241924622-Apr-1947.
[35] S. Roberts, “Dielectric Properties of Lead Zirconate and Barium-Lead Zirconate,” *J. Am. Ceram. Soc.*, vol. 33, no. 2, pp. 63–66, 1950.
[36] G. Shirane, E. Sawaguchi, and Y. Takagi, “Dielectric Properties of Lead Zirconate,” *Phys. Rev.*, vol. 84, no. 3, pp. 476–481, Nov. 1951.
[37] S. Cole and H. Espenschied, “Lead Titanate: Crystal Structure, Temperature of Formation, and Specific Gravity Data,” *J. Phys. Chem.*, vol. 41, no. 3, pp. 445–451, 1937.
[38] G. Busch and P. Scherrer, “Eine neue seignette-elektrische Substanz,” *Naturwissenschaften*, vol. 23, no. 43, p. 737.
[39] E. Wainer and A. Salomon, “High Dielectric Constant Ceramics,” 2,377,910,1945.
[40] G. Shirane and A. Takeda, “Phase Transitions in SOlid Solutions of PbZrO3 and PbTiO3 (I) Small Concentrations of PbTiO3,” *J. Phys. Soc. Jpn.*, vol. 7, no. 1, pp. 5–11, 1952.

[41] G. Shirane, K. Suzuki, and A. Takeda, “Phase Transition in Solid Solutions of PbZrO3 and PbTiO3 (II) X-Ray Study,” *J. Phys. Soc. Jpn.*, vol. 7, no. 1, pp. 12–18, 1952.
[42] B. Jaffe, R. S. Roth, and S. Marzullo, “Piezoelectric Properties of Lead Zirconate-Lead Titanate Solid-Solution Ceramics,” *J. Appl. Phys.*, vol. 25, no. 6, pp. 809–810, Jun. 1954.
[43] T. Ikeda, “Studies on (Ba-Pb)(Ti-Zr)O3 System,” *J. Phys. Soc. Jpn.*, vol. 14, pp. 168–174, 1959.
[44] B. Jaffe, W. R. Cook, and H. Jaffe, *Piezoelectric Ceramics*. London: Academic Press, 1971.
[45] D. I. Woodward, J. Knudsen, and I. M. Reaney, “Review of Crystal and Domain Structures in the PZT Solid Solution,” *Phys. Rev. B*, vol. 72, no. 10, pp. 1–7, 2005.
[46] B. Noheda, D. E. Cox, G. Shirane, J. A. Gonzalo, L. E. Cross, and S.-E. Park, “A Monoclinic Ferroelectric Phase in the PZT Solid Solution,” *Appl. Phys. Lett.*, vol. 74, no. 14, pp. 2059–2062, 1999.
[47] W. Cao and L. E. Cross, “Theorectical Model for the Morphotropic Phase Boundary in LEad Zirconate-Lead Titanate Solid Solution,” *Phys. Rev. B*, vol. 47, no. 9, pp. 4825–4830, 1993.
[48] Y. Shindo and F. Narita, “Piezomechanics in PZT Stack Actuators for Cryogenic Fuel Injectors,” in *Smart Actuation and Sensing Systems - Recent Advances and Future Challenges*, G. Berselli, Ed. 2012.
[49] K. D. Budd, S. K. Dey, and D. A. Payne, “Sol-Gel Processing of PbTi03, PbZr03, PZT, and PLZT Thin Films,” *Br. Ceram. Proc.*, vol. 36, pp. 107–121, 1985.
[50] S. K. Dey, K. D. Budd, and D. A. Payne, “Thin-Film Ferroelectrics of PZT by Sol-Gel Processing,” *IEEE Trans. Ultrason. Ferroelectr. Freq. Control*, vol. 35, no. 1, pp. 80–81, 1987.
[51] M. Aratani, K. Nagashima, and H. Funakubo, “Preparation of Pb(Zr $_{x}$, Ti $_{1-x}$)O $_{3}$ Thin Films by Source Gas Pulse-Introduced Metalorganic Chemical Vapor Deposition,” *Jpn. J. Appl. Phys.*, vol. 40, no. Part 1, No. 6A, pp. 4126–4130, Jun. 2001.
[52] H. Fujisawa, M. Shimizu, T. Horiuchi, T. Shiosaki, and K. Matsushige, “Investigation of the current path of Pb(Zr,Ti)O3 thin films using an atomic force microscope with simultaneous current measurement,” *Appl. Phys. Lett.*, vol. 71, no. 3, p. 416, Jul. 1997.
[53] K. Nagashima and H. Funakubo, “Composition Control of Pb(Zr$_\mbix$Ti$_**1**\mbi-x$)O$_**3**$ Thin Films Prepared by Metalorganic Chemical Vapor Deposition,” *Jpn. J. Appl. Phys.*, vol. 39, no. Part 1, No. 1, pp. 212–216, 2000.
[54] R. Frunza, D. Ricinschi, F. Gheorghiu, R. Apetrei, D. Luca, L. Mitoseriu, and M. Okuyama, “Preparation and characterisation of PZT films by RF-magnetron sputtering,” *J. Alloys Compd.*, vol. 509, no. 21, pp. 6242–6246, May 2011.
[55] X. Li, J. Liu, Y. Zeng, and J. Liang, “Low-temperature in situ preparation of ferroelectric Pb(Zr0.55Ti0.45)O3 thin films by reactive sputtering,” *Appl. Phys. Lett.*, vol. 63, no. 17, p. 2345, Oct. 1993.

[56] G. Velu and D. Remiens, “In situ deposition of sputtered PZT films: control of the growth temperature by the sputtered lead flux,” *Vacuum*, vol. 56, no. 3, pp. 199–204, Mar. 2000.
[57] P. Muralt, “PZT thin films for microsensors and actuators: Where do we stand?,” *IEEE Trans. Ultrason. Ferroelectr. Freq. Control*, vol. 47, no. 4, pp. 903–915, 2000.
[58] Y. Sakashita, T. Ono, H. Segawa, K. Tominaga, and M. Okada, “Preparation and electrical properties of MOCVD #x2010;deposited PZT thin films,” *J. Appl. Phys.*, vol. 69, no. 12, pp. 8352–8357, 1991.
[59] I. M. Reaney, D. V. Taylor, and K. G. Brooks, “Ferroelectric PZT Thin Films by Sol-Gel Deposition,” *J. Sol-Gel Sci. Technol.*, vol. 13, no. 1–3, pp. 813–820, Jan. 1998.
[60] R. W. Schwartz, “Chemical Solution Deposition of Perovskite Thin Films,” *Chem. Mater.*, vol. 9, no. 11, pp. 2325–2340, Nov. 1997.
[61] G. Yi, Z. Wu, and M. Sayer, “Preparation of Pb(Zr,Ti)O3 thin films by sol gel processing: Electrical, optical, and electro-optic properties,” *J. Appl. Phys.*, vol. 64, no. 5, p. 2717, Sep. 1988.
[62] G. Yi and M. Sayer, “An acetic acid/water based sol-gel PZT process I: Modification of Zr and Ti alkoxides with acetic acid,” *J. Sol-Gel Sci. Technol.*, vol. 6, no. 1, pp. 65–74, Jan. 1996.
[63] S.-Y. Chen and I.-W. Chen, “Texture Development, Microstructure Evolution, and Crystallization of Chemically Derived PZT Thin Films,” *J. Am. Ceram. Soc.*, vol. 81, no. 1, pp. 97–105, 1998.
[64] R. A. Lipeles, D. J. Coleman, and M. S. Leung, “Metalloorganic solution deposition of ferroelectric PZT films,” *IEEE Trans. Ultrason. Ferroelectr. Freq. Control*, vol. 38, no. 6, pp. 684–689, 1991.
[65] Q. Q. Zhang, S. J. Gross, S. Tadigadapa, T. N. Jackson, F. T. Djuth, and S. Trolier-McKinstry, “Lead zirconate titanate films for d33 mode cantilever actuators,” *Sensors Actuators Phys.*, vol. 105, no. 1, pp. 91–97, Jun. 2003.
[66] F. Calame and P. Muralt, “Growth and properties of gradient free sol-gel lead zirconate titanate thin films,” *Appl. Phys. Lett.*, vol. 90, no. 6, pp. 062907–062907–3, 2007.
[67] S. Kezić, K. Mahieu, A. C. Monster, and F. A. de Wolff, “Dermal absorption of vaporous and liquid 2-methoxyethanol and 2-ethoxyethanol in volunteers.,” *Occup. Environ. Med.*, vol. 54, no. 1, pp. 38–43, Jan. 1997.
[68] R. B. Sleet, J. A. Greene, and F. Welsch, “The relationship of embryotoxicity to disposition of 2-methoxyethanol in mice,” *Toxicol. Appl. Pharmacol.*, vol. 93, no. 2, pp. 195–207, Apr. 1988.
[69] K. Aoki, Y. Fukuda, K. Numata, and A. Nishimura, “Dielectric Properties of (111) and (100) Lead-Zirconate-Titanate Films Prepared by Sol-Gel Technique,” *Jpn. J. Appl. Phys.*, vol. 33, no. Part 1, No. 9B, pp. 5155–5158, 1994.
[70] C. J. Kim, D. S. Yoon, J. S. Lee, C. G. Choi, W. J. Lee, and K. No, “Electrical characteristics of (100), (111), and randomly aligned lead zirconate titanate thin films,” *J. Appl. Phys.*, vol. 76, no. 11, pp. 7478–7482, 1994.

[71] X. Du, J. Zheng, U. Belegundu, and K. Uchino, “Crystal orientation dependence of piezoelectric properties of lead zirconate titanate near the morphotropic phase boundary,” *Appl. Phys. Lett.*, vol. 72, no. 19, pp. 2421–2423, May 1998.
[72] D. A. Berlincourt, C. Cmolik, and H. Jaffe, “Piezoelectric Properties of Polycrystalline Lead Titanate Zirconate Compositions,” *Proc. IRE*, vol. 48, no. 2, pp. 220 –229, Feb. 1960.
[73] N. Ledermann, P. Muralt, J. Baborowski, S. Gentil, K. Mukati, M. Cantoni, A. Seifert, and N. Setter, “{1 0 0}-Textured, piezoelectric Pb(Zrx, Ti1−x)O3 thin films for MEMS: integration, deposition and properties,” *Sensors Actuators Phys.*, vol. 105, no. 2, pp. 162–170, Jul. 2003.
[74] I. Kanno, S. Fujii, T. Kamada, and R. Takayama, “Piezoelectric properties of c-axis oriented Pb(Zr,Ti)O3 thin films,” *Appl. Phys. Lett.*, vol. 70, no. 11, pp. 1378–1380, 1997.
[75] M. R. Soares, A. M. R. Senos, and P. Q. Mantas, “Phase coexistence in PZT ceramics,” *J. Eur. Ceram. Soc.*, vol. 19, no. 10, pp. 1865–1871, Aug. 1999.
[76] G. J. Willems, D. J. Wouters, H. E. Maes, and R. Nouwen, “Nucleation and orientation of sol-gel pzt-films on pt electrodes,” *Integr. Ferroelectr.*, vol. 15, no. 1–4, pp. 19–28, 1997.
[77] J. Cheng and Z. Meng, “Orientation controlling of PZT thin films derived from sol-gel techniques,” *J. Mater. Sci. Lett.*, vol. 19, no. 21, pp. 1945–1949, Nov. 2000.
[78] M. Kosec, B. Malic, and M. Mandeljc, “Chemical solution deposition of PZT thin films for microelectronics,” *Mater. Sci. Semicond. Process.*, vol. 5, no. 2–3, pp. 97–103, Apr. 2002.
[79] J. C. Boden and R. A. Back, “Photochemistry and free-radical reactions in formamide vapour,” *Trans. Faraday Soc.*, vol. 66, no. 0, pp. 175–182, Jan. 1970.
[80] S. Trolier-McKinstry, “Private Communication,” 2008.
[81] D. M. Potrepka, G. R. Fox, L. M. Sanchez, and R. G. Polcawich, “Pt/TiO2 Growth Templates for Enhanced PZT films and MEMS Devices,” *MRS Online Proc. Libr.*, vol. 1299, p. null–null, 2011.
[82] G. R. Fox, “Effect of Crystallographic Texture on Ferroelectric Performance of PZT Thin Films,” *MRS Online Proc. Libr.*, vol. 596, p. null–null, 1999.
[83] S. Hiboux and P. Muralt, “Mixed titania-lead oxide seed layers for PZT growth on Pt(111): a study on nucleation, texture and properties,” *J. Eur. Ceram. Soc.*, vol. 24, no. 6, pp. 1593–1596, 03 2003.
[84] C. V. R. V. Kumar, M. Sayer, R. Pascual, D. T. Amm, Z. Wu, and D. M. Swanston, “Lead zirconate titanate films by rapid thermal processing,” *Appl. Phys. Lett.*, vol. 58, no. 11, pp. 1161 –1163, Mar. 1991.
[85] S. Trolier-McKinstry and P. Muralt, “Thin Film Piezoelectrics for MEMS,” in *Electroceramic-Based MEMS*, vol. 9, N. Setter, Ed. Springer US, 2005, pp. 199–215.
[86] R. D. Klissurska, T. Maeder, K. G. Brooks, and N. Setter, “Microstructure of PZT sol-gel films on Pt substrates with different adhesion layers,” *Microelectron. Eng.*, vol. 29, no. 1–4, pp. 297–300, Dec. 1995.

[87] F. K. Lotgering, “Topotactical reactions with ferrimagnetic oxides having hexagonal crystal structures—I,” *J. Inorg. Nucl. Chem.*, vol. 9, no. 2, pp. 113–123, Feb. 1959.
[88] F. Chu and G. Fox, “United States Patent: 6376259 - Method for manufacturing a ferroelectric memory cell including co-annealing,” 637625923-Apr-2002.
[89] J. H. Ma, X. J. Meng, J. L. Sun, T. Lin, F. W. Shi, G. S. Wang, and J. H. Chu, “Effect of excess Pb on crystallinity and ferroelectric properties of PZT(40/60) films on LaNiO3 coated Si substrates by MOD technique,” *Appl. Surf. Sci.*, vol. 240, no. 1–4, pp. 275–279, Feb. 2005.
[90] E. K. F. Dang and R. J. Gooding, “Theory of the Effects of Rapid Thermal Annealing on Thin-Film Crystallization,” *Phys. Rev. Lett.*, vol. 74, no. 19, pp. 3848–3851, May 1995.
[91] Z. Huang, Q. Zhang, and R. W. Whatmore, “Structural development in the early stages of annealing of sol–gel prepared lead zirconate titanate thin films,” *J. Appl. Phys.*, vol. 86, no. 3, pp. 1662–1669, Aug. 1999.
[92] K. G. Brooks, I. M. Reaney, R. Klissurska, Y. Huang, L. Bursill, and N. Setter, “Orientation of rapid thermally annealed lead zirconate titanate thin films on (111) Pt substrates,” *J. Mater. Res.*, vol. 9, no. 10, pp. 2540–2553, 1994.
[93] F. Chu and G. Fox, “Relationship between PB content, crystallographic texture and ferroelectric properties of plzt thin films for FRAM® applications,” *Integr. Ferroelectr.*, vol. 33, no. 1–4, pp. 19–26, 2001.
[94] Y. Shimamoto, K. Kushida-Abdelghafar, H. Miki, and Y. Fujisaki, “H2 damage of ferroelectric Pb(Zr,Ti)O3 thin-film capacitors #x2014;The role of catalytic and adsorptive activity of the top electrode,” *Appl. Phys. Lett.*, vol. 70, no. 23, pp. 3096–3097, 1997.
[95] S. H. Hu, G. J. Hu, X. J. Meng, G. S. Wang, J. L. Sun, S. L. Guo, J. H. Chu, and N. Dai, “The grain size effect of the Pb(Zr0.45Ti0.55)O3 thin films deposited on LaNiO3-coated silicon by modified sol-gel process,” *J. Cryst. Growth*, vol. 260, no. 1–2, pp. 109–114.
[96] K. Okazaki and K. Nagata, “Effects of Grain Size and Porosity on Electrical and Optical Properties of PLZT Ceramics,” *J. Am. Ceram. Soc.*, vol. 56, no. 2, pp. 82–86, 1973.
[97] J.-K. Yang, W. S. Kim, and H.-H. Park, “Effect of grain size of Pb(Zr0.4Ti0.6)O3 sol–gel derived thin films on the ferroelectric properties,” *Appl. Surf. Sci.*, vol. 169–170, pp. 544–548, Jan. 2001.
[98] G. L. Brennecka, C. M. Parish, B. A. Tuttle, and L. N. Brewer, “Multilayer thin and ultrathin film capacitors fabricated by chemical solution deposition,” *J. Mater. Res.*, vol. 23, no. 01, pp. 176–181, 2008.
[99] N. R. Harris, M. Hill, R. Torah, R. Townsend, N. M. Beeby, N. M. White, and J. Ding, “A Multilayer thick-film PZT actuator for MEMS Applications,” *Sensors Actuators Phys.*, vol. 132, pp. 311–316, 2006.
[100] J. S. Song, I. S. Kim, S. J. Jeong, and M. S. Kim, “Multilayer Piezoelectric Ceramic Actuator for Laser Scanner,” *Int. Conf. Opt. MEMS Nanophotonics*, no. 129–130, 2010.

[101] M. Hoffman, T. Leuerer, R. Liedtke, U. Bottger, W. Mokwa, and R. Waser, “Integration of Piezoelectric PZT Thin Films with Internal Electrodes into an Actuator Structure for MEMS Applications,” *Integr. Ferroelectr.*, vol. 50, pp. 21–32, 2002.
[102] G. L. Brennecka, J. F. Ihlefeld, J.-P. Maria, B. A. Tuttle, and P. G. Clem, “Processing Technologies for High-Permittivity Thin Films in Capacitor Applications,” *J. Am. Ceram. Soc.*, vol. 93, no. 12, pp. 3935–3954, 2010.
[103] C. A. Randall, A. Kelnberger, G. Y. Yang, R. E. Eitel, and T. R. Shrout, “High Strain Piezoelectric Multilayer Actuators—A Material Science and Engineering Challenge,” *J. Electroceramics*, vol. 14, no. 3, pp. 177–191, Jul. 2005.
[104] K. Lubitz and H. Hellebrand, “Properties of PZT multilayer actuators,” in , *IEEE 7th International Symposium on Applications of Ferroelectrics, 1990*, 1990, pp. 502 –512.